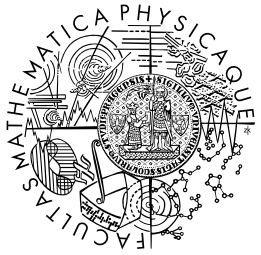

FACULTY
OF MATHEMATICS
AND PHYSICS
Charles University

MASTER THESIS

Bc. Pavel Váňa

Study of charmonia production and radiation at the LHC

Institute of Particle and Nuclear Physics

Supervisor of the master thesis: doc. Mgr. Martin Spousta, Ph.D.
Study programme: Particle and Nuclear Physics
Study branch: FCJFP

Prague 2022

I declare that I carried out this master thesis independently, and only with the cited sources, literature and other professional sources. It has not been used to obtain another or the same degree.

I understand that my work relates to the rights and obligations under the Act No. 121/2000 Sb., the Copyright Act, as amended, in particular the fact that the Charles University has the right to conclude a license agreement on the use of this work as a school work pursuant to Section 60 subsection 1 of the Copyright Act.

In ..... date ....

Author's signature

Dedication

I would like to express my gratitude to my supervisor doc. Mgr. Martin Spousta, Ph.D. for his leadership, patience and moral support during elaboration of this thesis. Also, I would like to thank Mgr. Martin Rybář, Ph.D. for many valuable discussions. Also, I would like to thank my family, especially my beloved mother, for their unconditional love and support throughout my studies.

Title: Study of charmonia production and radiation at the LHC

Author: Bc. Pavel Váňa

Institute: Institute of Particle and Nuclear Physics

Supervisor: doc. Mgr. Martin Spousta, Ph.D., Institute of Particle and Nuclear Physics

Abstract: This thesis contains a study of production and radiation of J/ψ and $\psi(2S)$ in pp collisions. Basic analysis of J/ψ and $\psi(2S)$ using data from pp collisions at $\sqrt{s} = 5.02$ TeV measured in 2017 by the ATLAS Experiment at the LHC is performed. The yield of J/ψ is separated into prompt and non-prompt components. A comparison between Monte Carlo generator Pythia 8.240 and data collected by the ATLAS Experiment in 2015 and 2017 at $\sqrt{s} = 5.02$ TeV is done. Transverse momentum dependent discrepancy between data and simulation is observed. It is seen that the description of charmonia production by Pythia 8 is limited since it cannot reproduce the shape of measured cross-section. An introduction to yield extraction using RooFit from measured data is also provided.

Another part of this thesis is the description of charmonium production and gluon radiation in pp collisions simulated by Pythia generator. The slow growth of the mean value of the number of gluons radiated by charmonium intermediate octet state with increasing p_{T} is observed.

Keywords: charmonia • parton energy loss • heavy-ion collisions • QCD medium • LHC

Název práce: Studium produkce a vyzařování charmonií na LHC

Autor: Bc. Pavel Váňa

Ústav: Ústav částicové a jaderné fyziky

Vedoucí diplomové práce: doc. Mgr. Martin Spousta, Ph.D., Ústav částicové a jaderné fyziky

Abstrakt: Práce je věnována studiu produkce a vyzařování J/ψ a $\psi(2S)$ produkovaných v *pp* srážkách. Bylo provedeno srovnání dat *pp* srážek s těžištovou energií $\sqrt{s} = 5.02$ TeV získaných z Monte Carlo generátoru Pythia 8.240 a dat naměřených v roce 2015, respektive v roce 2017, experimentem ATLAS na urychlovači LHC v CERNu. Výtěžky J/ψ extrahované z dat jsou rozděleny na prompt a non-prompt zdroje. Je pozorována odchylka mezi simulací a naměřenými daty, která závisí na velikosti příčné hybnosti dimuonů. To znamená, že Pythia neposkytuje úplný popis produkce charmonií v *pp* srážkách.Tato práce také popisuje základy extrakce výtěžku z naměřených dat použitím prostředí RooFit.

Další část této práce se zabývá popisem produkce a vyzařování charmonií v *pp* srážkách v generátoru Pythia. Byl pozorován pomalý růst středního počtu gluonů vyzářených intermediálním stavem charmonia v závislosti na rostoucím p_{T}.

Klíčová slova: charmonia • energetické ztráty partonů • srážky těžkých iontů • QCD médium • Velký hadronový urychlovač

Contents

List of Abbreviations

ALICE ..... A Large Ion Collider Experiment

ATLAS ..... A Toroidal LHC Apparatus

CEM ..... The Colour-Evaporation Model

CERN ..... European Organization for Nuclear Research

CMS ..... The Compact Muon Solenoid

COM ..... The Colour-Octet Mechanism

CSM ..... The Colour-Singlet Model

GMC ..... Glauber Monte-Carlo

ID ..... The Inner Detector

LEIR ..... Low Energy Ion Ring

LEP ..... Large Electron-Positron Collider

LHC ..... Large Hadron Collider

LHCb ..... Large Hadron Collider beauty

LHCf ..... Large Hadron Collider forward

MC ..... Monte Carlo generator

MoEDAL ..... Monopole and Exotics Detector at the LHC

NRQCD ..... Non-relativistic QCD

PID ..... Particle identification

PS ..... Proton Synchroton

QCD ..... Quantum chromodynamics

QED ..... Quantum electrodynamics

QGP ..... Quark-gluon plasma

RHIC ..... Relativistic Heavy Ion Collider

SLAC ..... Stanford Linear Accelerator Center

SM ..... The Standard Model of particle physics

SPS ..... Super Proton Synchroton

TOTEM ..... TOTal Elastic and diffractive cross section Measurement

WIP ..... Work in progress

Introduction

The subject of this thesis is an experimental study of charmonia, J/ψ and $\psi(2S)$, produced in proton-proton (pp) collisions at the center-of-mass energy $\sqrt{s} = 5.02$ TeV corresponding to the center-of-mass energy of Pb+Pb collisions at the Large Hadron Collider (LHC) during Run 2. This thesis aims to introduce the problem of charmonia production in pp collisions and analyses data measured by the ATLAS experiment at the LHC. Further, production of charmonia in Monte Carlo generator PYTHIA is studied in order to understand gluon radiation of charmonia octets evolving to physical states.

Ultra-relativistic collisions of heavy-ions are expected to produce extremely hot, dense and deconfined medium. Degrees of freedom of this deconfined medium are free quarks and gluons. Therefore, the medium is called *quark-gluon plasma (QGP)*. First attempts to create QGP were made by scientists at CERN's Super-Proton Synchrotron (SPS) in the 1980s and 1990s. Further studies of QGP were performed at Relativistic Heavy Ion Collider (RHIC) at Brookhaven National Laboratory (BNL) on Long Island in the United States which started the operation in 2000.

Highly collimated showers of hadrons and other particles produced by the hadronization process are created during pp and heavy-ion collisions. These showers are called *jets*. Jets propagating through QGP do not behave the same as those produced in pp collisions. In heavy-ion collisions, jets lose energy due to interaction with the hot and dense plasma. This phenomenon is called *jet quenching*. Since we cannot directly observe QGP, it is necessary to use "probes" to measure its properties, and jets and charmonia are often used as QGP probes.

J/ψ was the first observed charm quark meson (bound state of charm quark and charm anti-quark). It was discovered in 1974 independently by two laboratories - BNL in Long Island and Stanford Linear Accelerator Center (SLAC). Nearly in 1986, Tetsuo Matsui and Helmut Satz suggested that charmonia could be sensitive QGP probes [1]. They also postulated that interaction with the hot and dense plasma would lead to a dissociation of bound state leading to observable charmonia suppression.

Currently, the precise mechanism of charmonia production in pp and mechanism of charmonia suppression in heavy-ion collisions are unknown. This thesis aims to make the first steps towards a full analysis of charmonium production in heavy-ion collision data. Further, it aims to quantify gluon radiation using Monte Carlo simulations in PYTHIA which can be used in future data analysis.

This thesis is organised as follows: Chapter 1 provides the theoretical background introducing the Standard Model of particle physics, the concept of Quantum chromodynamics, jets and jet algorithms. Chapter 2 provides an introduction to heavy-ion collisions, its description by the Glauber model and quarkonia production. Chapter 3 contains the description of the LHC and the ATLAS Experiment. Chapter 4 introduces our results. First, the results of PYTHIA simulations are introduced, then the basics of yield extraction using RooFit is described. Further, results of our analysis are compared with results extracted from PYTHIA and previous measurements done by the ATLAS Collaboration [2].

1. The Standard Model and the theory of the strong interaction

The first chapter of this thesis provides a brief introduction to the Standard Model of particle physics, a model describing elementary particles and their interactions. Since this thesis focuses on the study of the interaction between quarks and gluons, the basics of the theory of strong interaction, *the Quantum chromodynamics (QCD)*, are summarised.

1.1 The Standard Model of particle physics

The Standard Model of particle physics (SM) is a physical theory describing electromagnetic, weak (electroweak) and strong interaction. That means that SM provides description of the three of four known forces in the universe. The gravitational force is not included in the SM, it is described by the Theory of General Relativity made by Albert Einstein. Gravitational force is neglected in this thesis.

The Standard Model is formulated in quantum field theory mathematical framework as a Yang-Mills theory based on SU(3) × SU(2) × U(1) local gauge symmetry [3]. The process of building the Standard Model started in the first half of the 20th century, when the *Quantum electrodynamics*, quantum field theory of electrodynamics, was formulated by Paul Dirac. First theory of weak interactions was proposed by Enrico Fermi in 1933. First steps towards composing these theories into the Standard Model were made in the second half of the 20th century when Chen Ning Yang and Robert Mills extended the concept of gauge theory for abelian groups. In early 1960s, Sheldon Glashow combined electromagnetic and weak interactions to electroweak force [4]. Later, the Higgs mechanism was introduced as a method how to treat residual divergences. The Standard Model development was finalized in the 1970s as the theory of the strong interaction (Quantum chromodynamics, QCD) was introduced. Basics of the QCD are described in Section 1.2.

The particles in the SM are divided into groups by their properties, such as charge, spin, colour and other quantum numbers. The basic distribution is made in a sense of the particle spin:

- *Fermions* are particles with half-integer spin. They obey Fermi-Dirac statistics. There are three generations of fermions in the nature, which differ by their mass. Due to the Pauli exclusion principle, only two fermions can occupy the same quantum state.

- *Bosons* are particles with integer spin. They obey the Bose-Einstein statistics, and in contrast with fermions, there is no limit on the number of bosons that may occupy the same quantum state. Elementary bosons act like force carriers; they intermediate the interaction between particles, thus elementary bosons are called *intermediate bosons*.

Fermions were named by Paul Dirac, who predicted that every particle is associated with an antiparticle with the same mass but opposite quantum charges.

An interaction of particle and antiparticle is called annihilation. The Standard Model scheme of elementary particles is described below and shown in Figure 1.1.

Leptons are fermions with integer electric charge interacting via electroweak interactions. Neutral leptons are called *neutrinos*, hence neutrinos do not interact electromagnetically.

Quarks are fermions that interact via strong, weak and electromagnetic force. They were predicted by theoreticians M. Gell-Mann and G. Zweig in 1964 to solve the problem of hadron classification scheme. Gell-Mann and Zweig postulated that hadrons are particles consisting of quarks. Evidence of proton quark structure was observed in 1969 at SLAC in deep inelastic scattering experiments. Quarks are described by their electric charge, mass, spin, flavour and colour.

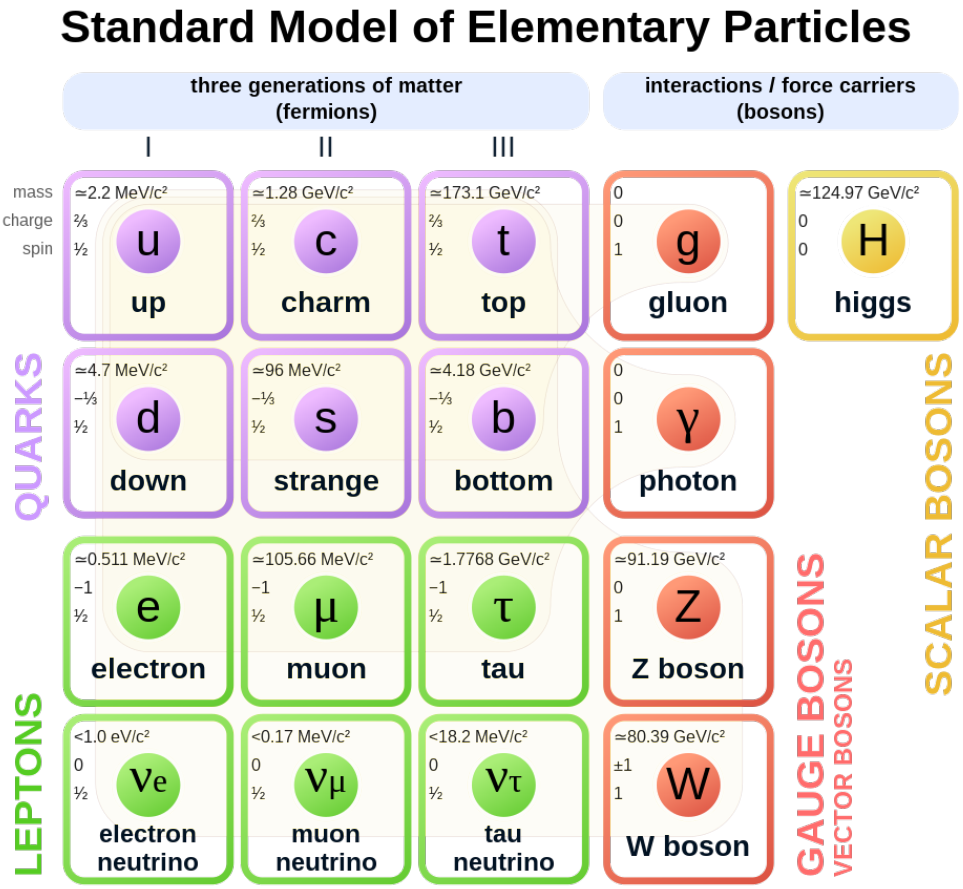

Figure 1.1: The scheme of elementary particles in the Standard Model of particle physics. Figure taken from [5].

Intermediate bosons (gauge bosons) are bosons mediating interactions between particles. *Gluon* is boson responsible for strong interaction, which is connected with particles with quantum number *colour*. The strong interaction forces quarks to make bound states - *hadrons*. *Photon* is boson mediating electromagnetic force. Together with gluons, these bosons are masseless. Quantum field theory describing electromagnetic force is called *Quantum electrodynamics (QED)*. Weak interactions are mediated via electrically charged vector bosons W^+, W^-, which change quark and lepton flavour. Z^0 vector boson is electrically neutral and it

is responsible for weak interactions of neutrinos, and production of fermion anti-fermion pairs. Z^0 does not change particle flavor. *Higgs boson* is scalar boson (spin 0) predicted by P. Higgs, F. Englert and R. Brout in 1964. This boson is essential for understanding how particles get its mass via Higgs model. It was discovered in 2012 by experiments ATLAS and CMS at CERN [6].

For more details about SM see [4, 7, 8].

1.2 Quantum chromodynamics

Quantum chromodynamics (QCD) is the quantum field theory describing interaction of coloured particles (particles with quantum number colour - quarks and gluons). It explains how elementary quarks and gluons form colourless composite particles - *hadrons*, either *mesons* (bound states of quark q and anti-quark $\bar{q}$) or *baryons* (bound states consisting of three quarks qqq). Following paragraphs provide a brief introduction to QCD. For details see e.g. [9, 10].

QCD is the Yang-Mills quantum field theory based on non-abelian SU(3) group. The non-abelian character of QCD is given by the fact, that quarks exist in three colour states. Therefore, basic mathematical quantity describing a quark with flavour f is colour SU(3) triplet:

$$\Psi^f \equiv \begin{pmatrix} \psi^f_{\mathrm{R}} \\ \psi^f_{\mathrm{G}} \\ \psi^f_{\mathrm{B}} \end{pmatrix}, \tag{1.1}$$

where R means red, G stands for green and B means blue. As in other quantum field theories, the dynamics is encoded in Lagrangian density $\mathcal{L}$, which in case of QCD is given by following form:

$$\mathcal{L}_{\mathrm{QCD}} = -\frac{1}{4} G^a_{\mu\nu} G^{\mu\nu}_a + \sum_{flavour} \bar{\Psi}^i_f \left(i\gamma_\mu D^\mu - \delta_{ij} m_f \right) \Psi^j_f, \tag{1.2}$$

where $G^{\mu\nu}_a$ denotes modified gluon field strength tensor corresponding to colour index a ($a = 1, \ldots 8$), ψ_f is corresponding to Dirac spinor SU(3) triplet of quark with flavour f defined by Equation (1.1), m_f denotes "bare" mass of quark with flavour f, γ_μ stands for Dirac matrices and D is covariant derivative defined as follows:

$$D = \delta_{ij}\partial_\mu - \sum_a i g T^a_{ij} A^a_\mu, \tag{1.3}$$

where g is the QCD coupling constant. Usually, this constant is expressed as the *strong coupling constant* α_s, which is related to the QCD coupling constant g by relation $\alpha_s = g^2/4\pi$. T_a are generators of SU(3) fundamental representations (called Gell-Mann colour matrices) and A^a_μ are gauge gluon fields. The Gell-Mann colour matrices satisfy the Lie algebra such that:

$$[T_a, T_b] = i f_{abc} T_c, \tag{1.4}$$

where $f_{abc} \in \mathbb{R}$ represents structure constants of SU(3) group. To preserve Lagrangian density SU(3)-gauge invariance, quark and gluon fields must satisfy these relations:

$$\Psi_f \to \Psi'_f = e^{i\alpha_a T_a} \Psi_f, \quad A^a_\mu \to \left(A^a_\mu \right)' = A^a_\mu - f^{abc} \alpha^b A^c_\mu + \frac{1}{g} \partial_\mu \alpha^a \tag{1.5}$$

As a consequence of the local gauge invariance, the gluon field strength tensor reads as follows:

$$G^a_{\mu\nu} = \partial_\mu A^a_\nu - \partial_\nu A^a_\mu + g f_{abc} A^b_\mu A^c_\mu \tag{1.6}$$

To see any particular consequences of non-abelian structure of SU(3) gauge group, one can write Lagrangian density (1.2) explicitly using relations (1.3) and (1.6). It is possible to separate QCD Lagrangian density $\mathcal{L}_{\mathrm{QCD}}$ into free part and interaction part:

$$\mathcal{L}_{\mathrm{QCD}} = \mathcal{L}_{\mathrm{free}} + \mathcal{L}_{\mathrm{int}} \tag{1.7}$$

The interaction part of QCD Lagrangian density can be written in the following form:

$$\mathcal{L}_{\mathrm{int}} = -g\bar{\Psi}_f \gamma^\mu T_a \Psi A^a_\mu - \frac{1}{2} g f_{abc} \left(\partial^\mu A^\nu_a - \partial^\nu A^\mu_a\right) A^b_\mu A^c_\nu - \frac{1}{4} g^2 f_{abc} f_{ade} A^b_\mu A^c_\nu A^\mu_d A^\nu_e \tag{1.8}$$

In the interaction part of QCD Lagrangian density (1.8) one can identify the first term as a standard interaction vertex known from the quantum electrodynamics (QED). However, in QCD this term has different strength constant g, and Gell-Mann colour matrices modify it due to the colour structure of the quark field. The second and third vertex are new terms in QCD compared to the QED due to the non-abelian structure of QCD. The second term describes the self-interaction vertex of three gluon fields, and the third term describes the self-interaction vertex of four gluon fields. These QCD vertices are illustrated via Feynman diagrams in Figure 1.2.

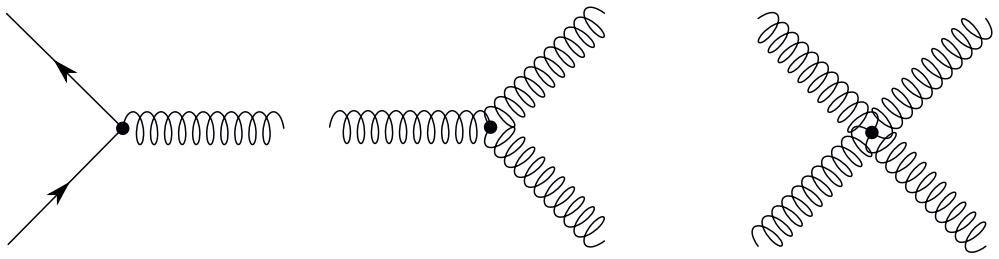

Figure 1.2: Feynman diagrams corresponding to QCD interaction vertices.

These differences between QCD and QED are given by fact, that QED gauge bosons (photons) do not carry the charge while QCD gauge bosons (gluons) do cary the charge (color charge). Therefore, they can interact with each other. This non-abelian structure of QCD leads to two specific phenomena - *colour confinement* and *asymptotic freedom*.

QCD is suffering, like QED, by divergences when one performs perturbative calculations. These divergences come from quantum loops and result from integration over the unconstrained loop momenta. Divergences can be divided into two categories:

- *Ultraviolet divergences (UV)* - results of integration over large values of loop momenta
- *Mass divergences* - the result of integration over the region of small virtualities

There are generally two steps how to treat them:

- *Regularization* - this method is formally based on cutting off high values of the loop momenta (e.g. Pauli-Villars, dimensional regularization, etc.)
- *Renormalization* - after the regularization divergent terms are absorbed by redefined (renormalized) quantities

For more details about these methods see [9, 3]. Due to renormalization of $\mathcal{L}_{\mathrm{QCD}}$ the original coupling constant g depends on the renormalization (non-physical) scale μ. Typically the scale μ should be chosen as the typical physical scale of the analysed process. In deep inelastic scattering scale μ is conventionally chosen as transferred momentum squared Q^2. Sometimes it is preferable to use the square root of the CMS energy $\sqrt{s}$. The fact that the coupling constant of strong interaction α_s depends on the renormalization scale is often called "running of coupling constant". This phenomenon is described by the so-called renormalization group equation:

$$\frac{\partial \alpha_s(Q^2)}{\partial \log Q^2} \equiv \beta(\alpha_s) = -\left[\frac{\beta_0}{4\pi}\alpha_s^2(Q^2) + \left(\frac{1}{4\pi}\right)^2 \beta_1 \alpha_s^3(Q^2) + \left(\frac{1}{4\pi}\right)^3 \beta_2 \alpha_s^4(Q^2) + \dots\right], \tag{1.9}$$

where β_0 and β_1 are determined only by the numbers of quark flavours n_f and colours N_c as follows:

$$\beta_0 = \frac{11N_c - 2n_f}{3} \tag{1.10}$$

$$\beta_1 = \frac{34N_c^2 - 16N_c n_f}{3}. \tag{1.11}$$

By solving Equation (1.9) at the lowest order one obtains a following equation describing how the strong coupling constant α_s changes from scale μ^2 to Q^2:

$$\alpha_s(Q^2) = \frac{\alpha_s(\mu^2)}{1 + \frac{\beta_0}{4\pi}\alpha_s(Q^2)\log\left(\frac{Q^2}{\mu^2}\right)}. \tag{1.12}$$

From Equation (1.10) it is clearly seen that $\beta_0 > 0$, which means leading term in 1.9 is negative. Therefore, $\alpha_s(Q^2) \to 0$ for $Q^2 \to \infty$. This phenomenon called *asymptotic freedom* describes that quarks and gluons behave like free particles at large transverse momenta.

Another way how to rewrite Equation (1.12) can be done introducing the energy scale Λ:

$$\alpha_s(Q^2) = \frac{4\pi}{\beta_0 \log\left(\frac{Q^2}{\Lambda^2}\right)}, \tag{1.13}$$

where Λ describes the lower bound of applicability of perturbative calculations. The QCD starts to diverge at scale $\Lambda_{QCD} \approx 200 - 400\,\mathrm{MeV}$ at the first order of right hand side of Equation (1.9), which means perturbative calculations cannot be used and non-perturbative QCD needs to be used. In this region, so-called Lattice QCD [10] is used (QCD is formulated on spacetime, that was discretized into a infinite lattice.). Λ_{QCD} is often called as the Landau pole. Since $\alpha_s(Q^2) \to \infty$ in region of small transferred momenta at leading order (LO), quarks and gluons are confined and create colourless bound states - hadrons. This phenomenon is called *colour confinement* and it explains why particle detectors cannot detect

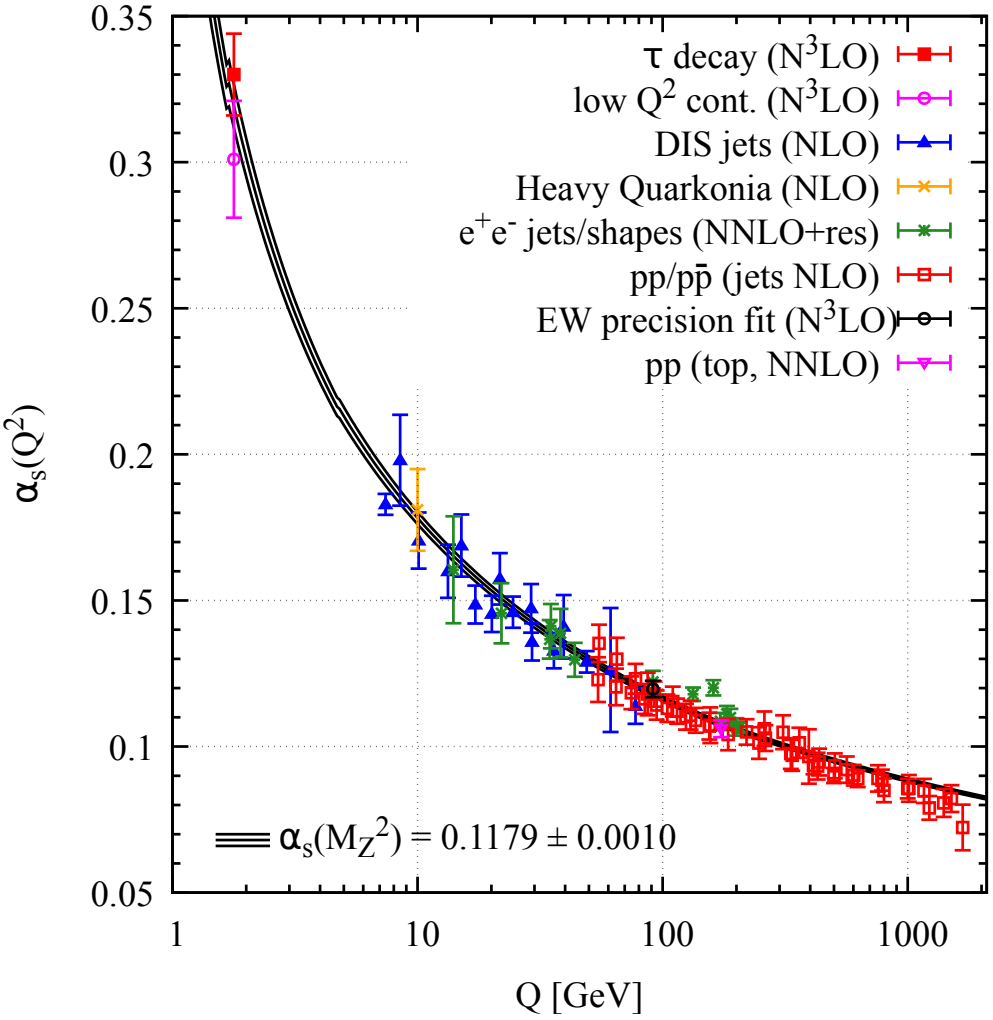

Figure 1.3: Measurements of α_s as a function of the energy scale Q. Various degrees of perturbative QCD calculations were used to extract α_s from the data (NLO: next-to-leading order, NNLO: next-to-next-to-leading order, NNLO+res: NNLO with ressumation, N^{3}LO: next-to-NNLO). Figure is taken from [11].

any coloured particles directly. Mechanism describing process of hadron creation is called *hadronization*.

Conventionally strong coupling constant α_s is explicitly calculated for renormalization scale chosen as $\mu^2 = m_Z^2$ (rest mass of the Z-boson). Its value is shown in Figure 1.3 that summarizes results of previous measurements of α_s.

1.2.1 Jets in QCD

Relativistic collisions of hadrons or heavy-ions may lead to the hard scattering of constituent quarks or gluons collectively called *partons*. These so-called partonic hard processes lead to the creation of new partons due to large momentum transfer during hard scattering. At this stage, partons are almost free, and perturbative QCD can be applied. As the partons move aside from each other, the gluonic field between them increases up to the moment when it is more efficient to create new quark-antiquark pairs. Also, accelerated colour charged particle radiates partons to decrease their virtuality (their four-momentum squared is not equal to their rest

mass). Due to colour confinement created quarks and gluons then recombine with quarks and antiquarks created from vacuum and form hadrons - *hadronization* [9]. This process repeats until quarks do not have enough energy to produce new $q\bar{q}$ pairs leaving two sets of hadrons travelling in the opposite directions. These hadrons are usually collimated into the cone around the direction of the primary parton. This collimated spray of particles is called *jet*. Measuring properties of jet provides essential information about primary parton.

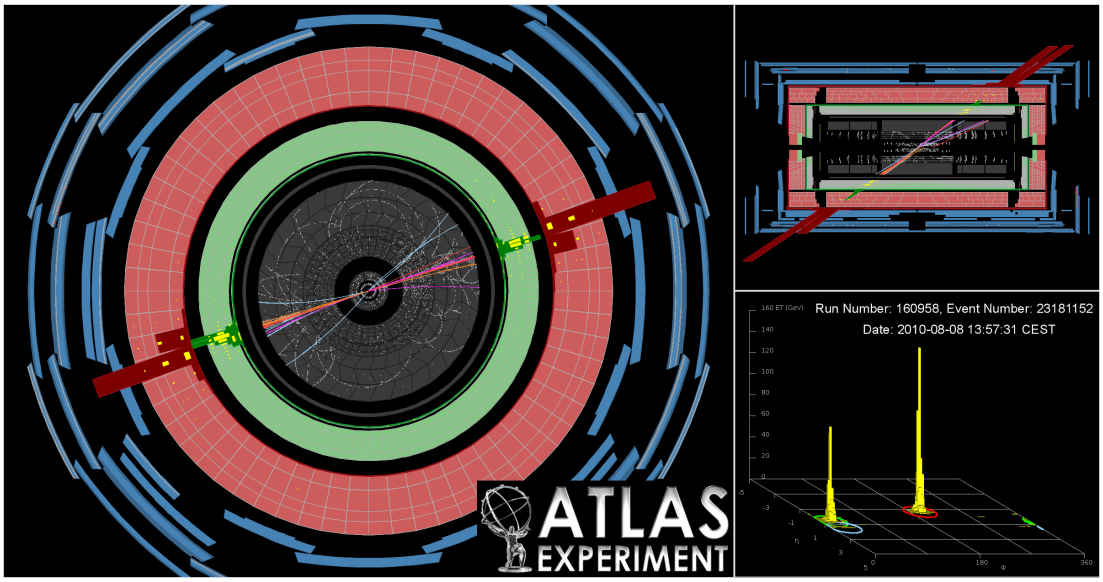

Figure 1.4: Display of a di-jet event produced in pp collisions at $\sqrt{s} = 13\,\text{TeV}$ in 2017. The view of the event in the plane transverse to the beam direction is shown on the left side of the figure. The top-right panel presents the longitudinal view of the event. The bottom-right panel represents the calorimeter clusters in the $(\eta - \phi)$ plane. The figure is taken from [12].

1.2.2 Jet algorithms

Jet reconstruction algorithm is a procedure of combining the calorimetry and tracking information to define jets. These algorithms must be *collinear safe* and *infrared (IR) safe*. Collinear safety is violated when collinear splitting changes jet. IR safety is violated when soft emissions change jet. Two types of jet algorithms exist:

- *Cone algorithms* - e.g. SIScone,
- *Sequential clustering algorithms* - e.g. k_{T} algorithm, anti-k_{T} algorithm.

Cone algorithms are based on fixed cone shape drawn in $(\eta - \phi)$ plane with cone radius R_{cone}. Basic version of these algorithms is not collinear and IR safe. For more details, see, e.g. [13]. Safety problems followed by other problems led to the introduction of sequential clustering algorithms.

Sequential clustering algorithms are IR and collinear safe. All sequential clustering algorithms have similar steps. First, the distance variable between two

particles d_{ij} is defined as:

$$d_{ij} = min(p_{\mathrm{T}i}^{a}, p_{\mathrm{T}j}^{a})\frac{R_{ij}^{2}}{R}, \tag{1.14}$$

where a is an exponent whose value depends on the particular clustering algorithm, R is the radius parameter determining the final size of the jet. In ATLAS experiment $R = 0.4$ is used for narrow jets and $R = 0.6$ for wide jets [14]. R_{ij} is distance between particles in $(\eta - \phi)$ space defined as:

$$R_{ij} = \sqrt{(\eta_i - \eta_j)^2 + (\phi_i - \phi_j)^2}. \tag{1.15}$$

Second, the distance parameter d_{iB} is defined as:

$$d_{iB} = p_{\mathrm{T}i}^{a}. \tag{1.16}$$

d_{iB} corresponds to the momentum space distance between the beam axis and the particle. The sequence of this algorithm is following:

1. Compute all distances d_{ij} and d_{iB} and find the smallest one:
   - If the smallest one is d_{ij}, combine particles i and j into one and start from step (1)
   - If the smallest one is d_{iB}, remove particle from the list and call it a jet
2. Repeat step (1) until all particles are clustered into a jet

Exponent a in Equation (1.14) is different for various cluster algorithms. $a = 2$ is corresponding to the k_{T} algorithm. $a = -2$ is corresponding to the anti-k_{T} algorithm, which is used by the ATLAS Experiment [14]. This clustering algorithm reduces sensitivity to the jet internal structure and it leads to jets of cone-like shape. $a = 0$ is corresponding to the *Cambridge/Aachen algorithm*, which is often used for studying jet substructure. For more details see [13].

2. Heavy-ion collisions

Quantum chromodynamics predicts the creation of a new state of matter in extreme conditions of very high densities and temperatures. Deconfined quarks and gluons are degrees of freedom of this medium. Hence it is called *quark-gluon plasma (QGP)*. Shortly after the Big Bang, the universe was filled with QGP for a few millionths of a second. In order to recreate matter in these conditions, relativistic heavy-ion collisions are performed.

During collisions of nuclei, it is expected that the nuclei deposit a large amount of energy into a minimal volume. It may lead to the creation of the QGP, according to Bjorken [15]. Each collision of heavy nuclei may lead to a production of several thousands of particles. High precision and sensitive detector must be used to study QGP production and phenomena related to its presence. In order to reconstruct events produced in such collisions, the used detector must be able to detect particles in full azimuth.

The presence of QGP was firstly seen in study of Au+Au collisions with nucleon-nucleon center-of-mass energy $\sqrt{s_{NN}} = 200$ GeV at RHIC [16]. Production of QGP was also confirmed using Pb+Pb collisions at the LHC at CERN. These heavy-ion collisions are studied by ATLAS Experiment, *A Compact Muon Solenoid (CMS)* and *A Large Ion Collider Experiment (ALICE)*.

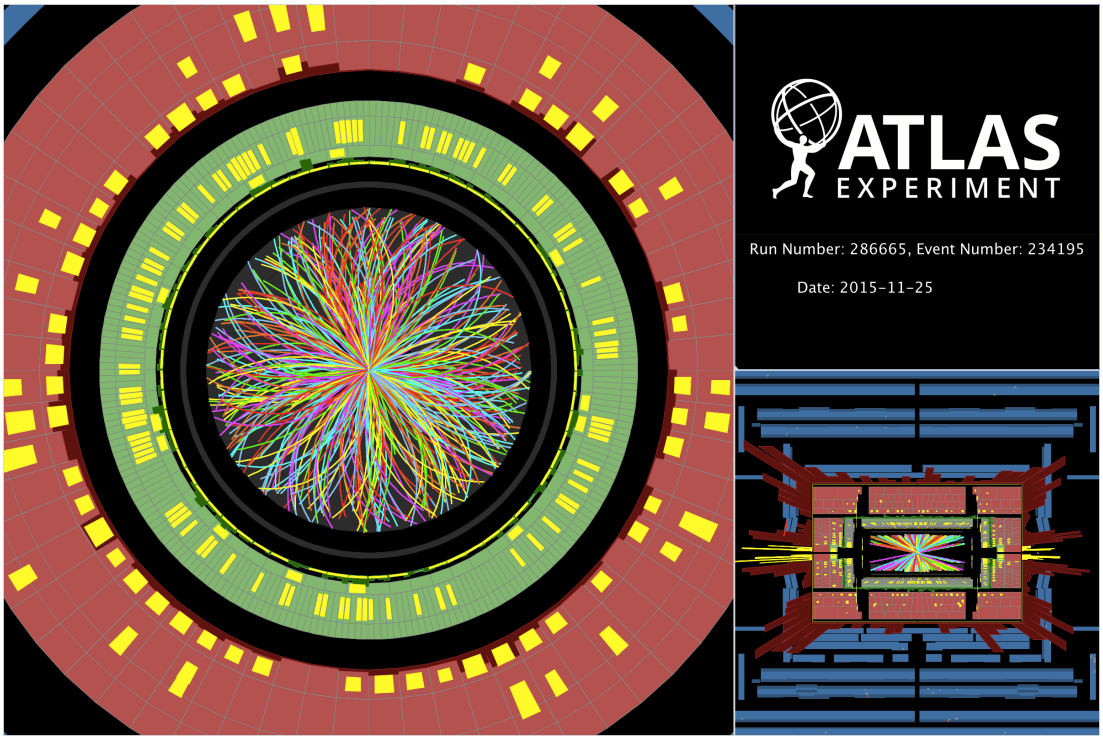

Figure 2.1: The event display representing reconstructed event of Pb+Pb collision from 2015. Figure taken from [17].

2.1 The Glauber model

The Glauber model is a phenomenological model proposed by Roy Glauber [18, 19] describing geometry of heavy-ion collision.

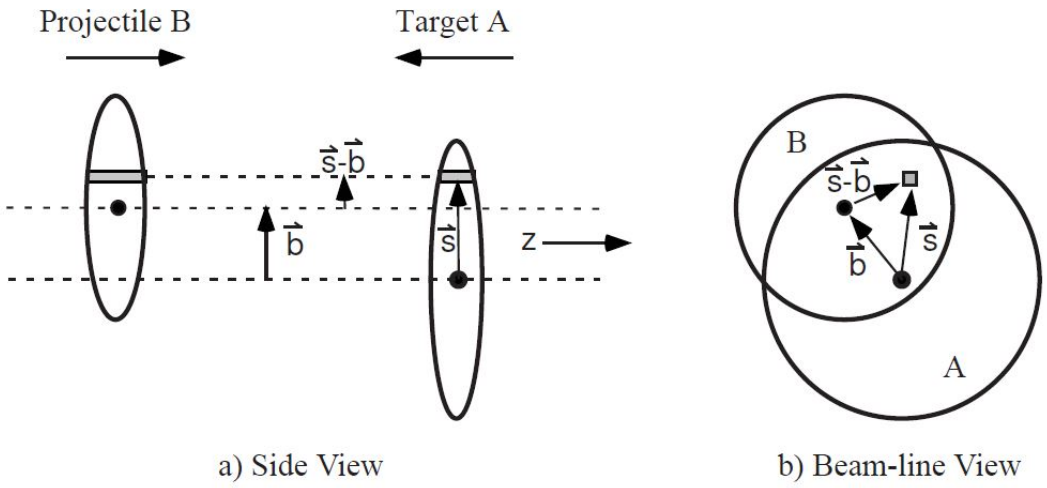

Figure 2.2: Schematic representation of the Glauber model geometry of two nuclei colliding with impact parameter b. A transversal view (left), and longitudinal view (right) are shown. Figure taken from [19].

During the heavy-ion collision, two Lorentz contracted disks collide with the *impact parameter* b. This scheme is shown in Figure 2.2. The impact parameter b is defined as the distance between the centers of the colliding nuclei in a transverse plane. Using the impact parameter quantity, one can divide collisions to the *central collisions* ($b \approx 0$), *peripheral collisions* ($0 < b < 2R$) and *ultra-peripheral collisions* ($b > 2R$), where R describes the radius of colliding nuclei.

The Glauber model assumes that collision of two nuclei consist of superposition of all nucleon-nucleon collisions. The density of nucleons in a distance r from the center of a nucleus is typically parametrised by the *Woods-Saxon distribution* as

$$\rho = \frac{\rho_0}{1 + \exp\left(\frac{r-R}{a}\right)}, \tag{2.1}$$

where ρ_0 is a normalisation constant, a represents the "skin depth" of the nucleus with the radius R.

Consider two nuclei, A and B, colliding with the impact parameter b as it is described in Figure 2.2. A key quantity of the Glauber model is the *nuclear thickness function*, which represents the probability per unit transverse area of a given nucleon being located in the flux tube in distance s from nucleus A. The nuclear thickness function is defined as

$$T_A(\vec{s}) = \int \rho_{\mathrm{A}}(\vec{s}, z_A)\mathrm{d}z_A. \tag{2.2}$$

Nuclear overlap function is defined as

$$T_{AB}(\vec{b}) = \int T_A(\vec{s})\, T_B(\vec{s} - \vec{b})\mathrm{d}^2 s, \tag{2.3}$$

where b is the impact parameter. The product $T_A(\vec{s})T_B(\vec{s}-\vec{b})\mathrm{d}^2s$ represents the joint probability per unit area of finding nucleons in the flux tubes of nuclei A and B of differential area d^2s. The probability of one inelastic nucleon-nucleon collision is expressed using nucleon-nucleon inelastic cross-section σ^{NN} as $T_{AB}(\vec{b})\sigma^{\mathrm{NN}}$.

The probability of n inelastic collisions between A nucleons of the nucleus A and the B nucleons of the nucleus B is given by the Poisson distribution as

$$P(n,\vec{b}) = \binom{AB}{n}\left[T_{\mathrm{AB}}(\vec{b})\sigma^{\mathrm{NN}}_{\mathrm{inel}}\right]^n\left[1-T_{\mathrm{AB}}(\vec{b})\sigma^{\mathrm{NN}}_{\mathrm{inel}}\right]^{AB-n}. \tag{2.4}$$

The impact parameter dependent on a total number of nucleon-nucleon binary collisions N_{coll} is calculated as the mean of a binomial distribution as

$$N_{\mathrm{coll}}(\vec{b}) = \sum_{n=1}^{AB} nP(n,\vec{b}) = AB\,T_{AB}(\vec{b})\,\sigma^{\mathrm{NN}}_{\mathrm{inel}}. \tag{2.5}$$

The number of *participants* N_{part} is the total number of interacting nucleons. The number of participants at impact parameter b can be calculated as

$$\begin{aligned} N_{\mathrm{part}}(\vec{b}) = A\int T_A(\vec{s})\{1-\left[1-T_B(\vec{s}-\vec{b})\sigma^{\mathrm{NN}}_{\mathrm{inel}}\right]^B\}\mathrm{d}^2s \\ +B\int T_B(\vec{s}-\vec{b})\{1-\left[1-T_A(\vec{s})\sigma^{\mathrm{NN}}_{\mathrm{inel}}\right]^A\}\mathrm{d}^2s. \end{aligned} \tag{2.6}$$

One of the techniques used to determine N_{part} and N_{coll} is the *Glauber Monte Carlo technique (GMC)*. This technique is based on populating two nuclei with the Woods-Saxon distribution described by Equation (2.1). The collisions of nuclei with randomly generated impact parameters b are performed. The GMC assumes that nucleus-nucleus collision is a sequence of independent binary nucleon-nucleon collisions. Therefore, the nucleons travel on straight-line trajectories, and the inelastic nucleon-nucleon cross-section is independent of the number of collisions of each nucleon.

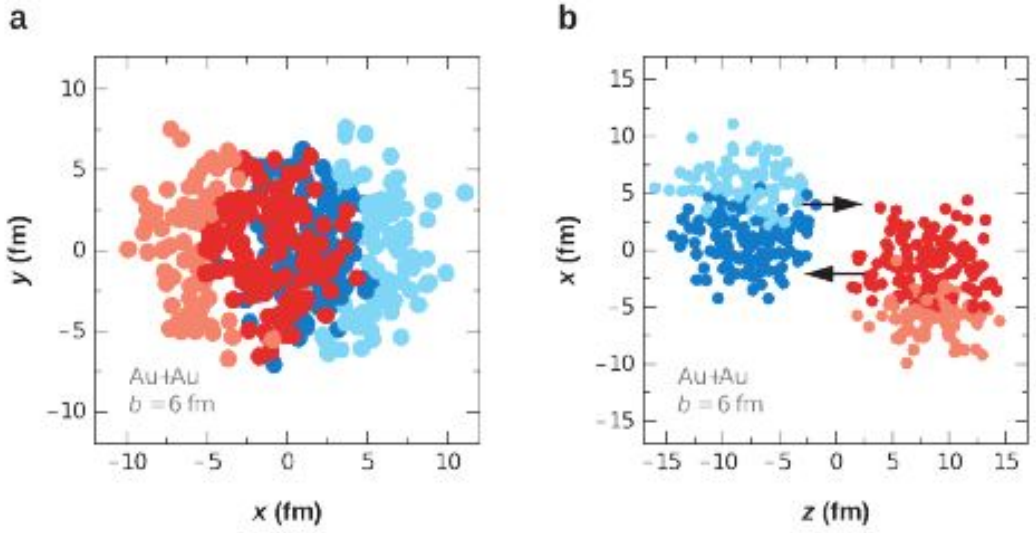

Figure 2.3: An Au-Au GMC event with impact parameter $b = 6$ fm. A transversal view (a) and the longitudinal view (b) is shown. Darker circles represent participating nucleons. Figure taken from [19].

The schematic view of the heavy-ion collision event generated using GMC is shown in Figure 2.3. Transverse distance d of nucleon to the beam axis is calculated for every nucleon. If the distance d satisfies condition

$$d \leq \sqrt{\frac{\sigma_{\text{inel}}^{\text{NN}}}{\pi}}, \tag{2.7}$$

then nucleons are said to have participated in the collision and the N_{coll} is incremented. The number of participants N_{part} is estimated as the number of nucleons, which satisfied condition described by the Equation (2.7) at least once.

2.1.1 Centrality definition

Parameters such as the impact parameter b, the number of participants N_{part} or the number of collisions N_{coll} are not directly observable. In order to quantify the degree of geometrical overlap of two colliding nuclei, concept of *centrality classes* was introduced.

The basic assumption underlying centrality classes is that the impact parameter is related to particle multiplicity or the overall event activity. For events with large b, we expect low multiplicity and a small overall event activity, whereas for events with small b, we expect large multiplicity and a large overall event activity. Models have shown that the multiplicity and the total transverse energy E_{T} are correlated with the number of participants N_{part}.

Centrality classification at the ATLAS experiment is done by measurement of the total transversal energy deposited in forward calorimeters (FCal). The FCal E_{T} distribution is calculated by summing the total transversal energy $\sum E_{\text{T}}$ for every event in the FCal. Data are then split into fractions of equal cross-section called *centrality bins*, shown in Figure 2.4. These bins are expressed in terms of percentiles. By convention, the 0–10% bin represents the most central 10 % of collisions and increasing percentiles to high values refer to more peripheral collisions. Performing the GMC method described above, one can extract mean values of parameters used in Glauber model, i.e. $\langle b \rangle$, $\langle N_{\text{part}} \rangle$, $\langle N_{\text{coll}} \rangle$, etc.

2.2 Jets - nuclear modification factor R_{AA} and its measurement

Products of the hard-scattering of quarks and gluons in heavy-ion collisions evolve as parton showers propagating through the QGP. These parton shower constituents may suffer from interaction with deconfined quarks and gluons in the QGP, and as a consequence, they lose energy.

There are two main types of energy loss caused by the interaction with the QGP constituents [21]:

- Elastic scattering of parton shower constituents on the QGP constituents.
- Medium-induced gluon radiation called radiative energy loss. It is a QCD analogue to the QED bremsstrahlung.

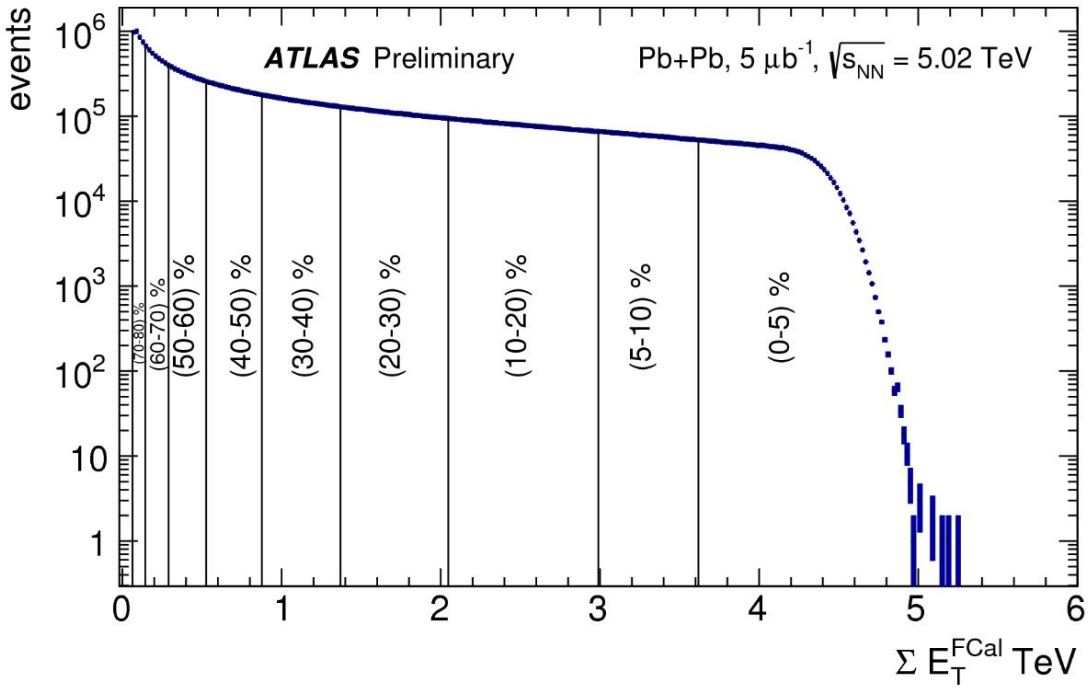

Figure 2.4: Measured FCal $\sum E_{\mathrm{T}}$ distribution in Pb+Pb collisions at $\sqrt{s_{\mathrm{NN}}} = 5.02$ TeV divided into centrality bins. Figure taken from [20].

It is expected that the radiative energy loss is dominant over the energy loss caused by the elastic scattering. Perturbative QCD predicts the production of two back-to-back partons during hard scattering interactions. These partons evolve as parton showers and hadronize and as a result the back-to-back dijet is observed. Parton interaction with QGP and associated parton energy loss leads to the modification of jet yields and jet properties. This phenomenon is called *jet quenching* [21].

Bjorken suggested that jets can be used as a QGP "probes" in order to study properties of such deconfined medium [15]. He also pointed out that one jet can be almost unquenched; meanwhile, the QGP can absorb the second jet. Evidence for the jet quenching at the LHC was provided by the measurements of properties of jet pairs [22].

In order to quantify the magnitude of the inclusive jet suppression in heavy-ion collisions, the *nuclear modification factor* R_{AA} is introduced. R_{AA} is defined as

$$R_{\mathrm{AA}} = \frac{\frac{1}{N_{\mathrm{evt}}} \frac{\mathrm{d}^2 N_{\mathrm{jet}}}{\mathrm{d}p_{\mathrm{T}}\mathrm{d}y}\Big|_{\mathrm{cent}}}{\langle T_{\mathrm{AA}} \rangle \frac{\mathrm{d}^2 \sigma_{\mathrm{jet}}}{\mathrm{d}p_{\mathrm{T}}\mathrm{d}y}\Big|_{pp}}, \tag{2.8}$$

where N_{jet} and σ_{jet} are the jet yield in Pb+Pb collisions and the jet cross-section in pp collisions, respectively, both measured as a function of transverse momentum p_{T} and rapidity y. N_{evt} is the total number of Pb+Pb collisions in a chosen centrality interval. Mean nuclear thickness function $\langle T_{\mathrm{AA}} \rangle$ provides normalisation. This normalisation is necessary due to proportionality of hard-processes in a nucleus-nucleus collision to the nuclear thickness function [19] leading to geometric enhancement. $R_{\mathrm{AA}} = 1$ means no suppression, the inclusive jet per event

yield in Pb+Pb collisions equals to the normalised inclusive jet cross-section in pp collisions.

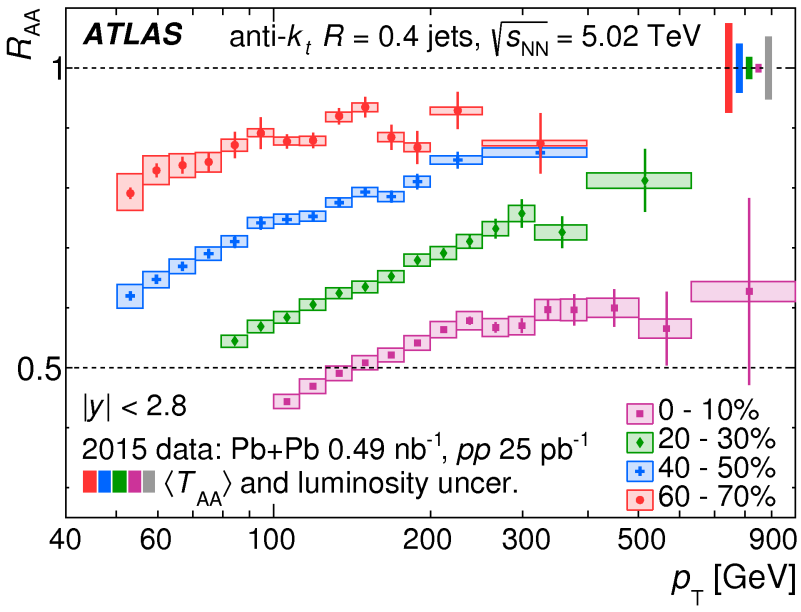

Figure 2.5: The R_{AA} values as a function of jet p_{T} for jets with $|y| < 2.8$ for four centrality intervals 0–10%, 20–30%, 40–50%, 60–70%). The error bars represent statistical uncertainties, the shaded boxes around the data points represent bin-wise correlated systematic uncertainties. The coloured and grey shaded boxes at $R_{\mathrm{AA}} = 1$ represent fractional $\langle T_{\mathrm{AA}} \rangle$ and pp luminosity uncertainties, respectively, which both affect the overall normalisation of the result. The horizontal size of error boxes represents the width of the p_{T} interval. Figure and caption taken from [23].

The nuclear modification factor R_{AA} evaluated as a function of jet p_{T} is presented in Figure 2.5 showing four centrality selections. These results were obtained by ATLAS Experiment measurement [23] of Pb+Pb data collected at $\sqrt{s_{\mathrm{NN}}} = 5.02\,\mathrm{TeV}$ in 2015 and pp data at $\sqrt{s} = 5.02\,\mathrm{TeV}$ from the same year. Clear centrality dependence of the R_{AA} is observed. A suppression of jet production in Pb+Pb collisions relative to pp collisions by a factor of two is observed in the centrality interval 0–10%. R_{AA} grows slowly with increasing jet p_{T}.

2.3 Quarkonia production

Quarkonia are bound states of quark anti-quark pair $q\bar{q}$ of the same flavour. Therefore quarkonia are flavourless $q\bar{q}$ bound states. Quarkonia belong to the group of hadrons called mesons. Term quarkonia is used only for $q\bar{q}$ bound states formed by heavy quarks excluding the top quark, i.e. c, b. The top quarks decay faster than the formation of the bound state is done. $c\bar{c}$ bound states are called *charmonia* and $b\bar{b}$ bound states are called *bottomonia*.

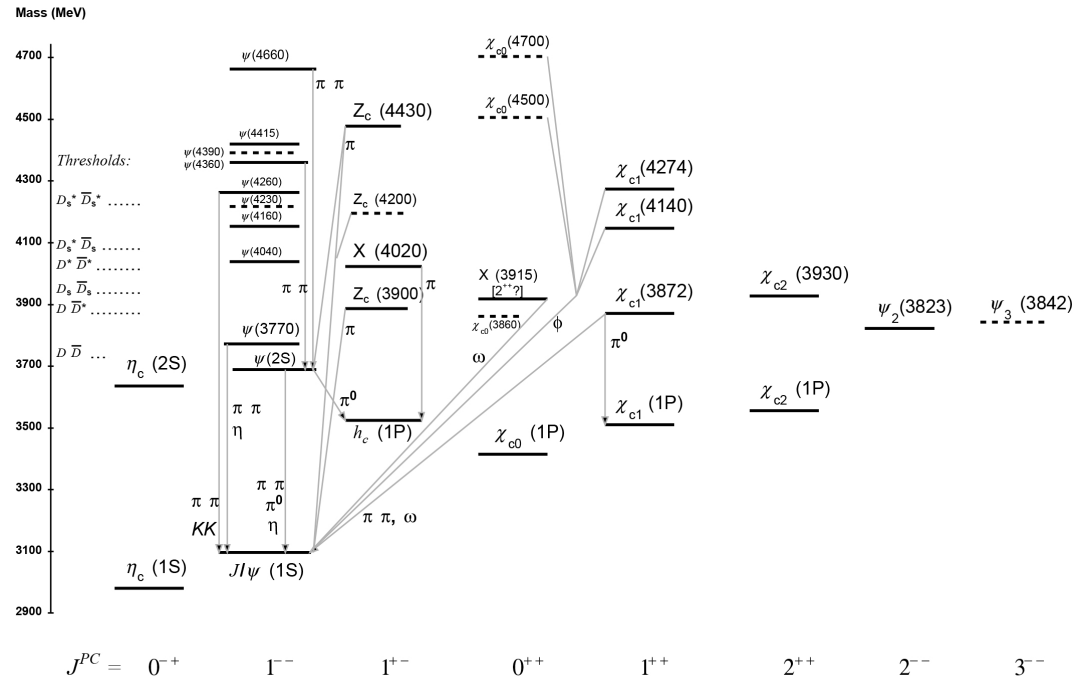

Figure 2.6: The level scheme of the charmonia system is presented. States included in Summary Tables in Particle Data Group [11] are shown with solid lines. Selected states not included in the Summary Tables are shown with dotted lines. The arrows indicate the most dominant hadronic transitions. Single-photon transitions, including $\psi(\mathrm{nS}) \to \gamma\eta_c(\mathrm{mS})$, $\psi(\mathrm{nS}) \to \gamma\chi_{cJ}(\mathrm{mP})$, $\chi_{cJ}(1\mathrm{P}) \to \gamma J/\psi$, and $\eta_c(2\mathrm{S}) \to \gamma J/\psi$ are omitted for clarity. Figure taken from [11].

J/ψ meson, sometimes denoted as $\psi(1\mathrm{S})$, was the first discovered charmonium. It was discovered in 1974 independently by two research groups, one at SLAC and one at BNL. J/ψ meson is considered as a ground state charmonium. It has rest mass of $m = 3096.900 \pm 0.006\,\mathrm{MeV}$ and decay width $\Gamma = 92.9 \pm 2.8\,\mathrm{keV}$ [11]. The first excited state is denoted $\psi(2\mathrm{S})$, or ψ', having rest mass $m = 3686.097 \pm 0.025\,\mathrm{MeV}$ and decay width $\Gamma = 294 \pm 8\,\mathrm{keV}$. The level scheme of the charmonia system is shown in Figure 2.6. The name of the state is determined by its quantum numbers J^{PC}, where J denotes the total angular momentum of $q\bar{q}$ system, P parity conjugation, and C charge conjugation. Standard spectroscopic notation $(2S+1)LJ$ is used. Here S, L, and J are the spin, orbital, and total angular momenta of the $q\bar{q}$ system.

Υ (*Upsilon*) meson was the first discovered bottomonium in 1977 in Fermilab. Υ is considered a ground state bottomonium, having rest mass $m = 9460.30 \pm 0.26\,\mathrm{MeV}$ and decay width $\Gamma = 54.02 \pm 1.25\,\mathrm{keV}$. For more details about quarkonia systems, see e.g. [11].

Quarkonia production is often described in a non-relativistic QCD framework (NRQCD)[24]. The colour structure of the $q\bar{q}$ pair allows the production of colour singlet and colour octet states, respectively. However, colour confinement ensures that mesons exist only as colour singlets. Therefore, colour octet states are non-physical intermediate states called Fock states. This intermediate state of $q\bar{q}$ pair

then evolves into a physical quarkonium by non-perturbative evolution of long-distance matrix elements. The intermediate $q\bar{q}$ pair in the octet state changes its colour and spin by radiating gluons. Singlet states are assumed to keep these quantum numbers unchanged when evolving to the physical state.

A complete description of quarkonia production is still a big unknown, but there are models approaches [25] which model the quarkonia production:

1. *The Colour-Singlet model (CSM)* - this model assumes direct production of colour singlet charmonia. In other words, it assumes that the quantum state of the $q\bar{q}$ pair does not evolve between its production and hadronization.

2. *The Colour-Octet Mechanism (COM)* - it assumes production of $q\bar{q}$ pair in intermediate colour octet states, so-called Fock states. These octet states transit to physical singlet states by the emission of soft gluons.

3. *The Colour-Evaporation Model (CEM)* - it assumes that quantum number of $q\bar{q}$ pair is randomised due too many gluons during hadronization.

Quarkonia are also produced by deexcitation of its higher excited states, so-called *feed down* [26]. Compared to bottomonia, charmonia are also produced by weak decay of B-hadrons (hadrons containing b quark). This thesis aims to study charmonia production. Therefore, from now on, only charmonia, namely J/ψ and ψ(2S), will be discussed. ψ(nS) denotes J/ψ for $n = 1$ and ψ(2S) for $n = 2$, respectively, where n denotes the radial quantum number. Therefore, ψ(2S) is so-called *radially excited state* of J/ψ. Charmonia produced via decays of B-hadrons are called as *non-prompt*, otherwise they are called *prompt*.

In Figures 2.7 and 2.8 one can find Feynman diagrams of CSM and COM contributions, respectively, to $c\bar{c}$ hadro-production. For the simplicity, $c\bar{c}(1)$ denotes singlet state, and $c\bar{c}(8)$ denotes octet state, respectively. Note that direct production of J/ψ and χ_{1c} via $gg \to J/\psi$ and $gg \to \chi_{1c}$ are forbidden. Corresponding u-channel diagrams, and radiative corrections are omitted for clarity.

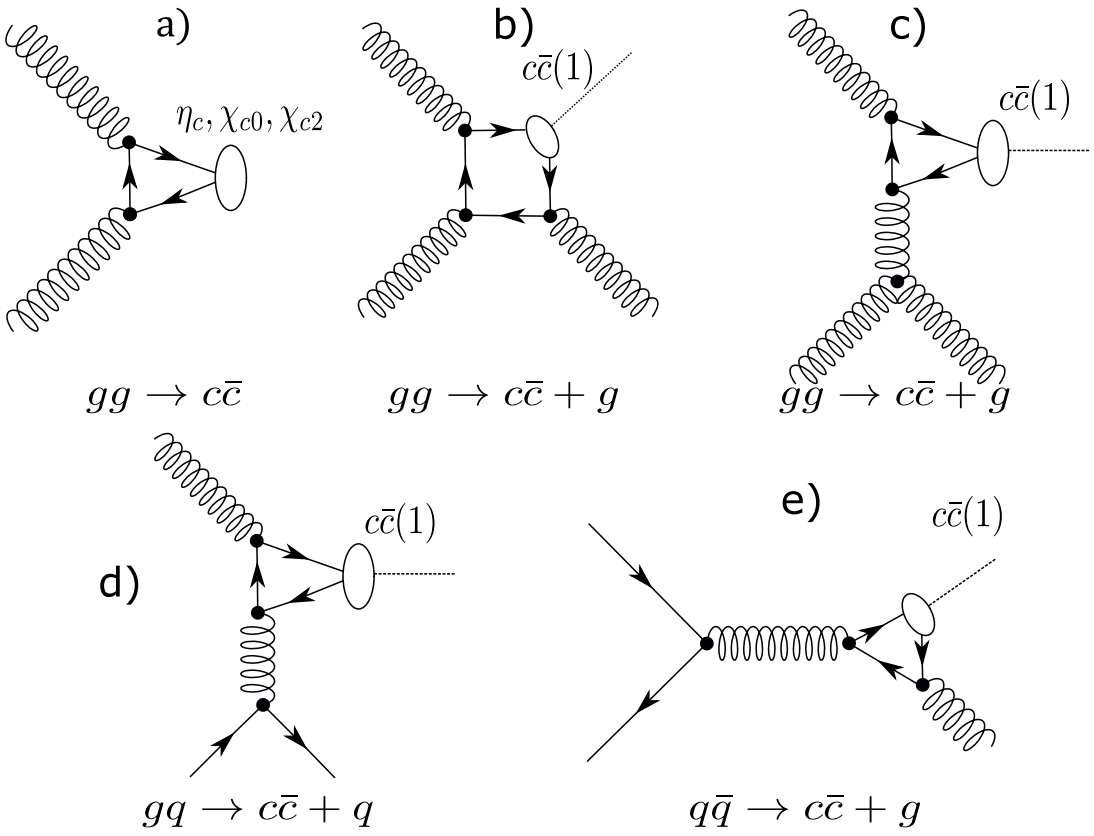

Figure 2.7: Representative diagrams contributing to $c\bar{c}$ hadro-production via CSM channels at α_S^2 (a), α_S^3 (b,c,d,e). Corresponding u-channel diagrams, and radiative corrections are omitted for clarity.

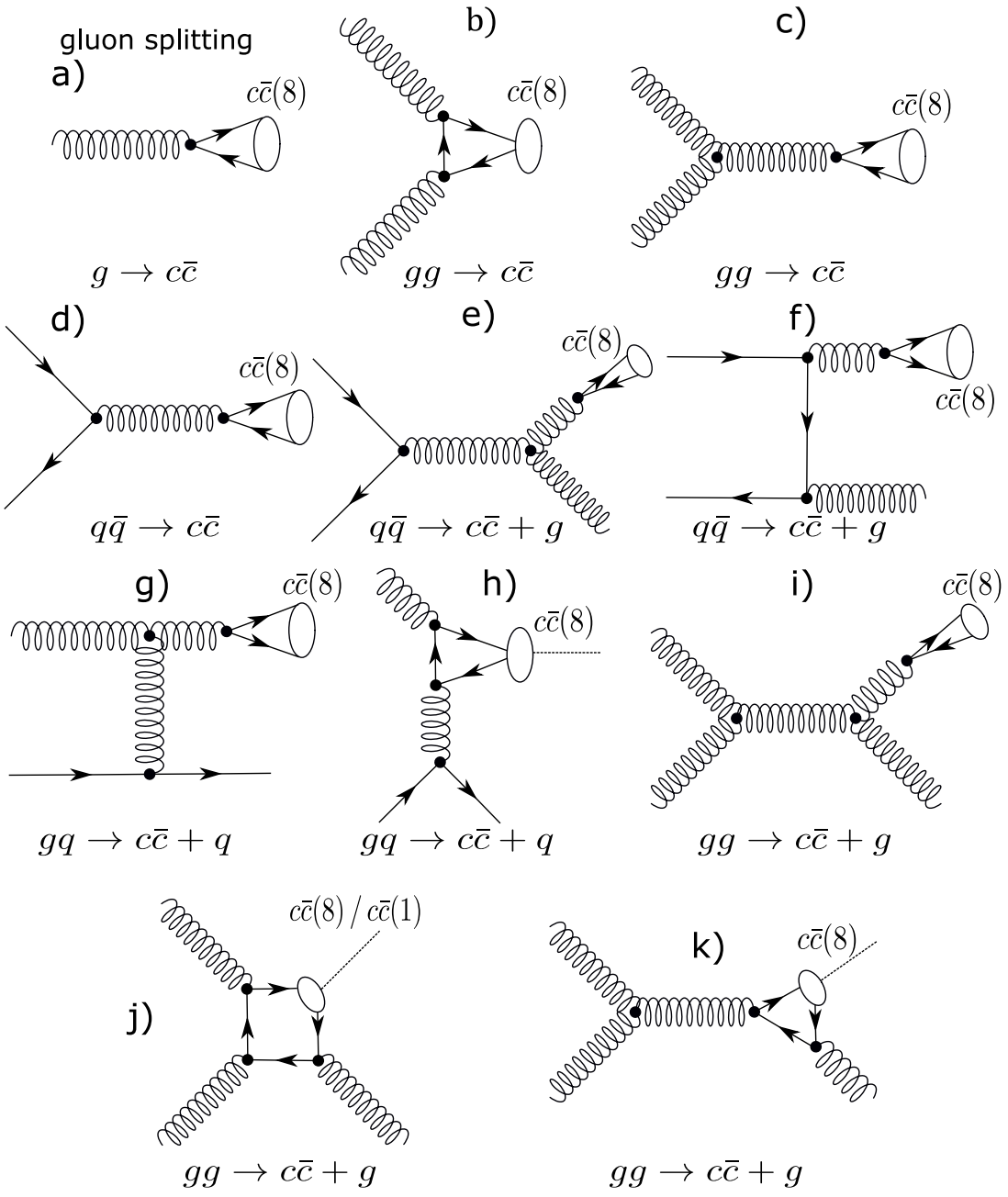

Figure 2.8: (a) Feynman diagram of the gluon splitting. Representative diagrams contributing to $c\bar{c}$ hadro-production via COM channels at α_S^2 (b,c,d), α_S^3 (e–k). Corresponding u-channel diagrams, and radiative corrections are omitted for clarity.

Note that COM provides contributions from the order α_S^2 compared to the CSM. To describe charmonia production at least at low p_{T} (below 100 GeV), one has to combine both models. However, these models cannot fully describe total cross-section at high p_{T} region. CEM also cannot fully describe total cross-section of the J/ψ production in the full measured p_{T} region. One of the main problems of CEM is that this model cannot describe yields of the excited states. For more details about CSM, COM and CEM models of charmonia production, see Refs. [25, 27].

2.3.1 Nuclear modification factor R_{AA}

When non-physical intermediate $c\bar{c}$ pair propagates through QGP during its evolution to the physical state, colour screening may occur. Colour screening in a deconfined medium weakens the strong interaction between c and $\bar{c}$ quarks at small distances. Colour screening leads to a dissociation of quarkonium bound state. This can be observed as a charmonia suppression. The suppression of the charmonia production should be larger for $\psi(2\mathrm{S})$ than for J/ψ due to smaller binding energy. This phenomenon is called as *sequential melting* [26]. It is believed that the suppression of different charmonium states could provide information about temperature and degree of deconfinement of the QGP [28].

R_{AA} is also defined in order to quantify the suppression of the charmonia production in heavy-ion collisions. R_{AA} is defined in the same way as it was defined for jets in the section 2.2,

$$R_{\mathrm{AA}} = \frac{\frac{1}{N_{\mathrm{evt}}} \frac{\mathrm{d}^2 N_{\psi(\mathrm{nS})}}{\mathrm{d}p_{\mathrm{T}}\mathrm{d}y}\Big|_{\mathrm{cent}}}{\langle T_{\mathrm{AA}} \rangle \frac{\mathrm{d}^2 \sigma_{\psi(\mathrm{nS})}}{\mathrm{d}p_{\mathrm{T}}\mathrm{d}y}\Big|_{pp}}, \tag{2.9}$$

where $N_{\psi(\mathrm{nS})}$ and $\sigma_{\psi(\mathrm{nS})}$ is the charmonia yield in Pb+Pb collisions and the charmonia cross-section in pp collisions, respectively, both measured as a function of transverse momentum p_{T} and rapidity y.

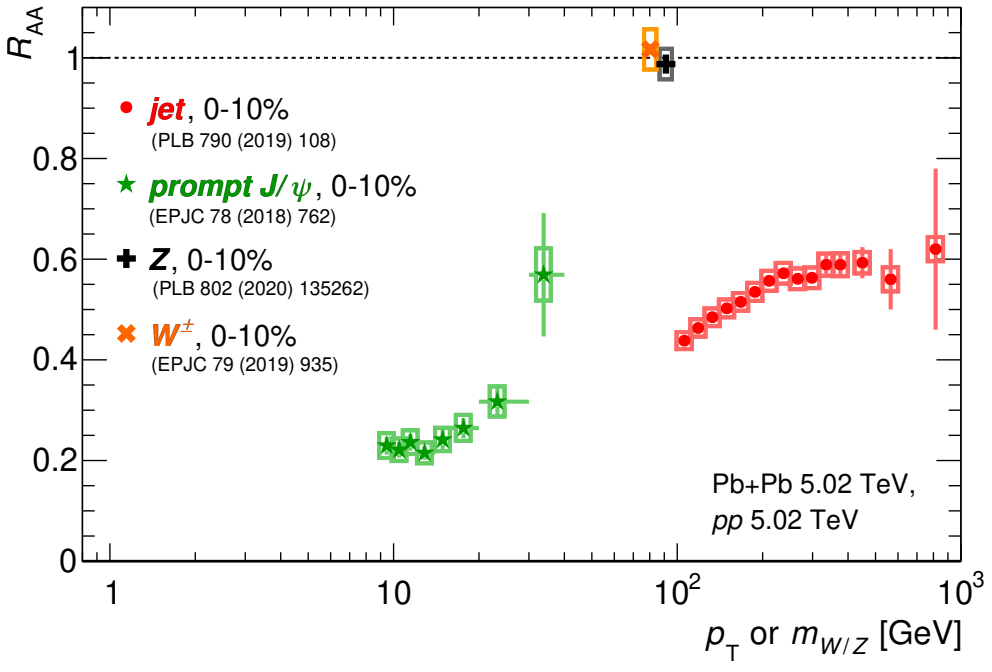

Figure 2.9: Compilation of results for the nuclear modification factor R_{AA} vs. p_{T} or $m_{\mathrm{W/Z}}$ in different channels from the Run 2 Pb+Pb and pp data. Results are shown for anti-k_{T} $R = 0.4$ jets (red circles), prompt J/ψ's (green stars), for Z bosons (black crosses, plotted at the Z boson mass) and for $W^{\pm}$ bosons (orange crosses, plotted at the W boson mass). The statistical uncertainties are shown as vertical bars and the total systematic uncertainties, including pp luminosity and T_{AA} uncertainties, are shown as boxes. Results from Refs. [23, 29, 30, 31]

Figure 2.9 shows R_{AA} as a function of p_{T} for jets, prompt J/ψ, for Z bosons and for W bosons for centrality interval $0-10\%$. Suppression by a factor of about 4 or 5 for prompt J/ψ mesons is observed. Jet suppression by a factor of 2 is observed. As expected, no suppression of the production of the Z boson and for W boson is observed since these bosons and their measured decay products do not interact strongly.

3. Experimental setup

In this chapter, the *Large Hadron Collider (LHC)* at CERN and *A Torroidal LHC ApparatuS (ATLAS)* are introduced. The data collected by ATLAS are used in this thesis. Detailed description of ATLAS and LHC can be found in Refs. [32, 33, 34, 35].

3.1 The Large Hadron Collider

The Large Hadron Collider (LHC) is the largest and most powerful circular particle accelerator in the world, which is located near Geneva, Switzerland. LHC is a synchrotron that consists of a 27-kilometre ring equipped of superconducting magnets to accelerate particles. LHC is a collider, in other words it consists of two separate beam pipes where protons are accelerated in opposite directions to a velocity close to the speed of the light.

LHC has been running since 2008 when it started to accelerate proton beams in addition, since 2010, lead ions are accelerated too. LHC is built in the tunnel that was previously used for *Large Electron-Positron Collider (LEP)* thus it is connected to almost every smaller accelerator in CERN. The whole scheme of CERN accelerators is shown in figure 3.1.

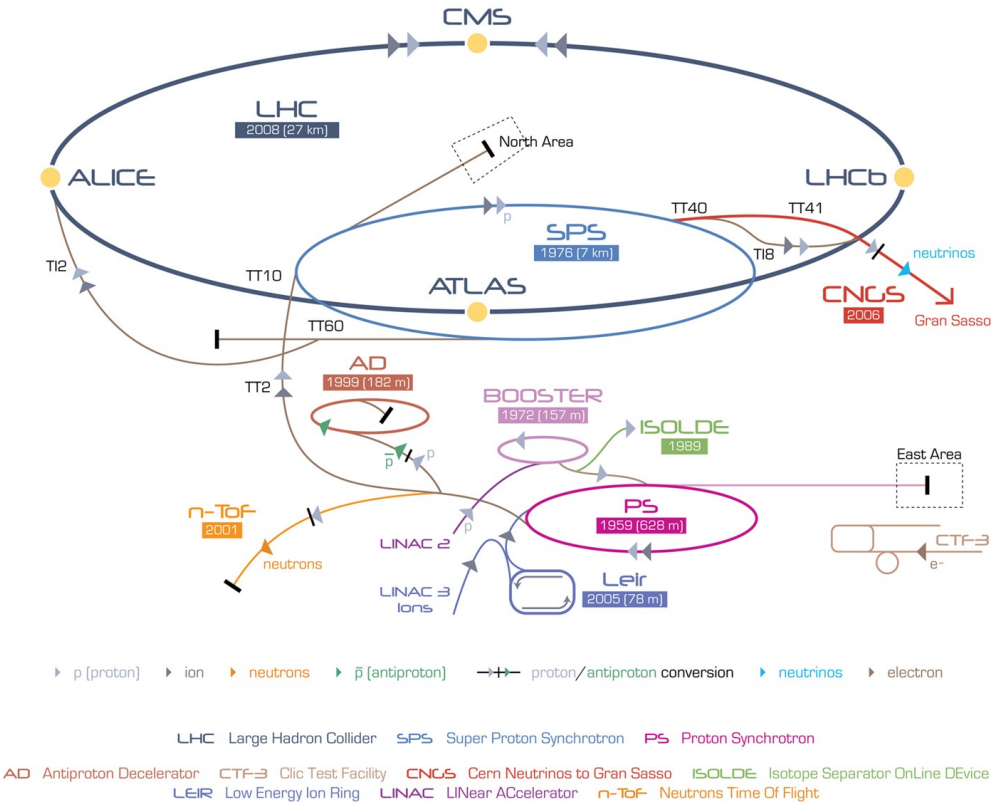

Figure 3.1: Scheme of accelerators located in CERN. Taken from [36].

As it was said, LHC is a particle collider. Particle beams are kept in the accelerator ring by a strong magnetic field (induction up to 8 T) maintained by

1232 dipole magnets, which bend the beams, and 392 quadrupole magnets focusing the beams. There are four points where another type of magnets is used to make particle beams collide at the LHC. These so-called interaction points correspond to locations of the largest particle physics experiments (particle detectors) at the LHC - *A Toroidal LHC ApparatuS (ATLAS)*, *Compact Muon Solenoid (CMS)*, *A Large Ion Collider Experiment (ALICE)* and *Large Hadron Collider beauty (LHCb)*.

The ATLAS and CMS are general-purpose particle physics experiments that are designed to exploit the full potential of the LHC, ALICE is designed to study primarily physics of heavy-ion collisions and LHCb studies primarily b-hadrons.

There are another three experiments at the LHC with a specific purpose: *TOTal Elastic and diffractive cross section Measurement experiment (TOTEM)*, which measures cross-sections and studies elastic scattering and diffractive processes, *Monopole and Exotics Detector at the LHC (MoEDAL)*, which searches for magnetic monopoles and *Large Hadron Collider forward (LHCf)*, which is focused on astroparticle physics.

As previously mentioned, the main physics program is focused on proton-proton collisions (*pp*-collisions). The protons' way to LHC starts at linear accelerator LINAC 2. After that, protons go through Booster to *Proton Synchroton (PS)* and *Super Proton Synchrotron (SPS)*. Afterwards protons are injected to LHC to collide with center-of-mass energy $\sqrt{s} = 14\,\text{TeV}$ per beam. The so-called injector chain is very similar to the injector chain for lead-lead collisions. Typically, heavy-ion collisions are performed at the LHC using $^{208}\text{Pb}^{82+}$ ions. $^{208}\text{Pb}^{27+}$ ions are extracted from the source before injection. These ions are accelerated and stripped (conversion to $^{208}\text{Pb}^{54+}$) at LINAC 3. After that, lead ions go through *Low Energy Ion Ring (LEIR)* and SPS (now fully stripped) to the LHC where they collide with center-of-mass energy $\sqrt{s_{NN}} = 5.02\,\text{TeV}$ per nucleon.

Particle colliders do not accelerate single particles but rather bunches of particles that consist of thousands of billions of particles. One bunch consists of $1.15 \cdot 10^{11}$ protons and $7 \cdot 10^7$ lead ions, respectively. To quantify the performance of collider, it is necessary to define instantaneous *luminosity* $\mathcal{L}$ and *integrated luminosity* L [11] which quantify the performance of a particle accelerator. Instantaneous luminosity for head-on collisions of two bunches of particles is defined as

$$\mathcal{L} = f_{coll} \frac{n_1 n_2}{4\pi\sigma_x\sigma_y}, \tag{3.1}$$

where f_{coll} characterizes frequency of head-on collisions, n_1 and n_2 are numbers of particles contained in bunches, σ_x and σ_y characterize the transverse beam size in the horizontal and vertical directions, respectively, at the interaction point. Integrated luminosity is defined as integral of $\mathcal{L}$ over the time

$$L = \int \mathcal{L}\mathrm{d}t. \tag{3.2}$$

The number of events N_{exp} is the product of the cross-section of interest σ_{exp} and integrated luminosity L:

$$N_{exp} = \sigma_{exp} L. \tag{3.3}$$

Typically one month per year, heavy-ion collisions are performed at the LHC using lead nuclei. Sometimes, other nuclei are used, e.g. xenon.

3.2 The ATLAS Experiment

ATLAS is the biggest of the seven detectors at the LHC, together with the CMS experiment belonging to general-purpose detectors that investigate both *pp* and Pb+Pb collisions. ATLAS has massive dimensions. It weighs over 7000 tons, it has 46 meters in length, 25 meters in height, and it is placed 100 meters below the ground level. It is designed to detect hundreds of million collisions per second, but the trigger system chooses only interesting events which will be stored in CERN Data Center for detailed analysis.

ATLAS detector has a cylindrical shape with an interaction point in its centre. It is composed of different sub-detectors ("slices") to detect all kinds of particles to reconstruct the primary event completely. Detector composition is shown in Figure 3.2.

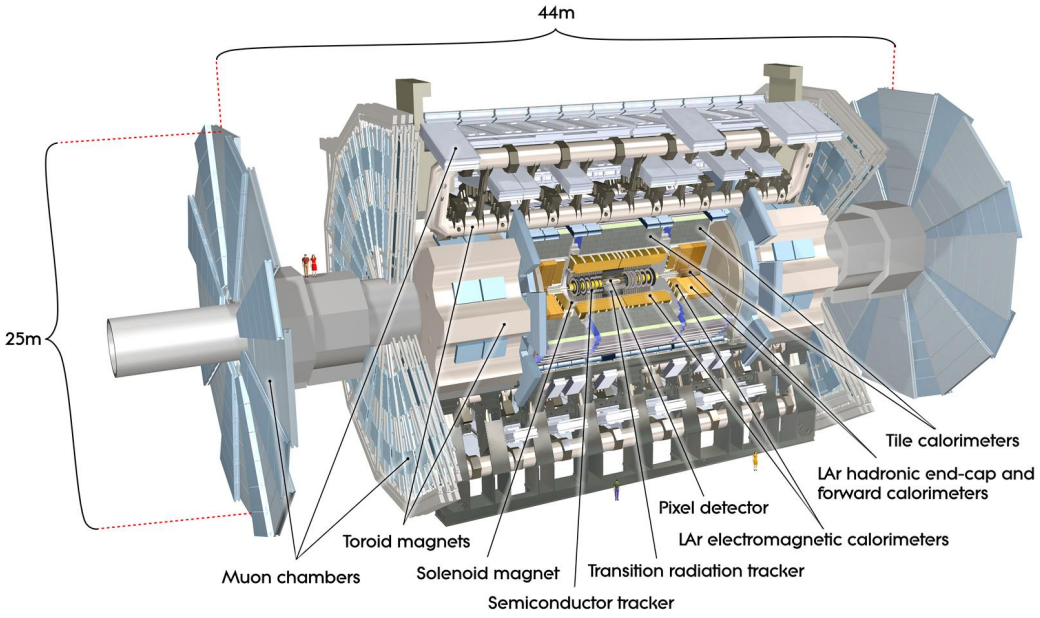

Figure 3.2: Cut-away view of the ATLAS detector. Figure taken from [37].

3.2.1 ATLAS coordinate system and kinematics

ATLAS uses a right-handed coordinate system with its origin at the interaction point in the centre of the detector and the z-axis along the beam pipe. The x-axis points to the centre of the LHC ring, and the y-axis points upwards. Assuming ATLAS axial symmetry, the azimuthal angle ϕ is measured around the z-axis, which means $\phi = 0$ corresponds to the positive x-axis. By definition, polar angle θ is the angle from the beam axis which means that θ equals 0 or π along the beam axis. In the following paragraphs, quantities used to describe kinematics of the collisions are introduced.

Let us assume a particle with four-momentum [1] $\boldsymbol{P} = (E, \vec{p})$, where E denotes its energy and $\vec{p}$ its momentum vector. Now it is useful to define *rapidity* y [11]

[1] In this thesis natural units are used, $\hbar = c = 1$.

as follows

$$y \equiv \frac{1}{2}\frac{E + p_z}{E - p_z}. \tag{3.4}$$

It can be shown, that rapidity is not Lorentz-invariant quantity, but it is additive under the boosts along z-axis. For $|\vec{p}| \gg m$, the rapidity may be expanded and simplified to obtain *pseudorapidity* η [11] defined as

$$\eta \equiv -\ln\left[\tan\left(\frac{\theta}{2}\right)\right], \tag{3.5}$$

therefore pseudorapity is a spatial coordinate describing the angle between the particle momentum $\vec{p}$ and the positive direction of the beam axis (z-axis). To obtain complete kinematic description of the particle we may define *transverse momentum* p_T as the projection of momentum vector to the x-y plane

$$p_\mathrm{T} = |\vec{p}| \sin\theta = \sqrt{p_x^2 + p_y^2}. \tag{3.6}$$

We can also define *transverse energy* E_T using previous definition of transverse momentum as

$$E_\mathrm{T} = E \sin\theta. \tag{3.7}$$

p_T, E_T, ϕ and y (or p_T, m, ϕ and y) now fully characterize the particle measured in detector. Using these variables, we can rewrite the cross section of measured process in the invariant form as it is mentioned in [11] as follows

$$E\frac{\mathrm{d}^3\sigma}{\mathrm{d}\vec{p}} = \frac{\mathrm{d}^3\sigma}{\mathrm{d}\phi\,\mathrm{d}y\,p_\mathrm{T}\,\mathrm{d}p_\mathrm{T}}. \tag{3.8}$$

Assuming two particles described by four-momenta $\boldsymbol{P}_1 = (E_1, \vec{p}_1)$, $\boldsymbol{P}_2 = (E_2, \vec{p}_2)$, center-of-mass energy $\sqrt{s}$ can be expressed in Lorentz-invariant form [11]

$$\sqrt{s} = \sqrt{(\boldsymbol{P}_1 + \boldsymbol{P}_2)^2} = \sqrt{(E_1 + E_2)^2 - |\vec{p}_1 + \vec{p}_2|^2}, \tag{3.9}$$

where s is the *Mandelstam variable*. Center-of-mass energy is related to invariant mass of system M as

$$M^2 = s = (E_1 + E_2)^2 - |\vec{p}_1 + \vec{p}_2|^2. \tag{3.10}$$

This quantity is essential for particle identification. During the acceleration of heavy-ions, only protons are accelerated, since neutrons do not have electric charge. One can introduce nucleon-nucleon center-of-mass energy $\sqrt{s_\mathrm{NN}}$ defined as

$$\sqrt{s_\mathrm{NN}} = 2E_p\frac{Z}{A}, \tag{3.11}$$

where A is number of nucleons in nuclei, Z is number of protons in nuclei and E_p is energy of fully accelerated proton by used accelerator.

3.2.2 ATLAS sub-detectors

Inner Detector

The Inner Detector (ID) is very compact and highly sensitive detector that consists of three different systems of sensors - *Pixel Detector (PD), Semiconductor Tracker (SCT)* and *Transition Radiation Tracker (TRT).* It is the innermost part of the ATLAS detector, and it is immersed in the solenoidal magnetic field of 2 T, which is generated by the central solenoid. ID has a cylindrical shape with a length of 6.2 m and a radius of 1.05 m. The ID is shown in Figure 3.3.

The ID is designed to measure the direction, momentum and charge of electrically charged particles, which allows reconstructing the paths of these particles and their origin - vertex. The ID provides these measurements within the pseudorapidity range $|\eta| < 2.5$.

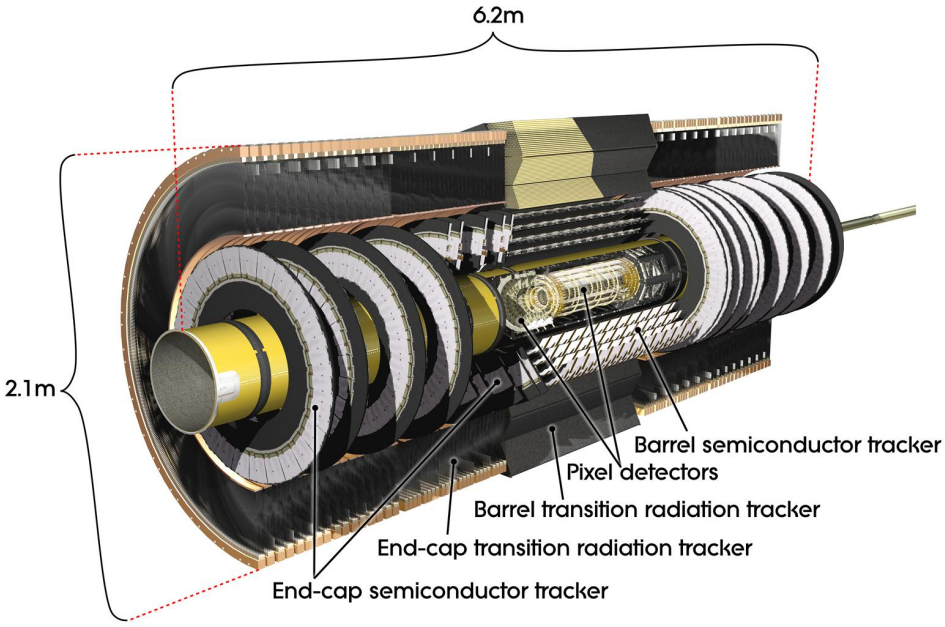

Figure 3.3: Cut-away view of the Inner Detector. Figure taken from [38].

- PD is the innermost part of the ID, and it is composed of 47 000 silicon pixels. In 2014, another layer was added to the PD, which is the closest one to the particle beam. It is called *Insertable B-Layer (IBL).*

- SCT is working on the same principle as PD, but it is composed of silicon strips to cover a larger area than PD. Each strip has dimensions 80 μm $\times$ 12 cm.

- TRT is the outermost part of the ID, which is composed of gaseous straws tubes.

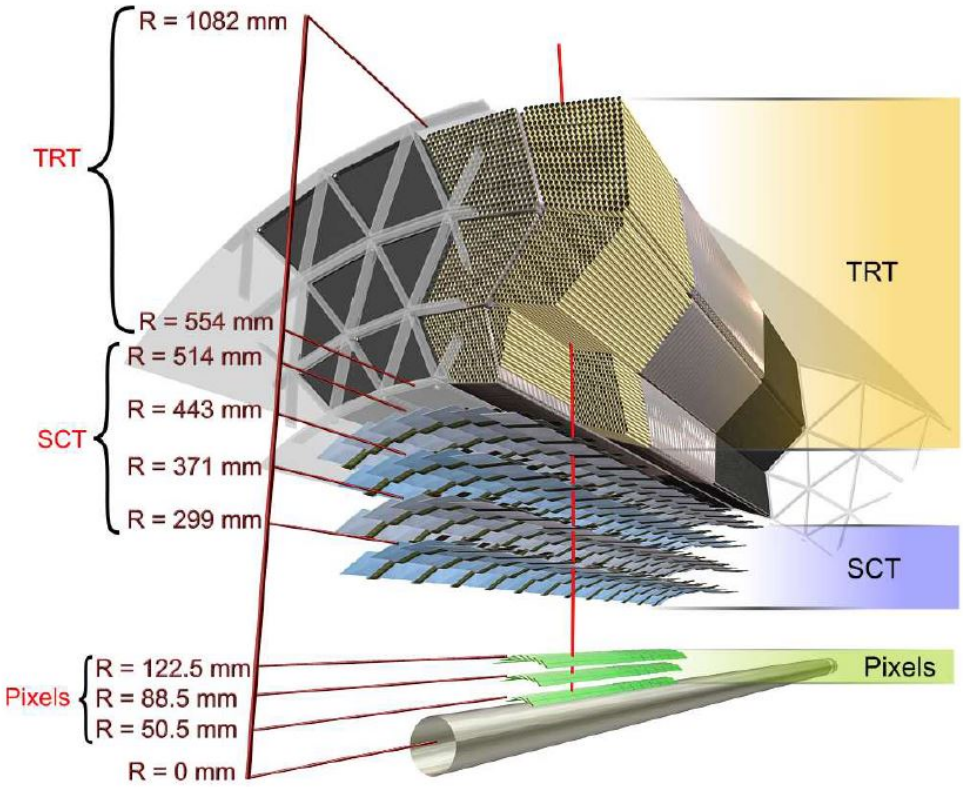

Figure 3.4: Detailed cut-away view of the Inner Detector. Figure taken from [35].

System of calorimeters

Calorimeter is a type of detector designed to stop the particles coming from a collision forcing them to deposit all of their energy. ATLAS calorimeters consist of the electromagnetic calorimeter and the hadronic calorimeter, each of these detects different particles. Any calorimeter has its "passive" medium, absorber, that absorbs particle energy such as metal layers, and on the other hand it has its "active" medium that detects particles.

A particle that strikes calorimeter creates an electromagnetic shower (particle interacting through the electromagnetic interaction), or it creates a hadronic shower (strongly interacting particle). ATLAS calorimetery is composed of electromagnetic calorimeter using liquid argon technology, the so-called *Liquid Argon (LAr) Calorimeter*, and hadronic calorimeter, *Tile Hadronic Calorimeter (TileCal)*.

- The LAr Calorimeter surrounds the ATLAS ID and measures the energy of electrons, protons and hadrons. It is composed of metal layers (tungsten, copper or lead) surrounded by liquid argon. As particles ionise liquid argon, we can measure the electric current that is produced. LAr covers the pseudorapidity range of $|\eta| < 3.2$ and LAr forward calorimeter (FCal) extend the pseudorapidity range to $|\eta| < 4.9$.

- The TileCal surrounds the LAr Calorimeter and measures the energy of hadrons using almost 420 000 plastic scintillator tiles. TileCal uses layers of steel as an absorber. As a particle strikes one of these layers, it generates a shower of new particles. After that, plastic scintillators produce photons,

as they are hit by charged particles, which are converted into an electric current (its intensity is proportional to the energy of the primary particle). TileCal covers the pseudorapidity range of $|\eta| < 1.7$.

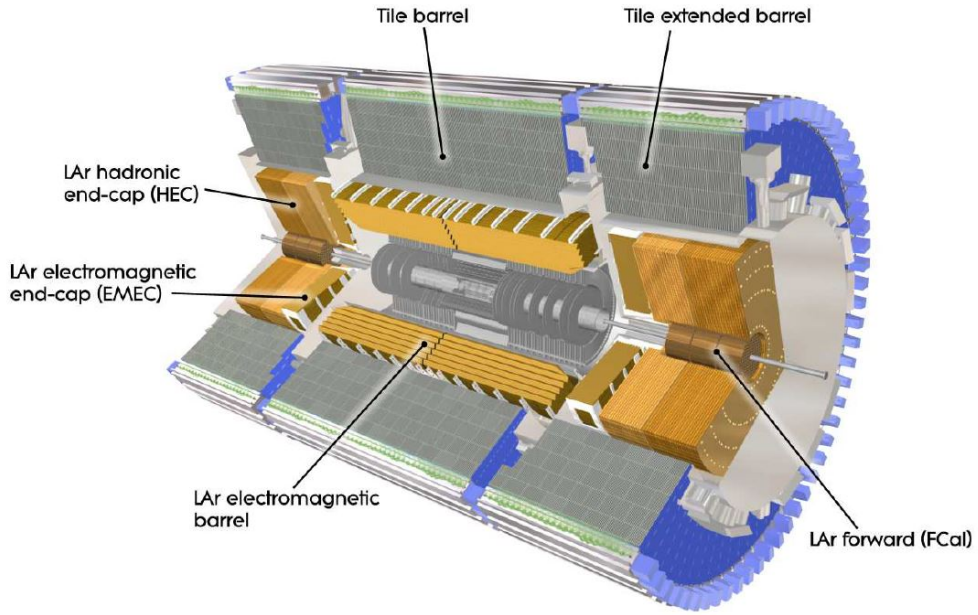

Figure 3.5: Cut-away view of the ATLAS calorimeter system. Figure taken from [35].

Muon Spectrometer

Muon Spectrometer is a part of the ATLAS detector used to detect muons. During many interesting events, muons are produced, but they almost do not interact with calorimeters because of their small cross-section for interaction with matter.

Muons charge and momenta are obtained by measuring sagitta of the muon trajectory produced by the magnetic field. Chambers are arranged such that their plane is roughly aligned with the bending plane of the magnet system. The "precision coordinate" is the coordinate perpendicular to the muon trajectory. The "second coordinate" is the coordinate orthogonal to the measurement plane.

It is made of almost 4000 individual muon chambers. The muon spectrometer has 4 subsections shown in Figure 3.6:

- *Thin Gap Chambers* are used for triggering and second coordinate measurement at the edge of the detector.
- *Resistive Plate Chambers* are used for triggering and second coordinate measurement in the central region.
- *Monitored Drift Tubes* measure curves of tracks.
- *Cathode Strip Chambers* are used to measure precision coordinates at the outer edge of the detector.

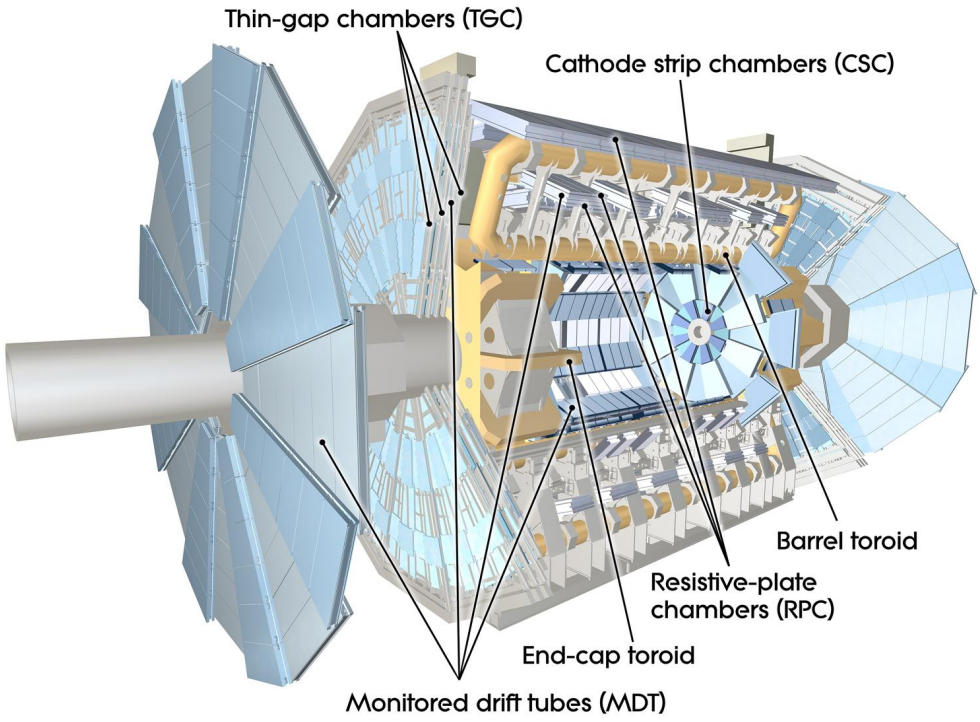

Figure 3.6: Cut-away view of the ATLAS muon spectrometer. Figure taken from [39].

Forward detectors

The Forward detectors are a group of detectors that are located far away from the interaction point. They are constructed for the measurement of particles at very small angles. One of the main tasks of these detectors is to measure luminosity in the interaction point precisely.

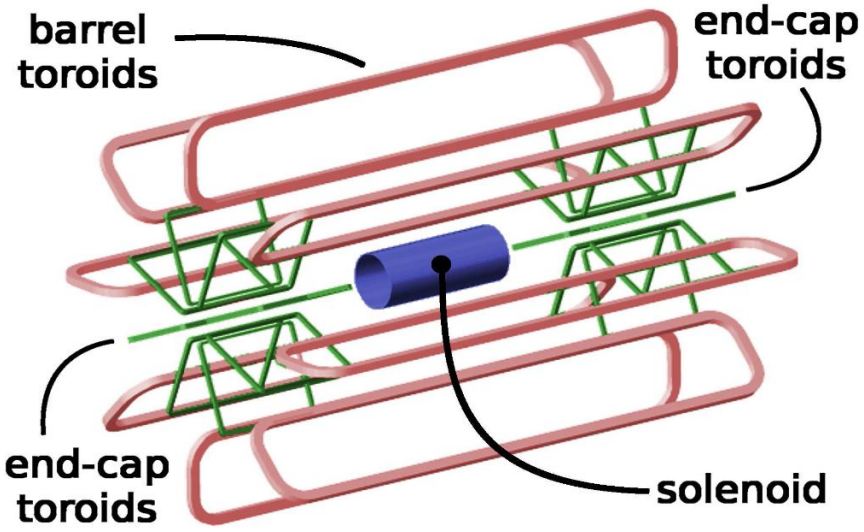

Figure 3.7: ATLAS Magnet system. Figure taken from [40].

Magnet system

One of parts of the ATLAS detector is the system of magnets (shown in Figure 3.7), which generates magnetic fields. The magnetic field is necessary to bend charged particle trajectories, which allows to measure the electric charge of charged particles and their momenta.

The ATLAS uses two types of superconducting magnet systems - solenoidal and toroidal. Central solenoid provides a 2 Tesla magnetic field in the Inner Detector. The outer toroidal magnetic field is provided by Barrel toroid (eight huge superconducting barrel loops) and by two end-cap toroidal magnets. Its magnetic field is not uniform, and it varies between 2 and 8 Tesla.

Trigger system

The ATLAS can observe up to 1.7 billion proton collisions every second, which represent about 60 million megabytes of data every second for storing. However, only a small amount of this data is needed for detailed analysis. Therefore the ATLAS Experiment has its a two-level trigger system, which provides the event selection.

- *Level-1 hardware trigger* is constructed with custom electronics, and it a hardware system. It works with information from the calorimeters and the Muon Spectrometer. This trigger decreases readout frequency to 100 kHz.
- *High Level Trigger* is a software trigger using a large CPU farm (this farm contains up to 40 000 CPUs). It provides a basic analysis of the stored events in a very short period. Therefore it decreases readout frequency to 1 kHz - these events are stored for detailed analysis.

4. Analysis of inclusive charmonia production in *pp* collisions at 5.02 TeV

In this chapter, the original results of this thesis are presented. These results are compared to Monte-Carlo (MC) simulations and original results from [2], which were published in 2018.

Section 4.1 describes MC simulations, which were done using Pythia 8.240 [41]. Section 4.2 is divided into several subsections describing main parts of analysis of data collected by the ATLAS Experiment. Section 4.4 describes fitting procedure using RooFit, and basic principles of the fit model used in analysis of the ATLAS data. Section 4.5 presents original results compared to MC simulations and data of *pp* collisions at $\sqrt{s} = 5.02\,\text{TeV}$ from 2015. In this thesis, we used the dataset containing 25 434 events of *pp* collisions at $\sqrt{s} = 5.02\,\text{TeV}$. Used dataset represents about 1 % of total collected luminosity in 2017 which was approximately $260\,\text{pb}^{-1}$. This dataset is denoted as the "ATLAS 2017 - Work in progress" (ATLAS 2017 - WIP).

4.1 MC simulations

Pythia [41] is a general-purpose Monte Carlo event generator used for the generation of high-energy collision events. It consists of a set of physics models describing the evolution from an elementary hard-scattering process to a complex multiparticle final state. This program combines rigorous physics theory like SM and phenomenological models (e.g. string fragmentation) with parameters determined from the data.

For this study Pythia sample containing 1 000 000 ψ(nS) candidates was generated using settings displayed below in Listing 4.1. Lines 2-8 provides basic Pythia settings. First center-of-mass energy was set to be $\sqrt{s} = 5.02\,\text{TeV}$ (this value is used for comparing results with J/ψ production published in [2]). Line 5 is setting random initial conditions using Pythia pseudo-random number generator for every event. Lines 12-20 provide tunning of measured parameters such as W boson width, etc. Further, lines 22-30 specify settings for PDFs multiparton-interactions and parton showers. In the end, lines 32-72 specify charmonia production in Pythia and choose only muon decay channel. This is described in details in sections 4.1.1 and 4.1.2.

Listing 4.1: Pythia settings

```
1  //Pythia settings
2  pythia.readString("Beams:eCM = 5020.");
3  pythia.readString("Main:numberOfEvents = 1000000");
4  pythia.readString("Main:timesAllowErrors = 10");
5  pythia.readString("Random:setSeed = on");
6  pythia.readString("Init:showAllSettings = off");
7  pythia.readString("Init:showChangedParticleData = on");
```

```
8   pythia.readString("Init:showAllParticleData = off");
9
10  // common ATLAS Pythia8
11  pythia.readString("Main:timesAllowErrors = 500");
12  pythia.readString("6:m0 = 172.5");
13  pythia.readString("23:m0 = 91.1876");
14  pythia.readString("23:mWidth = 2.4952");
15  pythia.readString("24:m0 = 80.399");
16  pythia.readString("24:mWidth = 2.085");
17  pythia.readString("StandardModel:sin2thetaW = 0.23113");
18  pythia.readString("StandardModel:sin2thetaWbar = 0.23146");
19  pythia.readString("ParticleDecays:limitTau0 = on");
20  pythia.readString("ParticleDecays:tau0Max = 10.0");
21
22  // PDF tune
23  pythia.readString("Tune:pp = 5");
24  pythia.readString("MultipartonInteractions:bProfile = 4");
25  pythia.readString("MultipartonInteractions:a1 = 0.00");
26  pythia.readString("MultipartonInteractions:pT0Ref = 2.13");
27  pythia.readString("MultipartonInteractions:ecmPow = 0.21");
28  pythia.readString("SpaceShower:rapidityOrder=0");
29
30  pythia.readString("PartonLevel:MPI = off");    // not setted
31
32  // Charmonia common
33  // Hard process
34  pythia.readString("PhaseSpace:pTHatMin = 5.");
35  pythia.readString("ParticleDecays:mixB = off");
36  pythia.readString("HadronLevel:all = on");
37
38  // Quarkonia production mode
39  pythia.readString("Charmonium:all = on");
40  pythia.readString("PhaseSpace:pTHatMinDiverge = 0.5");
41
42  // standard resonances decaying to J/Psi
43  pythia.readString("445:onMode = off");         // chi_2c
44  pythia.readString("445:onIfAny = 443");        // chi_2c
45  pythia.readString("10441:onMode = off");       // chi_0c
46  pythia.readString("10441:onIfAny = 443");      // chi_0c
47  pythia.readString("10443:onMode = off");       // h_1c
48  pythia.readString("10443:onIfAny = 443");      // h_1c
49  pythia.readString("20443:onMode = off");       // chi_1c
50  pythia.readString("20443:onIfAny = 443");      // chi_1c
51
52   // color triplet resonances decaying to J/Psi
53  pythia.readString("9940003:onMode = off");
54  pythia.readString("9940003:onIfAny = 443");
55  pythia.readString("9941003:onMode = off");
```

```
56    pythia.readString("9941003:onIfAny = 443");
57    pythia.readString("9942003:onMode = off");
58    pythia.readString("9942003:onIfAny = 443");
59
60    // color triplet resonances decaying to Psi(2S)
61    pythia.readString("9940103:onMode = off");
62    pythia.readString("9940103:onIfAny = 100443");
63    pythia.readString("9941103:onMode = off");
64    pythia.readString("9941103:onIfAny = 100443");
65    pythia.readString("9942103:onMode = off");
66    pythia.readString("9942103:onIfAny = 100443");
67
68    // signal
69    pythia.readString("443:onMode = off");          // J/Psi
70    pythia.readString("443:onIfAny = 13");
71    pythia.readString("100443:onMode = off");       // Psi(2S)
72    pythia.readString("100443:onIfAny = 13");
```

4.1.1 Charmonia production in Pythia

In Pythia there are three main sources of ψ(nS) production [42]

1. Decays of B mesons and baryons.

2. Parton-shower evolution, where produced c and $\bar{\text{c}}$ quark pair in two different branchings collapse to a single particle.

3. Direct production, where c quark loop couples to gluons and c$\bar{\text{c}}$ bound state. Higher-lying states may decay to ψ(nS) (see Figure 2.6).

In this study of MC charmonia production, the production of charmonia via decays of B mesons and baryons is avoided. Charmonia produced via decays of B mesons and hadrons are so-called *non-prompt*; otherwise, they are called *prompt*.

In Pythia charmonia are produced using colour singlet and colour-octet mechanisms via different Fock states, which are written in Table 4.1. The production in these channels is compared in terms of the number of recorded events in a given channel divided by the total number of events (relative production). In order to obtain results for this table, 1 000 000 events were generated.

To describe produced $c\bar{c}$ pair state the spectroscopic notation *(2S + 1)LJ* is used, where S is the spin of pair, L is the orbital angular momentum of pair and J is the total angular momentum of pair. The term in round-brackets specifies the physical state, while the term in square-brackets specifies Fock state (intermediate state) through which $c\bar{c}$ evolves to the physical state. (1) within the square-brackets of the Fock state denotes singlet-state and (8) denotes octet-state. E.g. $c\bar{c}$(3S1)[3S1(8)] denotes the physical state $c\bar{c}$(3S1) produced from the $c\bar{c}$[3S1(8)] octet state. The number 3 denotes, using notation $(2S+1)$, that the $c\bar{c}$ pair has spin one $S = 1$. S denotes it is a state with $L = 0$ and the number 1 denotes that it is a state with $J = 1$. These octet-states decay exclusively to physical charmonium radiating soft gluons.

Table 4.1 also provides connection between spectroscopic notation used in PYTHIA and well known names of $c\bar{c}$ states. (3S1) denotes J/ψ and its radially excited states such as $\psi(2S)$. (3PJ) denotes χ_c states with all allowed values of quantum number J, and (3DJ) denotes $\psi(3770)$.

Table 4.1: Relative production of charmonia produced in PYTHIA via different production channels.

No.	Subprocess	Rel. prod. [%]	Physical $c\bar{c}$
1	$gg \to c\bar{c}(3S1)[3S1(1)]g$	0.42	$J/\psi, \psi(2S)$
2	$gg \to c\bar{c}(3S1)[3S1(8)]g$	15.86	$J/\psi, \psi(2S)$
3	$qg \to c\bar{c}(3S1)[3S1(8)]q$		
4	$q\bar{q} \to c\bar{c}(3S1)[3S1(8)]g$		
5	$gg \to c\bar{c}(3S1)[1S0(8)]g$	2.61	$J/\psi, \psi(2S)$
6	$qg \to c\bar{c}(3S1)[1S0(8)]q$		
7	$q\bar{q} \to c\bar{c}(3S1)[1S0(8)]g$		
8	$gg \to c\bar{c}(3S1)[3PJ(8)]g$	3.26	$J/\psi, \psi(2S)$
9	$qg \to c\bar{c}(3S1)[3PJ(8)]q$		
10	$q\bar{q} \to c\bar{c}(3S1)[3PJ(8)]g$		
11	$gg \to c\bar{c}(3S1)[3S1(1)]\gamma$	0.02	$J/\psi, \psi(2S)$
12	$gg \to c\bar{c}(3DJ)[3DJ(1)]g$	0.01	$\psi(3770)$
13	$gg \to c\bar{c}(3DJ)[3PJ(8)]g$	1.31	$\psi(3770)$
14	$qg \to c\bar{c}(3DJ)[3PJ(8)]q$		
15	$q\bar{q} \to c\bar{c}(3DJ)[3PJ(8)]g$		
16	$gg \to c\bar{c}(3PJ)[3PJ(1)]g$	70.06	$\chi_{0c}, \chi_{1c}, \chi_{2c}, h_{1c}$
17	$qg \to c\bar{c}(3PJ)[3PJ(1)]q$		
18	$q\bar{q} \to c\bar{c}(3PJ)[3PJ(1)]g$		
19	$gg \to c\bar{c}(3PJ)[3S1(8)]g$	6.44	$\chi_{0c}, \chi_{1c}, \chi_{2c}, h_{1c}$
20	$qg \to c\bar{c}(3PJ)[3S1(8)]q$		
21	$q\bar{q} \to c\bar{c}(3PJ)[3S1(8)]g$		
22	$gg \to 2\,c\bar{c}(3S1)[3S1(1)]g$	0.01	$J/\psi, \psi(2S)$
23	$q\bar{q} \to 2\,c\bar{c}(3S1)[3S1(1)]g$	0.01	$J/\psi, \psi(2S)$

It is clearly seen that the most dominant subprocesses are direct production of $c\bar{c}(3S1)$ physical states such as χ_c states.

4.1.2 Kinematics of charmonia

The kinematics of charmonia was studied for J/ψ and $\psi(2S)$. The distribution of the invariant mass of dimuon candidates $m_{\mu\mu}$ is plotted in Figure 4.1 to control selection criteria. In this figure, only two peaks are clearly seen. First peak is located at 3.1 GeV corresponding to J/ψ and the second peak is visible at 3.7 GeV corresponding to $\psi(2S)$. The dimuon candidates, and J/ψ and $\psi(2S)$ mesons, respectively, generated in PYTHIA were identified using particle ID code common to majority of Monte Carlo generators [11]. The kinematics of charmonia was studied in two samples, both consisting of 10^6 events. Both samples were generated using settings from Listing 4.1. The first sample was used to study dimuon candidates produced via decays of J/ψ and $\psi(2S)$. The second sample

was used to study J/ψ and $\psi(2S)$ directly identified by the particle identification code (PID).

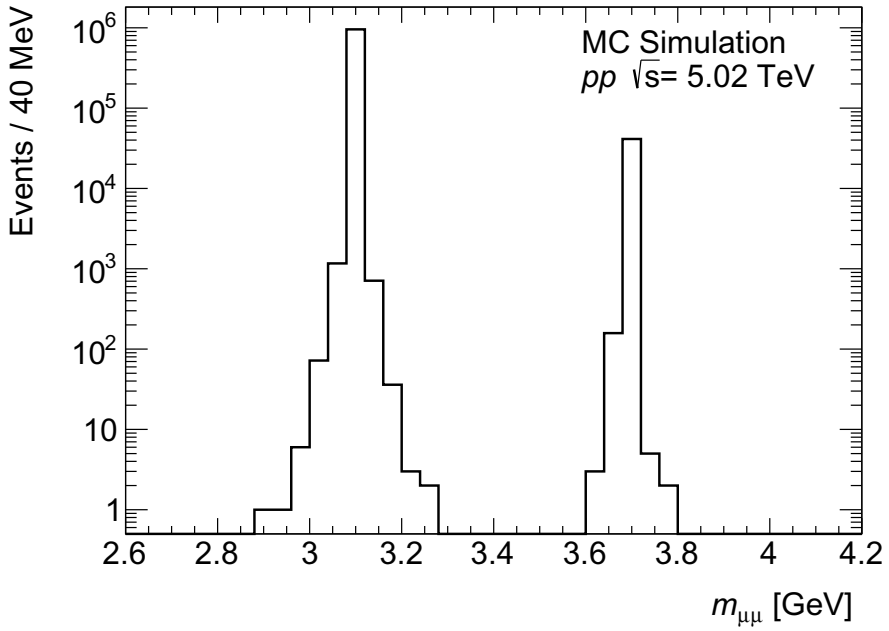

Figure 4.1: The histogram of invariant mass of muon pairs generated in PYTHIA.

Figures presented below are used to compare the kinematics of dimuon candidates and ψ(nS), where $n = 1$, 2 denotes radial quantum number, and S denotes states with $L = 0$. $\psi(1S)$ and $\psi(2S)$ denotes J/ψ, and $\psi(2S)$, respectively. Distributions of y, ϕ and p_{T} were calculated. Rapidity distribution is shown in Figure 4.2. Shape of the rapidity distribution is not Gaussian. The shape is driven by the transformation of the binary parton-level cross-section from (E, $\vec{p}$) where it increases at large longitudinal angles to (p_{T}, y, ϕ, m) where it decreases at large y for particles above a given p_{T} threshold. The distribution of azimuthal angle ϕ is presented in Figure 4.3. As expected, charmonium yield is a constant function of ϕ as unpolarized beams were used. The p_{T} spectra are shown in Figure 4.4. The peak located at $p_{\mathrm{T}} = 5\,\mathrm{GeV}$ is corresponding to setting of $\hat{p}_{\mathrm{T,min}} = 5\,\mathrm{GeV}$, where $\hat{p}_{\mathrm{T,min}}$ denotes the minimum p_{T} of parton coming from the hard-process. High-p_{T} region is well described by a QCD-inspired power-law function [43].

Distributions of y, ϕ and p_{T} are supposed to have the same shape for charmonia and dimuons. Small differences between distributions are due to statistical fluctuations.

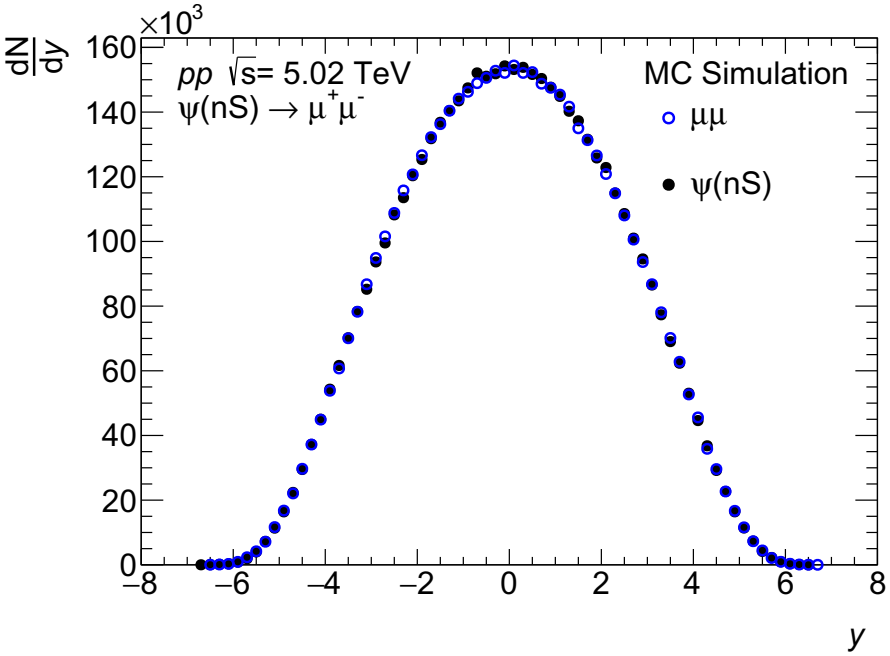

Figure 4.2: The rapidity distribution for charmonia states ψ(nS) (black markers) and for dimuons (blue circles) generated by PYTHIA.

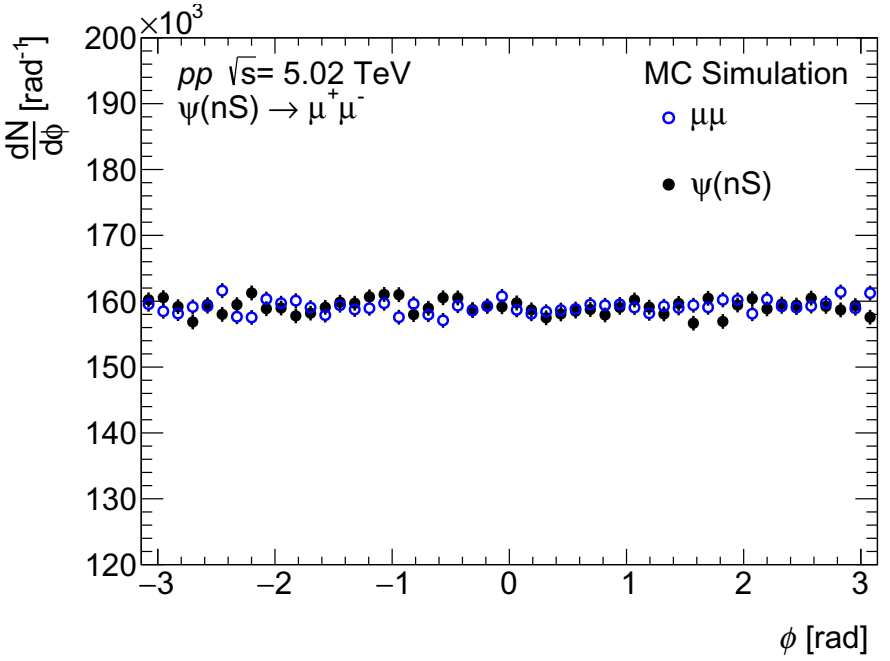

Figure 4.3: The azimuthal angle distribution for charmonia states ψ(nS) (black markers) and for dimuons (blue circles) generated by PYTHIA.

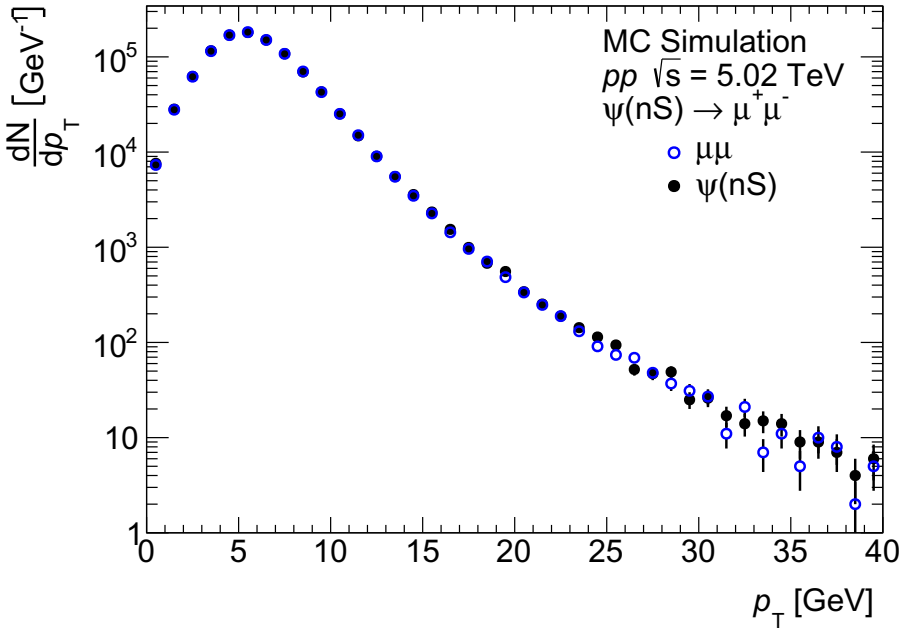

Figure 4.4: The transverse momentum distribution for charmonia states ψ(nS) (black markers) and for dimuons (blue circles) generated by PYTHIA.

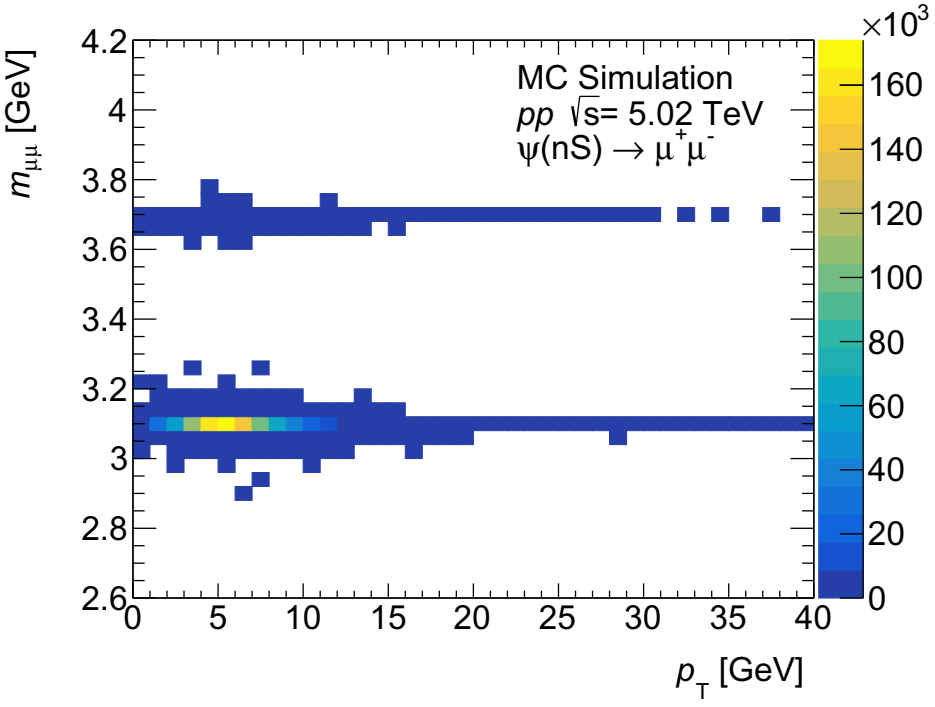

Figure 4.5: The 2D histogram representing the yield of the dimuon candidates as a function of transverse momentum and invariant mass generated by PYTHIA.

Histogram representing the yield of dimuon candidates as a function of transverse momentum p_{T} and invariant mass $m_{\mu\mu}$ is shown in Figure 4.5. Peak located at $p_{\mathrm{T}} = 5\,\mathrm{GeV}$ corresponds to the setting of the non-zero value of $\hat{p}_{\mathrm{T,min}}$.

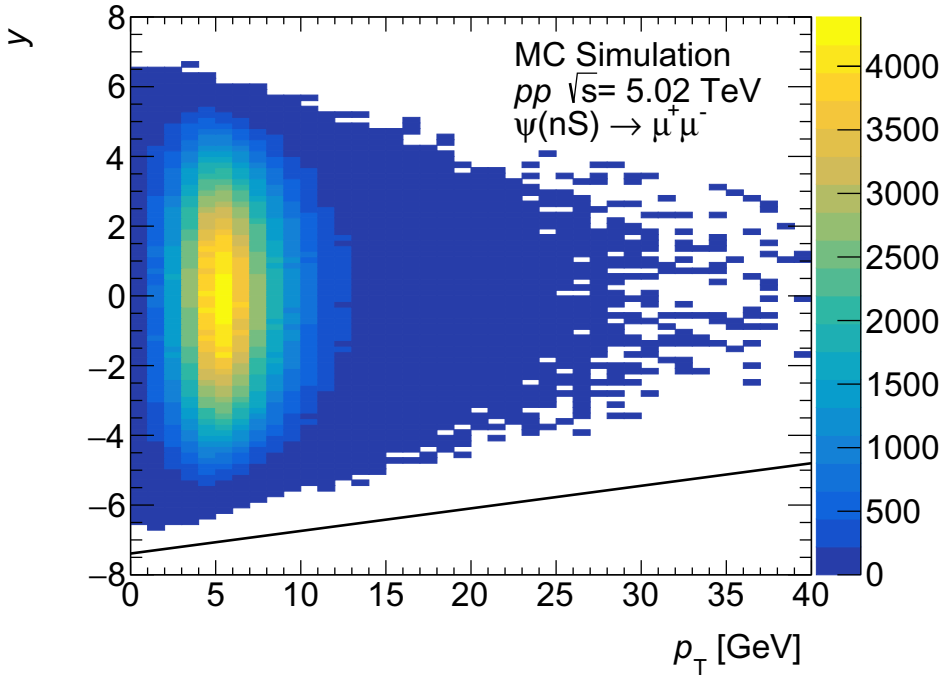

Figure 4.6: The 2D histogram representing the yield of the dimuon candidates as a function of transverse momentum and rapidity generated in PYTHIA. The black line corresponds to maximal rapidity driven by the total available energy in the process.

The 2D histogram, representing the yield of the dimuon candidates as a function of transverse momentum p_{T} and rapidity y, is shown in Figure 4.6. The reach of this distribution is driven by the available energy in the process. Most events are distributed near $p_{\mathrm{T}} = 5\,\mathrm{GeV}$, which is due to the setting of non-zero $\hat{p}_{\mathrm{T,min}}$ value. The maximum value of rapidity of process y_{max} corresponding to the available energy in the process $E_{max} = 2510\,\mathrm{GeV}$ was determined to be $|y_{max}| = 7.4$.

4.1.3 Gluon radiation of octet-states

Gluon radiation of charmonia octet-states produced in pp-collisions in PYTHIA was studied. Events with colour-octet intermediate states evolving to physical colour singlet either J/ψ or charmonia later decaying to J/ψ were chosen for this study. Studied particles were identified using particle identification codes (PID) described in PYTHIA manual.

Table 4.2 contains an overview of studied charmonia octet-states and a mean number of radiated gluons per one produced charmonium J/ψ, $\bar{N}_{gluons}$. It was studied with the MC sample of 100 000 events per subprocess. $\hat{p}_{\mathrm{T,min}}$ parameter was set to 8 GeV. Production of D-state charmonia was studied with the MC sample of 2 000 000 events per subprocess due to the small production rate of J/ψ. This lack of J/ψ produced by decaying D-states is caused by producing D-mesons.

The mean number of radiated gluons, $\bar{N}_{gluons}$, is a number of gluons that charmonium intermediate state radiates during evolution to physical J/ψ divided by the total number produced J/ψ of all subprocesses. Physical charmonium is not

always produced as J/ψ, but it could feed down to the J/ψ. No gluons are radiated during the feed down. Gluon radiation of the intermediate charmonia states was studied for every subprocess written in Table 4.1. Results are summarised in Table 4.2. In order to simplify obtained results, studied subprocesses were divided into eight categories. Each category has a different combination of the intermediate state and resulting physical charmonium. Intermediate singlet states with almost no radiation of gluons are seen as expected. Intermediate octet states with radiation of 2 gluons per produced J/ψ are mostly observed. Notation $c\bar{c}(8) \rightarrow J/\psi$ means selection of events, where octet-state evolves into physical charmonium resulting into J/ψ. If there is no additional information about the subprocess selection, all subprocesses containing the intermediate colour octet states, written in Table 4.1, are used. Errors were estimated as $\sigma/\sqrt{N}$, where σ denotes the standard deviation and N denotes the number of events.

Table 4.2: Gluon radiation of various charmonium intermediate states during evolution to physical J/ψ. X denotes a photon γ, hadron, or nothing, depending on the type of transition from physical charmonium to the J/ψ.

No.	Channel:	$\bar{N}_{gluons}$
1	$[3S1(1)] \rightarrow 3S1 \rightarrow J/\psi + X$	0.0014 ± 0.0002
2	$[3S1(8)] \rightarrow 3S1 + g \rightarrow J/\psi + X$	1.936 ± 0.002
3	$[1S0(8)] \rightarrow 3S1 + g \rightarrow J/\psi + X$	1.845 ± 0.002
4	$[3PJ(8)] \rightarrow 3S1 + g \rightarrow J/\psi + X$	1.874 ± 0.002
5	$[3DJ(1)] \rightarrow 3DJ \rightarrow J/\psi + X$	0.022 ± 0.012
6	$[3PJ(8)] \rightarrow 3DJ + g \rightarrow J/\psi + X$	1.775 ± 0.006
7	$[3PJ(1)] \rightarrow 3PJ \rightarrow J/\psi + X$	0.0014 ± 0.0002
8	$[3S1(8)] \rightarrow 3PJ + g \rightarrow J/\psi + X$	1.868 ± 0.002

Histogram representing the yield of J/ψ as a function of the energy of J/ψ, $E^{\mathrm{J}/\psi}$, and energy of its intermediate state, $E^{c\bar{c}}$, is presented in Figure 4.7. As expected, most cases are located above diagonal, which denotes the equality between the energy of intermediate state and the energy of J/ψ. Two possible sources of the presence of the events located below the diagonal can be effects of colour-reconnection and the initial state radiation.

Figure 4.8 shows the histogram representing the yield of J/ψ as a function of its transverse momentum, $p_{\mathrm{T}}^{\mathrm{J}/\psi}$, and a transverse momentum of intermediate state $p_{\mathrm{T}}^{c\bar{c}}$. As expected, yield is mostly located above the diagonal since the intermediate state is expected to lose energy during its evolution. However, some cases, where J/ψ has higher $p_{\mathrm{T}}^{\mathrm{J}/\psi}$ that intermediate state $c\bar{c}$, are observed. In these cases, the transverse momentum of physical charmonium is increased by the recoil caused by the emission of particles.

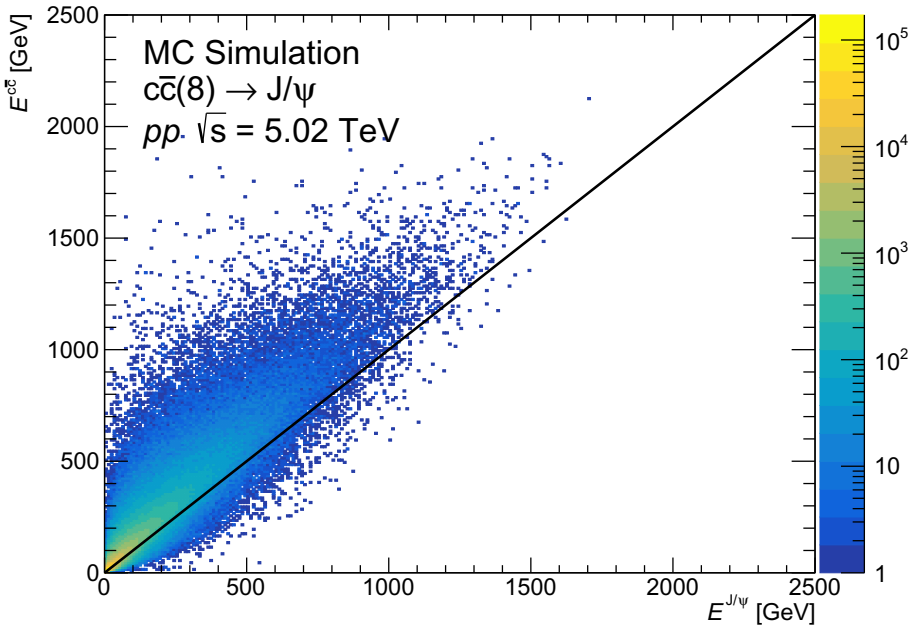

Figure 4.7: The 2D histogram representing the yield of J/ψ as a function of the energy of J/ψ ,$E^{\mathrm{J}/\psi}$, and energy of its intermediate state ,$E^{c\bar{c}}$, produced in pp-collisions at $\sqrt{s} = 5.02$ TeV in PYTHIA. The black line is corresponding to events with $E^{\mathrm{J}/\psi} = E^{c\bar{c}}$.

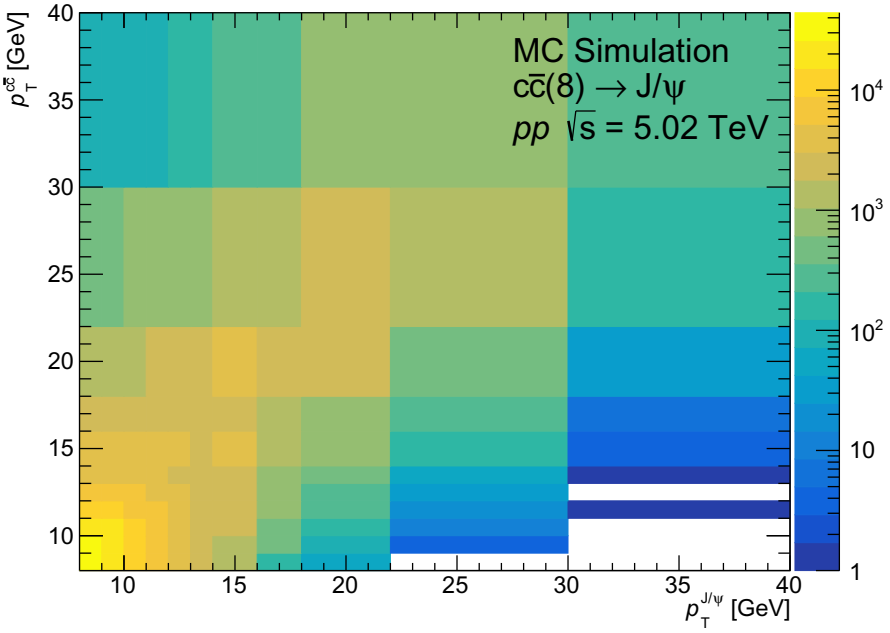

Figure 4.8: The 2D histogram representing the yield of J/ψ as a function of transverse momentum of J/ψ ,$p_{\mathrm{T}}^{\mathrm{J}/\psi}$, and transverse momentum of its intermediate state, $p_{\mathrm{T}}^{c\bar{c}}$, produced in pp-collisions at $\sqrt{s} = 5.02$ TeV in PYTHIA.

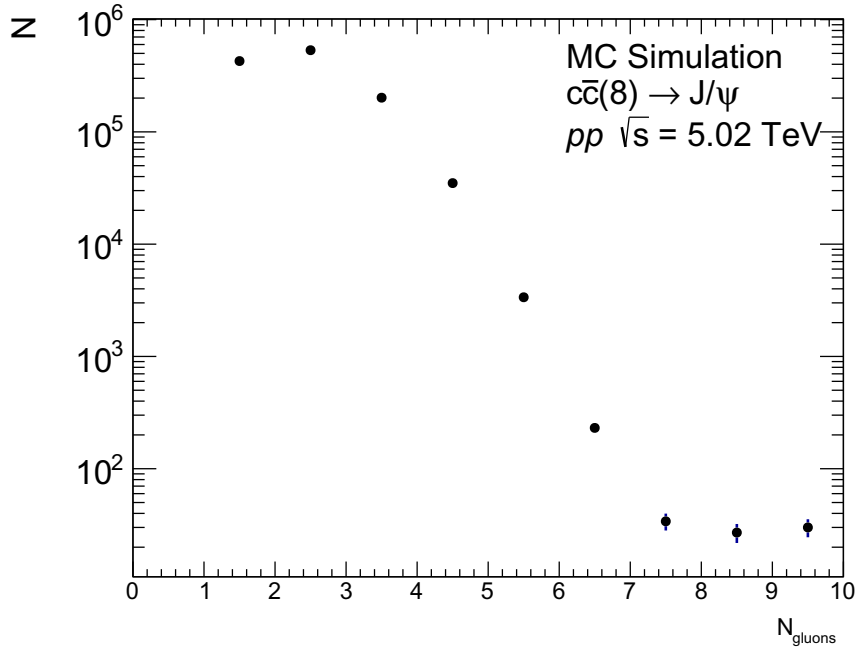

Figure 4.9: The yield of J/ψ as a function of the number of radiated gluons, N_{gluons}, which were radiated during the evolution from its original intermediate state $c\bar{c}(8)$. First bin represents zero radiated gluons.

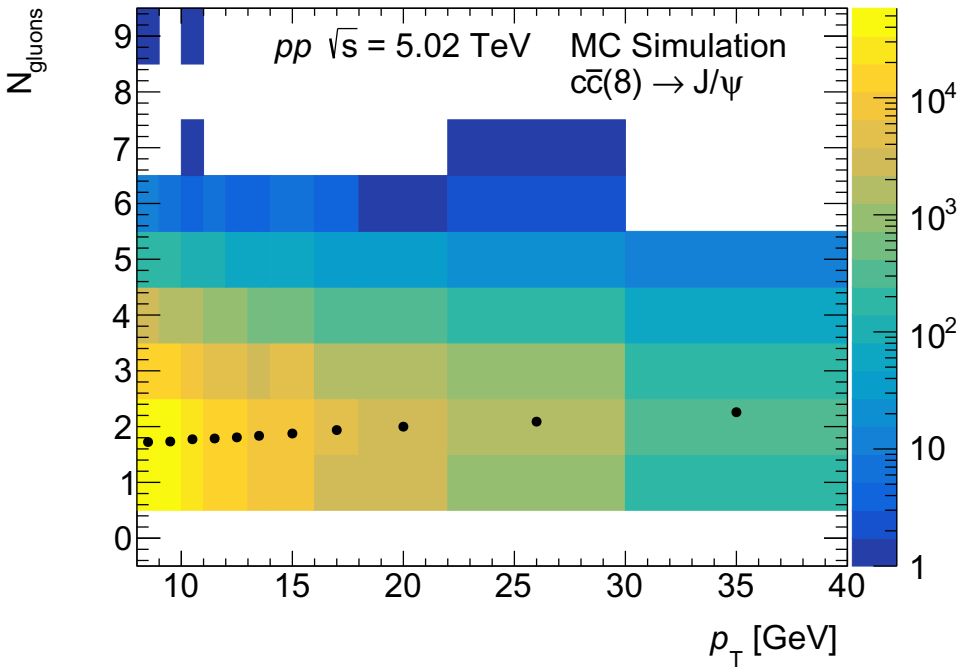

Figure 4.10: The yield of J/ψ as a function of transverse momentum and the number of radiated gluons during the evolution of the original intermediate state $c\bar{c}(8)$ generated in PYTHIA. Black markers denote the mean value of radiated gluons in a given p_{T} bin.

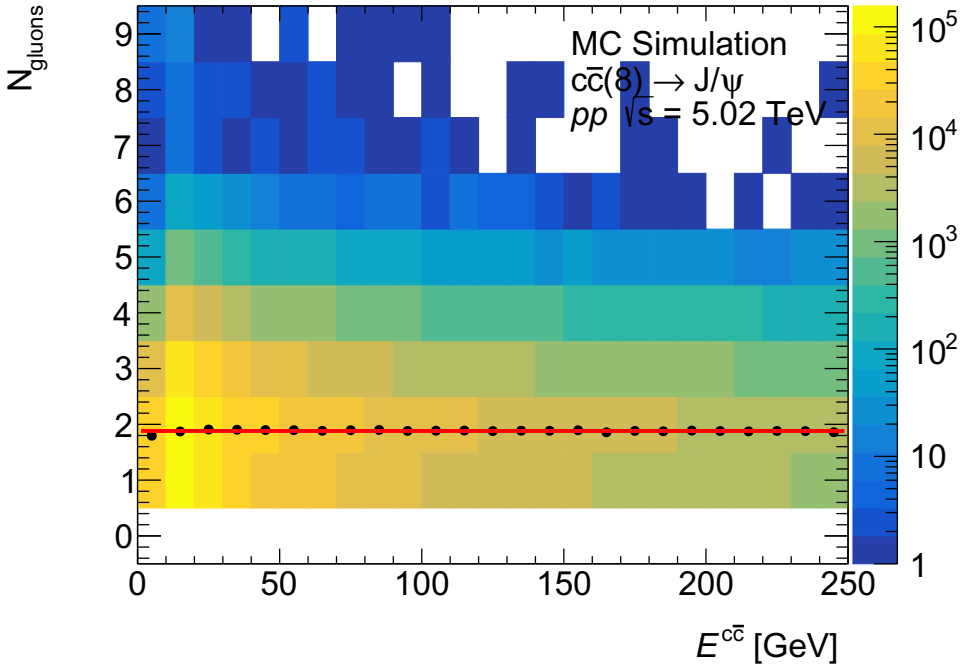

Figure 4.11: The yield of J/ψ as a function of energy of the intermediate octet state, $E^{c\bar{c}}$, and the number of radiated gluons during the evolution of the original intermediate state $c\bar{c}(8)$ generated in PYTHIA. Black markers denote the mean value of radiated gluons in a given $E^{c\bar{c}}$ bin. Red line denotes result of fitted constant function.

Histogram representing the yield of J/ψ as a function of the number of radiated gluons, N_{gluons} from its original intermediate state is shown in Figure 4.9. This histogram contains all subprocesses, including intermediate octet states written in Table 4.1. It is seen that the evolution of the intermediate octet state into the physical charmonium is mostly accompanied by the emission of 1-3 gluons.

Further, histogram representing the yield of J/ψ as a function of its transverse momentum p_{T} and the number of radiated gluons from the intermediate color octet state is shown in Figure 4.10. Again, this histogram contains all subprocesses from Table 4.1. Shape of distribution along the y-axis corresponds to results shown in Figure 4.9. Black markers denote the mean value of radiated gluons per one p_{T} bin. It can be seen that the mean value of radiated gluons modestly increases with increasing p_{T} of final J/ψ. In general, the mean value is consistent with values provided in Table 4.2.

Histogram representing the yield of J/ψ as a function of energy of the intermediate octet state, $E^{c\bar{c}}$, and the number of radiated gluons during the evolution of the original intermediate state $c\bar{c}(8)$ is shown in Figure 4.11. Black markers denote the mean value of radiated gluons in a given $E^{c\bar{c}}$ bin. This distribution is fitted with a constant function. It is seen that the mean value of radiated gluons during the evolution of the original intermediate state does not depend on the energy of intermediate state.

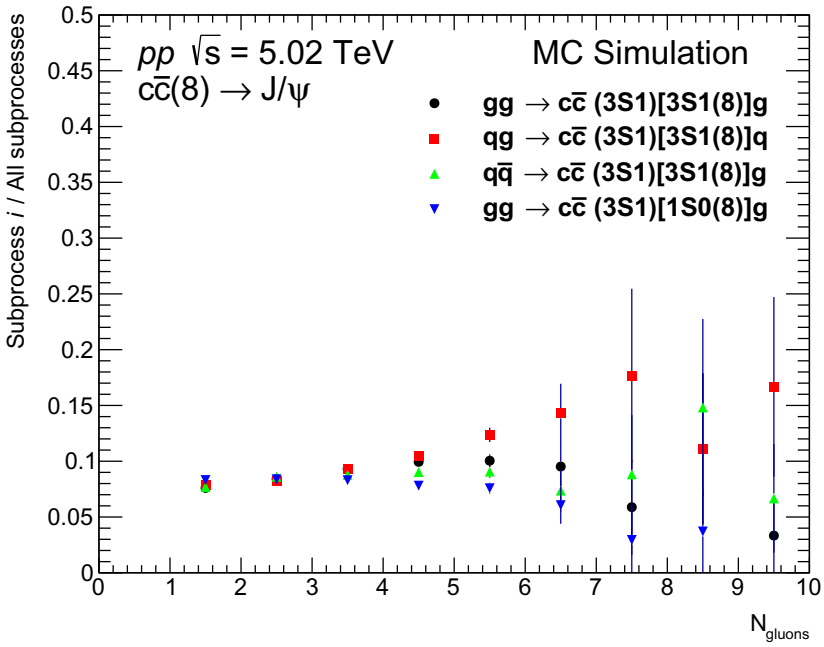

Figure 4.12: Distributions of J/ψ yields for a given subprocess (see legend) divided by total J/ψ yield for all subprocesses evaluated as a function of number of radiated gluons. First bin represents zero radiated gluons.

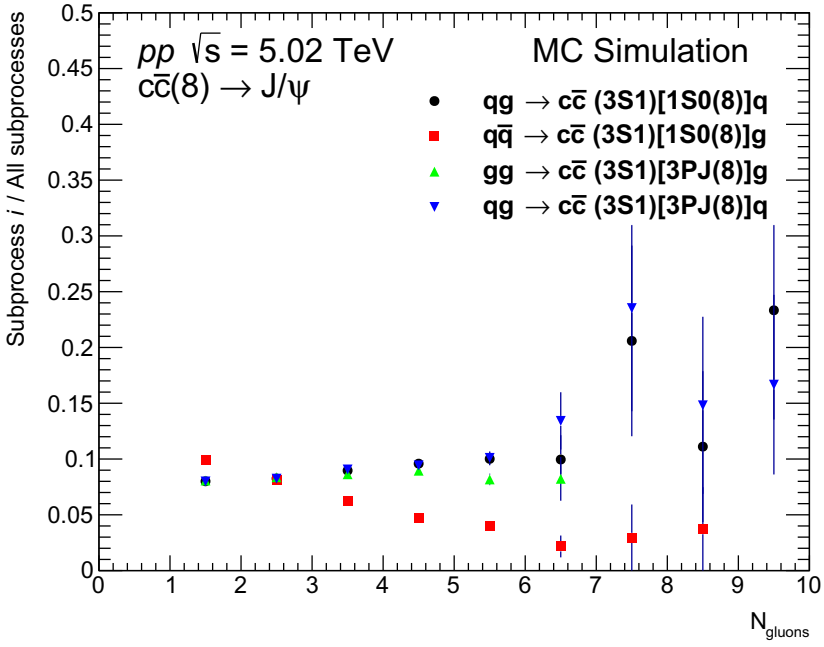

Figure 4.13: Distributions of J/ψ yields for a given subprocess (see legend) divided by total J/ψ yield for all subprocesses evaluated as a function of number of radiated gluons. First bin represents zero radiated gluons.

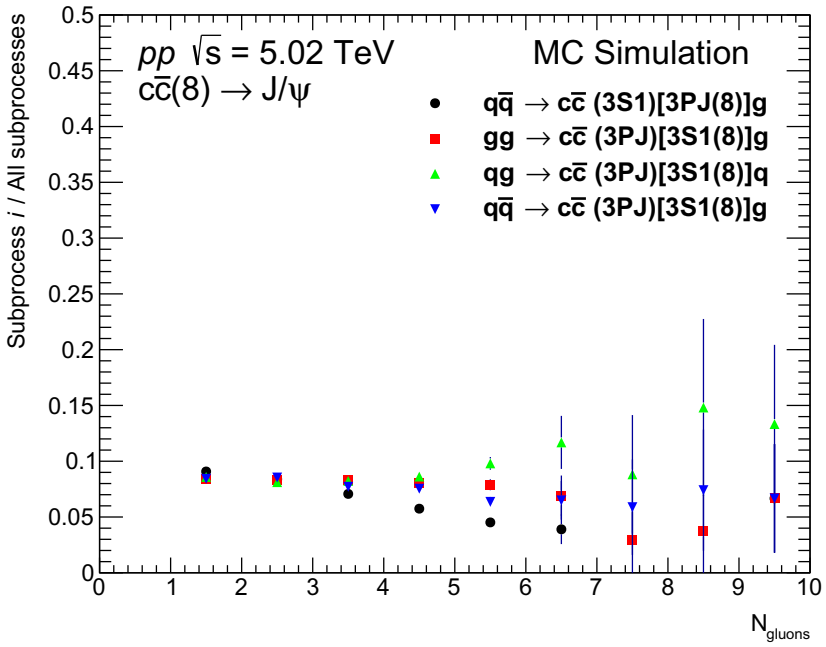

Figure 4.14: Distributions of J/ψ yields for a given subprocess (see legend) divided by total J/ψ yield for all subprocesses evaluated as a function of number of radiated gluons. First bin represents zero radiated gluons.

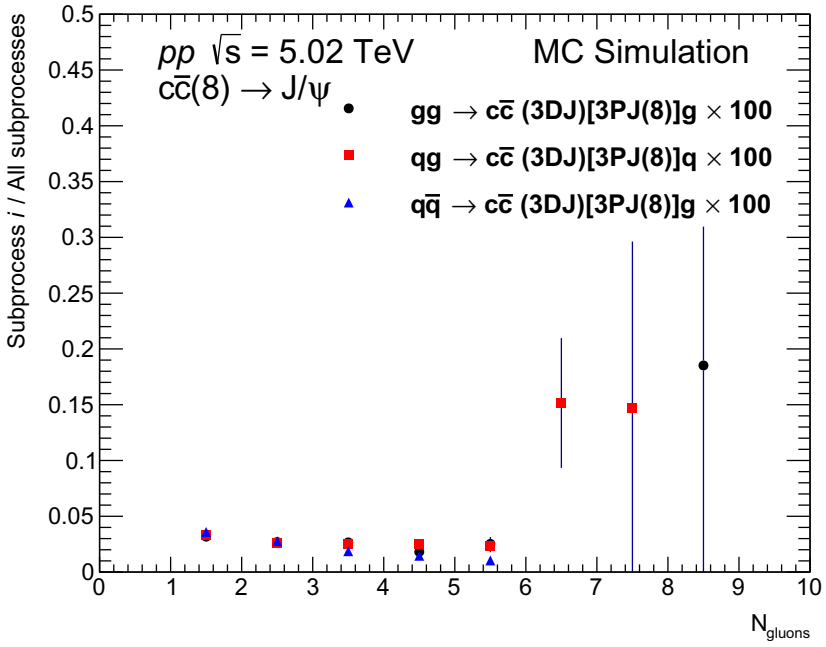

Figure 4.15: Distributions of J/ψ yields for a given subprocess (see legend) divided by total J/ψ yield for all subprocesses evaluated as a function of number of radiated gluons. First bin represents zero radiated gluons. Distributions are scaled by factor of 100 due to insufficient statistics.

In order to study gluon radiation of intermediate state produced in various subprocesses, distributions of J/ψ yield for a given subprocess divided by J/ψ yield for all subprocesses (Figure 4.9) are calculated. These ratios evaluated as a function number of radiated gluons are shown in Figures 4.12 - 4.15 for all subprocesses defined in Table 4.1. It is observed that all subprocesses start to differ at the value of three emitted gluons. The origin of these small differences is not known. Different statistics of processes in Figure 4.15 are caused by the production of D-mesons as explained earlier. Histogram shown in Figure 4.15 is scaled by a factor of 100 due to insufficient statistics.

Transverse momentum spectra of resulting J/ψ are presented in Figures 4.16, 4.17, 4.18 and 4.19. As expected, there are no large deviations among different subprocesses. A similar shape for similar subprocesses is observed, e.g. subprocesses with [3S1(8)] in Figure 4.16. On the contrary different subprocesses exhibit different shapes, e.g. subprocesses involving [1S0(8)] differ from subprocesses with [3S1(8)] by a factor of 10 - see Figure 4.16.

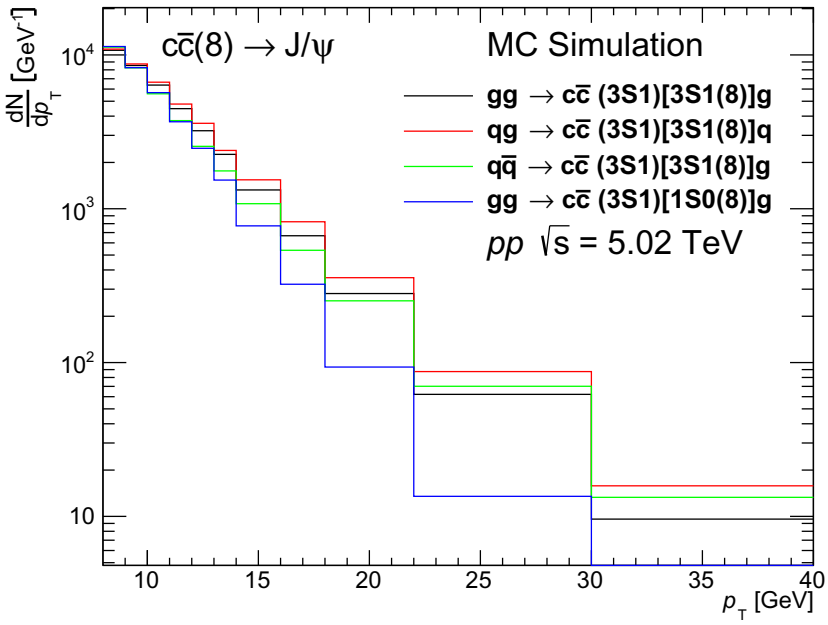

Figure 4.16: The transverse momentum spectra of physical charmonia J/ψ produced in subprocess i (see legend).

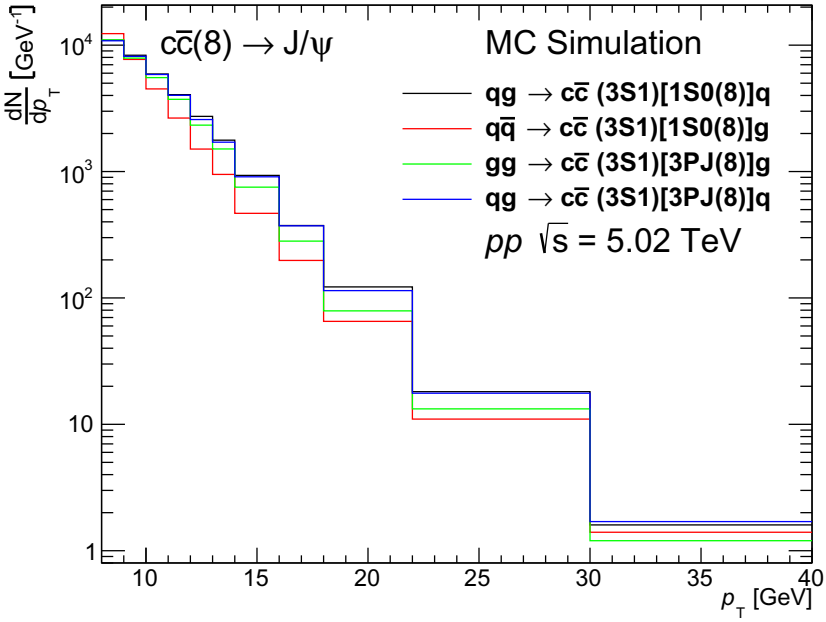

Figure 4.17: The transverse momentum spectra of physical charmonia J/ψ produced in subprocess i (see legend).

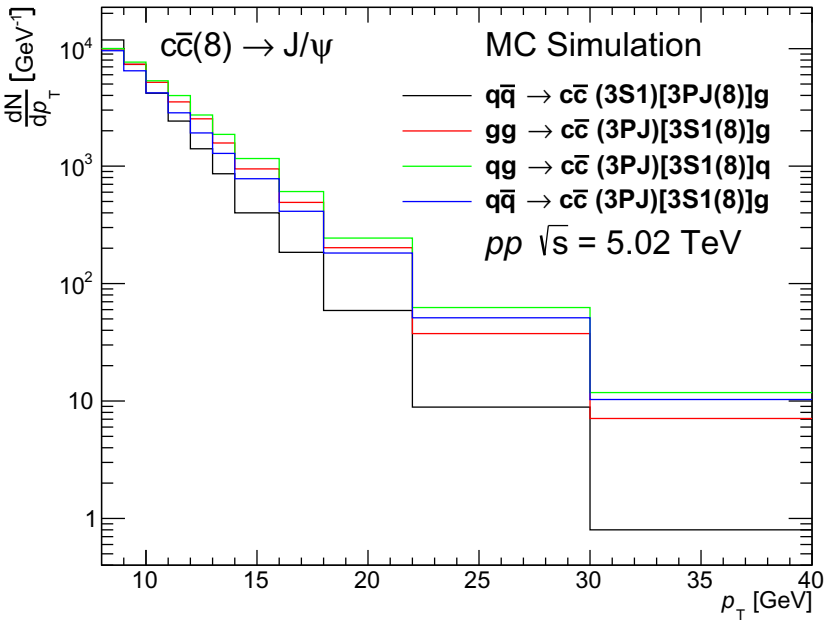

Figure 4.18: The transverse momentum spectra of physical charmonia J/ψ produced in subprocess i (see legend).

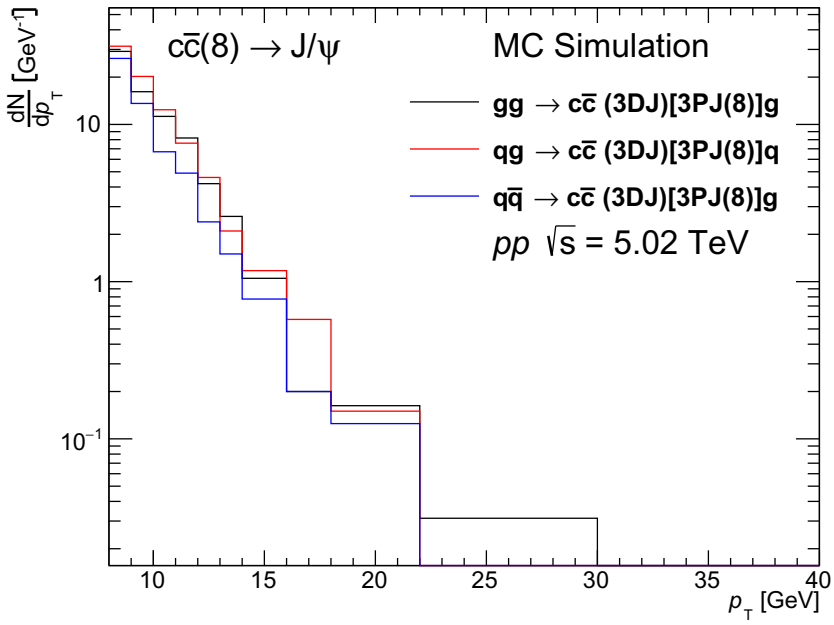

Figure 4.19: The transverse momentum spectra of physical charmonia J/ψ produced in subprocess i (see legend).

4.2 Data analysis

Analysis described in this section follows analysis published in Ref. [2] and ATLAS supporting document [44].

4.2.1 Event selection

The analysis presented in this thesis uses data from pp collisions at the center-of-mass energy of $\sqrt{s} = 5.02\,\text{TeV}$ recorded by the ATLAS Experiment in 2017. Events were collected using a trigger, which requires that the event contains at least two reconstructed muons. Both muons must generate a L1 muon trigger and they have to be confirmed by the HLT.

Muon candidates are required to pass the "tight" muon working point selection [45] without any TRT requirements. Further, these muon candidates have to have $p_{\text{T}} > 4\,\text{GeV}$ and $|\eta| < 2.4$. To be selected, muon pair must have origin in a common vertex, have opposite charge, and an invariant mass in the range of $2.6 < m_{\mu\mu} < 4.2\,\text{GeV}$. In this study acceptance correction is applied (it is described in section 4.2.3), but no efficiency correction is applied.

Kinematics of selected dimuons is shown in Figure 4.20.

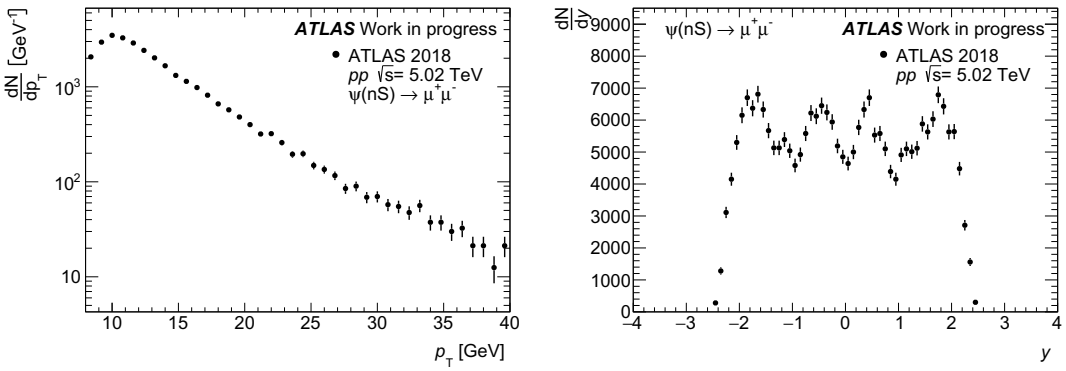

Figure 4.20: The transverse momentum distribution of dimuon candidates (left panel) and the rapidity distribution of dimuon candidates (right panel). Dimuon candidates were not corrected for detector efficiency and acceptance.

The p_{T} spectrum of dimuon candidates, shown in the left panel of the Figure 4.20, has expected shape described by power law dictated by perturbative QCD. The rapidity distribution, shown in the right panel of the Figure 4.20, is different compared to the distribution extracted from Pythia in the Figure 4.2. It differs due to the detector range and its efficiency. The ID covers the range of $|\eta| < 2.5$.

4.2.2 Efficiency correction

In the data analysis it is necessary to apply efficiency correction to remove negative effects of trigger and reconstruction algorithms. In the study published in 2018 [2], trigger and reconstruction efficiencies were calculated using tag-and-probe method (T&P) [45].

The T&P method is based on the selection of a muon sample from $J/\psi \to \mu\mu$ events collected by a single muon trigger which requires one muon of the

decay (tag) to be identified as "tight" muon which triggered the read-out of the event and the second muon (probe) which is required to be reconstructed as system independent. The background contamination and the muon efficiency are obtained from a simultaneous ML fit of two independent distributions of the invariant mass which differ by events in which the probe is or is not successfully matched to the selected muon. Muon reconstruction efficiency varies between 60% and 90%. Dimuon trigger efficiency increases from 50% to 85% with increasing p_{T}.

4.2.3 Acceptance correction

The *acceptance* $\mathcal{A}$ of quarkonium decays into muon pairs is defined as probability that both muons from the decay fall in the fiducial region ($p_T(\mu^{\pm}) > 4$ GeV, $|\eta(\mu^{\pm})| < 2.4$). The acceptance depends on transverse momentum, rapidity, invariant mass and the spin-alignment of the quarkonium state, but previous measurements suggest that decays of quarkonia produced at LHC energies are consistent with the assumption that they are unpolarised.

Figure 4.21 shows the two-dimensional acceptance maps of $J/\psi \to \mu^+\mu^-$ and $\psi(2\mathrm{S}) \to \mu^+\mu^-$ as a function of the p_T and $|y|$. These maps are generated by using a toy MC sample as in previous measurements (for more details see [46]).

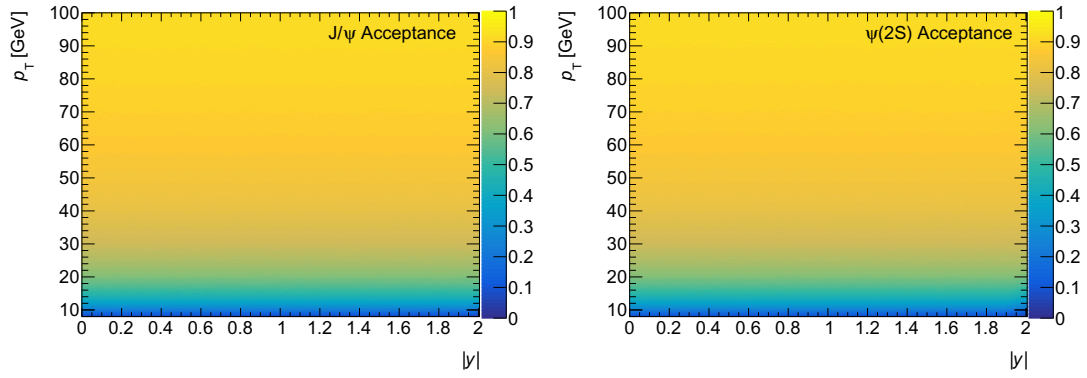

Figure 4.21: The unpolarized 2D acceptance map for $J/\psi \to \mu^+\mu^-$ (left panel) and $\psi(2\mathrm{S}) \to \mu^+\mu^-$ (right panel).

The acceptance correction is applied to charmonium yields using linear interpolation which is provided as follows: The upper mass boundary for the J/ψ candidates is assumed to be 3.5 GeV and the lower mass boundary for $\psi(2\mathrm{S})$ candidates is assumed to be 3.2 GeV resulting in a full range of 0.3 GeV. In the interpolation range of $m_{\mu\mu} \in [3.2,\ 3.5]$ following interpolation function is applied:

$$\mathcal{A} = \mathcal{A}(J/\psi) \times \frac{3.5 - m_{\mu\mu}}{0.3} + \mathcal{A}(\psi(2\mathrm{S}))\frac{m_{\mu\mu} - 3.2}{0.3}. \tag{4.1}$$

4.3 Fitting procedure

This section describes essential elements for yield extraction from the measured data obtained by the particle detector. Yield extraction is provided via a specific fit model using *RooFit* library [47] which is a part of *ROOT* toolkit [48] for data

analysis. In following paragraphs there is basic information about fit models, and RooFit is introduced and a primary example explaining the functionality of RooFit is provided. In section 4.4, fit model used in this analysis is described, and results of fitting are presented.

RooFit provides fitting of measured data via modelling of event data distributions. Measured data of any phenomena always contain both signal and background. Successful data analysis reports only signal events from measured data. This is done via building a fit model describing the signal and background line shapes, which calculates a number of signal events and a number of background events by fitting the measured data.

RooFit is like other programs (HistFitter [49] and so on) using *probability density functions (PDFs)* that describe the probability density of the observable $\vec{x}$ in terms of function of the parameters $\vec{\alpha}$, PDF$(\vec{x};\vec{\alpha})$. The fit model is the composite PDF describing our measured data line shape. This PDF has to be composed of two components: signal PDF and background PDF.

Working with PDFs is problematic because of the normalisation (sometimes hard to calculate) and integrating the PDF in higher dimensions. RooFit computes normalisation automatically (PDF has to be always normalised to 1) and simplifies the computation of the integrals. Therefore, fraction of the PDF can be used to compute the number of events.

RooFit is constructing data models using C++ objects, and each mathematical object is represented by a C++ object. Table 4.3 shows the correspondence between basic mathematical objects and RooFit classes.

Table 4.3: Relation between basic mathematical objects and RooFit classes [47].

Object	Math symbol	RooFit class name
Variable	x, α	RooAbsVar
Space point	$\vec{x}$	RooArgSet
List of space points	$\vec{x}_i$	RooAbsData
Function	$f(\vec{x})$	RooAbsReal
PDF	$A(\vec{x};\vec{\alpha})$	RooAbsPdf
PDF addition	$C(x) = fA(x) + (1-f)B(x)$	RooAddPdf

For instance, in the Listing 4.2 the construction of the Gaussian PDF in RooFit is shown. A Gaussian PDF in RooFit typically consists of four objects: three objects represent the observable, the mean and the sigma, the fourth object represents a Gaussian PDF.

Listing 4.2: Construction of the Gaussian PDF in RooFit

```
1 // RooFit observable with bounds
2 RooRealVar mass("mass", "m [GeV]", 2.8, 3.3);
3
4 // Parameters with initial value and bounds
5 RooRealVar mean("mean", "mean", 3.096, 2.8, 3.3);
6 RooRealVar sigma("sigma", "sigma",0.035, 0.02, 0.1);
7
8 // Build a Gaussian PDF
```

```
9 RooGaussian signal("signal", "signal", mass, mean, sigma);
```

The main reason for using Roofit framework is yield extraction from measured data. This task is not simple, but in RooFit, one can extract the desired yield using *Extended Maximum Likelihood method*. This method provides an extension of the likelihood function by normalisation. Therefore, one can directly identify some coefficients as the number of events of the specific process. Yield extraction can be also done by using of the Maximum Likelihood (ML) method. However, it differs from Extended ML fit in a way how we identify used parameters for summing signal PDF and background PDF - the parameter f from Table 4.3 serves as *fraction* of a certain component or it serves as a *yield* of a certain component.

Listing 4.3 shows an example of using Extended ML fitting in RooFit to provide yield extraction in two component model. Line 20 defines the observable of interest, which is *invariant mass*. In this example a simple Gaussian PDF is used as the signal shape. This Gaussian has mean at 3.069 GeV. Its sigma was chosen to be 0.025 GeV. Lines 27-28 provides building of Gaussian PDF with parameters *mean* and *sigma*.

Lines 30-35 define background which is build using exponential PDF. Lines 37-44 build a complete model, where Gaussian PDF and Exponential PDF are summed together. Parameters *nsig* and *nbkg* defined in lines 38-39 are used for yield extraction.

Line 49 generates 5000 events using Toy MC generator implemented in RooFit. Further, line 53 provides fitting using Extended ML fit.

Lines 55-70 are used to plot data, results of the fit and the components of our model. Further, lines 72-79 are used to build a legend. The rest of the Listing 4.3 provides printing the extracted number of signal and background events. The result of the fit is shown in Figure 4.22.

Listing 4.3: Construction of the Gaussian PDF in RooFit

```
1 // Unbinned fitting using fit model built in RooFit
2 // Run with ROOT as:
3 // .L roofit_ex.cpp
4 // roofit_ex()
5 // Possible errors: Check version of ROOT, works well
6 // with ROOT 6.24
7
8 #include "RooRealVar.h"
9 #include "RooDataSet.h"
10 #include "RooGaussian.h"
11 #include "RooAddPdf.h"
12 #include "RooPlot.h"
13
14 using namespace std;
15 using namespace RooFit;
16
17 void roofit_ex(){
18 ////////////-Signal-/////////////////////////////////////
19 // Define observables:
```

```
20    RooRealVar mass("mass", "m [GeV]", 2.8, 3.6);
21
22 // Define parameters:
23    RooRealVar sigma("mean", "", 3.096);
24    RooRealVar width("sigma", "", 0.025);
25
26 // Build Gaussian PDF:
27    RooGaussian signal("signal", "signal PDF", mass,
28    mean, sigma);
29
30 ////////////-Background-////////////////////////////////
31 // Build Exponential background PDF:
32    RooRealVar bkgPar("bkgpar", "background parameter",
33    -2.0);
34    RooExponential background("background", "Exponential PDF",
35     mass, bkgPar);
36
37 ////////////-Build a complete model-////////////////////
38    RooRealVar nsig("nsig", "Number of signal events",
39    0.0, 10000.0);
40    RooRealVar nbkg("nbkg", "Fraction of bkg events",
41    0.0, 10000.0);
42    RooAddPdf model("model", "Gauss + Exp",
43    RooArgList(signal, background),
44    RooArgList(nsig, nbkg));
45
46 ///////////-Data analysis-////////////////////////////////
47 // Generate ToyMC data using our model, then fit these
48 // data using ML method
49    RooDataSet *data = model.generate(mass, 5000);
50
51 // Perform Extended ML fit
52 // of composite model to data:
53    model.fitTo(*data, Extended());
54
55 // Plot generated data
56    RooPlot *results = mass.frame(Title("ML fit of
57     composite model"), Bins(40));
58    data->plotOn(results, Invisible()); // Make components
59 // invisible...We want to plot them separately
60    model.plotOn(results, Invisible());
61    model.plotOn(results, Name("Signal"),
62     Components(RooArgSet(background,signal)), FillColor(kBlue),
63     DrawOption("F"), FillStyle(3344));
64    model.plotOn(results, Name("Background"),
65    Components(background), LineColor(kWhite),
66    FillColor(kGray), DrawOption("F"));
67    data->plotOn(results, Name("Data"), MarkerSize(1.0));
```

```
68      model.plotOn(results, Name("Fit"),
69      LineColor(kBlack), LineWidth(3));
70      results->Draw();
71
72  // Build legend
73      TLegend *leg = new TLegend(0.65,0.65,0.89,0.89);
74      leg->SetLineColor(kWhite);
75      leg->AddEntry("Data","Data", "P");
76      leg->AddEntry("Signal","Signal","F");
77      leg->AddEntry("Background","Background", "F");
78      leg->AddEntry("Fit","Fit", "L");
79      leg->Draw();
80
81  // Print extracted yields
82      cout << "Number of signal events:" << nsig.getVal()
83     << endl;
84      cout << "Number of background events:" << nbkg.getVal()
85     << endl;
86
87  }
```

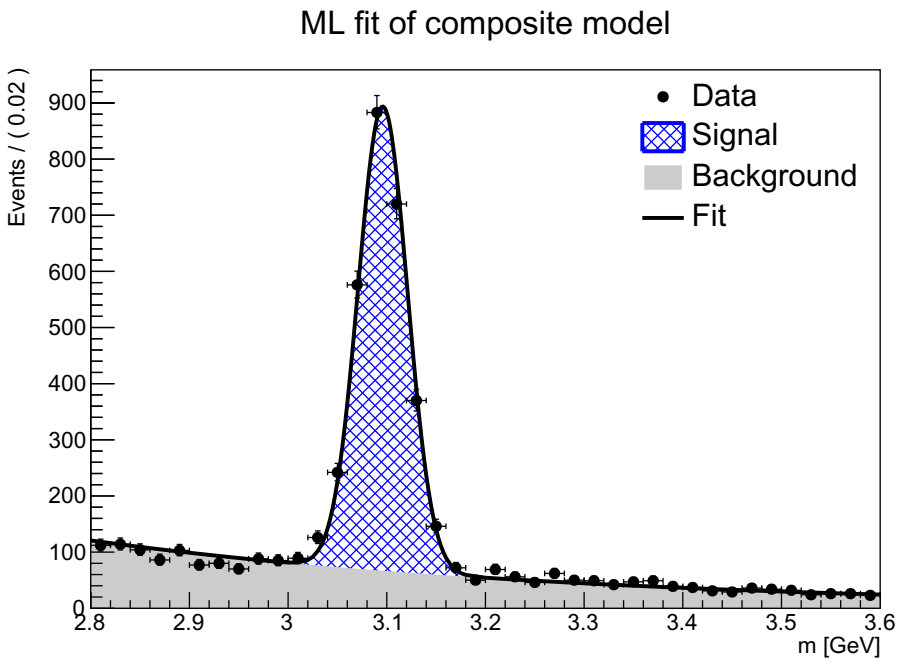

Figure 4.22: Extended ML fit using Roofit. 5000 events were generated using Toy MC generator implemented in RooFit.

Macro presented in the listing 4.3 returned after fitting 5000 generated events these results:

$$nsig = 2591$$

$$nbkg = 2709$$

4.4 Yield extraction

The goal of this study it to obtain results that can be compared with study [2]. First, the main steps from study [2] are summarised. Then, analysis of a fraction of 2017 data set is performed and results are compared with the results from study [2].

First, the differential cross section of charmonium is defined. In this study, differential cross section (multiplied by the dimuon decay branching ratio) is calculated for each interval of transverse momentum and rapidity as follows:

$$\frac{\mathrm{d}^2\sigma_{\mathcal{O}(\mathrm{nS})}}{\mathrm{d}p_\mathrm{T}\mathrm{d}y} \times B(\mathcal{O}(\mathrm{nS}) \to \mu^+\mu^-) = \frac{N_{\mathcal{O}(\mathrm{nS})}}{\Delta p_\mathrm{T} \times \Delta y \times L}, \tag{4.2}$$

where L is the integrated luminosity, Δp_T and Δy are interval sizes of dimuon transverse momentum and rapidity, respectively. $N_{\mathcal{O}(\mathrm{nS})}$ is the observed yield of charmonium of nS state, where n = 1, 2 is the radial quantum number, and S is the spectroscopic notation of state with zero orbital angular momentum. This yield is extracted from the fit and corrected using total correction weight w_{total}^{-1}, which is assigned to each selected dimuon candidate. This weight is defined as:

$$w_{total}^{-1} = \mathcal{A}(\mathcal{O}(\mathrm{nS})) \cdot \varepsilon_{reco} \cdot \varepsilon_{trigger}, \tag{4.3}$$

where $\mathcal{A}(\mathcal{O}(\mathrm{nS}))$ is the acceptance of the selected dimuon for a given charmonium state, ε_{reco} is the dimuon reconstruction efficiency and $\varepsilon_{trigger}$ is the trigger efficiency.

It is necessary to distinguish between the prompt charmonia (charmonia produced in hard processes including decays or feed-down of other charmonium states) and non-prompt charmonia (charmonia produced via b-hadron decays). To distinguish these, the pseudo-proper lifetime $\tau_{\mu\mu}$ is used. It is defined as:

$$\tau_{\mu\mu} = \frac{L_{xy} m_{\mu\mu}}{p_\mathrm{T}^{\mu\mu}}, \tag{4.4}$$

where $m_{\mu\mu}$ is dimuon invariant mass, $p_\mathrm{T}^{\mu\mu}$ is the dimuon transverse momentum and L_{xy} stands for the distance of the dimuon secondary vertex from the primary vertex along the dimuon momentum direction in the transverse plane.

To extract yields of the prompt and non-prompt charmonia from measured data the two-dimensional unbinned ML fit is performed on the weighted distributions of the dimuon invariant mass $m_{\mu\mu}$ and the pseudo-proper time $\tau_{\mu\mu}$ using the fit model described below. Each interval of dimuon transverse momentum $p_\mathrm{T}^{\mu\mu}$ and rapidity y is fitted independently in RooFit framework. The two-dimensional PDF for observables ($m_{\mu\mu}$, $\tau_{\mu\mu}$) is in the fit model defined as:

$$\mathrm{PDF}(m_{\mu\mu},\, \tau_{\mu\mu}) = \sum_{i=1}^{7} \beta_i f_i(m_{\mu\mu}) \cdot h_i(\tau_{\mu\mu}) \otimes g(\tau_{\mu\mu}), \tag{4.5}$$

where $\otimes$ denotes convolution of different PDFs, β_i is the normalisation factor of each component, $g(\tau_{\mu\mu})$ is a double Gaussian pseudo-proper time $\tau_{\mu\mu}$ resolution function (this function provides "smearing" of real values due to the resolution of the detector), $f_i(m_{\mu\mu})$ and $h_i(\tau_{\mu\mu})$ represent PDF terms of charmonia signal and background contributions, respectively. Definitions of $f_i(m_{\mu\mu})$ and $h_i(\tau_{\mu\mu})$ PDF terms are summarised in Table 4.4.

One can find out that according to Equation 4.5 used fit model PDF has seven terms. As it is described in Table 4.4 the charmonium signal line shape in $m_{\mu\mu}$ is described by the sum of a Crystall Ball (CB) function (parameters for this fuction are taken from study [50]) and a single Gaussian function with the same mean. The CB function is defined as

$$CB\left(m;\mu,\sigma,\alpha,n\right) = N \cdot \begin{cases} \exp\left(-\frac{(m-\mu)^2}{2\sigma^2}\right), \text{ for } \frac{m-\mu}{\sigma} > -\alpha \\ A \cdot \left(B - \frac{m-\mu}{\sigma}\right)^{-n}, \text{ for } \frac{m-\mu}{\sigma} \leq -\alpha \end{cases} \tag{4.6}$$

where

$$A = \left(\frac{n}{|\alpha|}\right)^n \cdot \exp\left(-\frac{|\alpha|}{2}\right) \tag{4.7}$$

$$B = \frac{n}{|\alpha|} - |\alpha| \tag{4.8}$$

$$N = \frac{1}{\sigma(C+D)} \tag{4.9}$$

$$C = \frac{n}{|\alpha|} \cdot \frac{1}{n-1} \cdot \exp\left(-\frac{|\alpha|}{2}\right) \tag{4.10}$$

$$D = \sqrt{\frac{\pi}{2}}\left(1 + \operatorname{erf}\left(\frac{|\alpha|}{\sqrt{2}}\right)\right) \tag{4.11}$$

N is a normalisation factor and μ, σ, α and n are fitted parameter. CB is a PDF used in high-energy physics for description of decay processes, where some fraction of the energies and momenta are not detected. Reconstructed invariant mass spectrum of a resonance is then modelled with CB function. CB consists of standard Gaussian PDF and the power-law tail. The erf denotes the error function, which is defined as

$$\operatorname{erf} x = \frac{2}{\sqrt{\pi}} \int_0^x \exp\left(-t^2\right) \mathrm{d}t. \tag{4.12}$$

The width parameter of the CB function is free, but the width of the Gaussian is fixed as CB width plus a constant (this constant comes from the ratio of muon p_{T} resolutions in different parts of the detector. The rest of the CB parameters are obtained from MC simulation. The mean and the width of the $\psi(2S)$ are fixed to parameters of the J/ψ by multiplication by the ratio of measured masses of the $\psi(2S)$ and the J/ψ (values are taken from Particle Data Group [11]). The relative fraction of the CB and Gaussian components is a free parameter shared by both the $\psi(2S)$ and the J/ψ. The prompt charmonium signal line shapes in pseudo-proper lifetime are described by convolution of δ function and the gaussian resolution function $g(\tau_{\mu\mu})$, while the non-prompt contribution to signal

in pseudoproper lifetime is described by exponential function E convolved with the gaussian resolution function $g(\tau_{\mu\mu})$.

The prompt background contribution is described by a constant distribution in $m_{\mu\mu}$ and by a convolution of a δ function and gaussian resolution function in $\tau_{\mu\mu}$. Further, it has two non-prompt contributions: One of them is given by single-sided (only for positive values of pseudo-proper lifetime) exponential function convolved with gaussian resolution function $g(\tau_{\mu\mu})$, the second one is almost the same, but the single-sided exponential function is replaced by a double-sided exponential function in the pseudo-proper time. The two non-prompt backgrounds in the invariant mass $m_{\mu\mu}$ component are parametrised as two independent exponential functions of $m_{\mu\mu}$.

Table 4.4: Probability density functions for individual components in the fit model used to extract individual contributions for charmonium signals and backgrounds [2]. Functions summarised here are defined as: CB - Crystal Ball function, G - Gaussian function, E - Exponential function, F - constant distribution, δ - Delta function. The parameter ω_i is the fraction of the CB component in signal.

i	Type	Source	$f_i(m_{\mu\mu})$	$h_i(\tau_{\mu\mu})$
1	J/ψ	Prompt	$\omega_1 CB_1(m_{\mu\mu}) + (1-\omega_1)G_1(m_{\mu\mu})$	$\delta(\tau_{\mu\mu})$
2	J/ψ	Non-prompt	$\omega_1 CB_1(m_{\mu\mu}) + (1-\omega_1)G_1(m_{\mu\mu})$	$E_1(\tau_{\mu\mu})$
3	ψ(2S)	Prompt	$\omega_2 CB_2(m_{\mu\mu}) + (1-\omega_2)G_2(m_{\mu\mu})$	$\delta(\tau_{\mu\mu})$
4	ψ(2S)	Non-prompt	$\omega_2 CB_2(m_{\mu\mu}) + (1-\omega_2)G_2(m_{\mu\mu})$	$E_2(\tau_{\mu\mu})$
5	Background	Prompt	F	$\delta(\tau_{\mu\mu})$
6	Background	Non-prompt	$E_3(m_{\mu\mu})$	$E_4(\tau_{\mu\mu})$
7	Background	Non-prompt	$E_5(m_{\mu\mu})$	$E_6(\lvert\tau_{\mu\mu}\rvert)$

Previous results from publication [2] obtained using fit model described above are presented in Figure 4.23. Our results of fitting using the same fit model are presented in Figure 4.24 (for weighted data) and in Figure 4.25 (data without correction). It is necessary to emphasise that only acceptance correction was applied to data in this thesis. One can compare our results to results from [2]. The biggest difference between the results presented in the study [2] and the results of our study is in the size of used data sets.

The signal mass peak of the J/ψ is clearly visible, but the signal mass peak of the ψ(2S) is not visible due to limited statistics. Therefore, ψ(2S) yield was not successfully extracted.

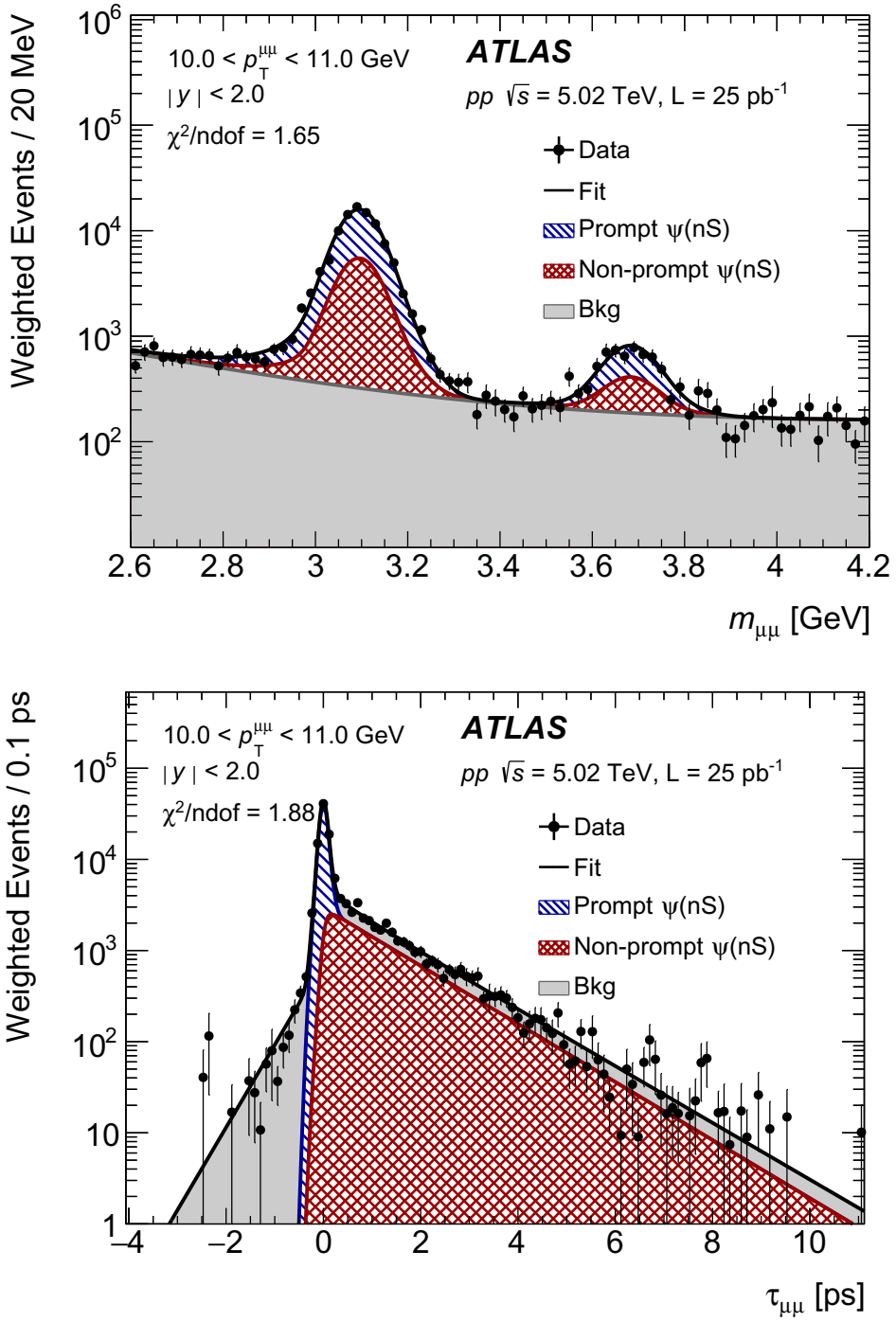

Figure 4.23: Projections of the charmonium fit onto dimuon invariant mass (top) and pseudo-proper time (bottom) for pp collisions at $\sqrt{s} = 5.02$ TeV for rapidity range $|y| < 2$. Figures are taken from [2].

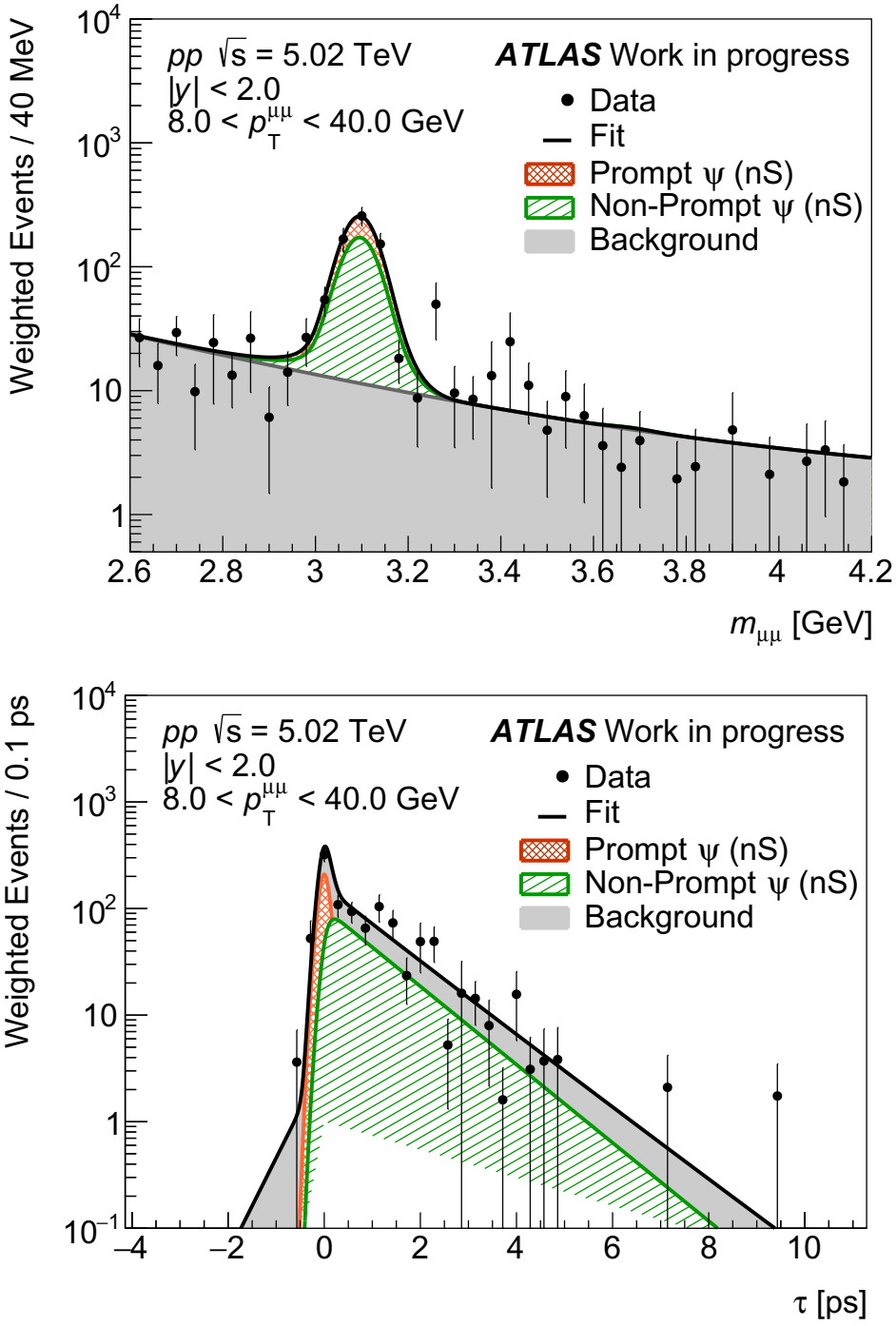

Figure 4.24: Projections of the charmonium fit onto dimuon invariant mass (top) and pseudo-proper time (bottom) for pp collisions at $\sqrt{s} = 5.02$ TeV for rapidity range $|y| < 2$. Data used in this fit were corrected for acceptance only.

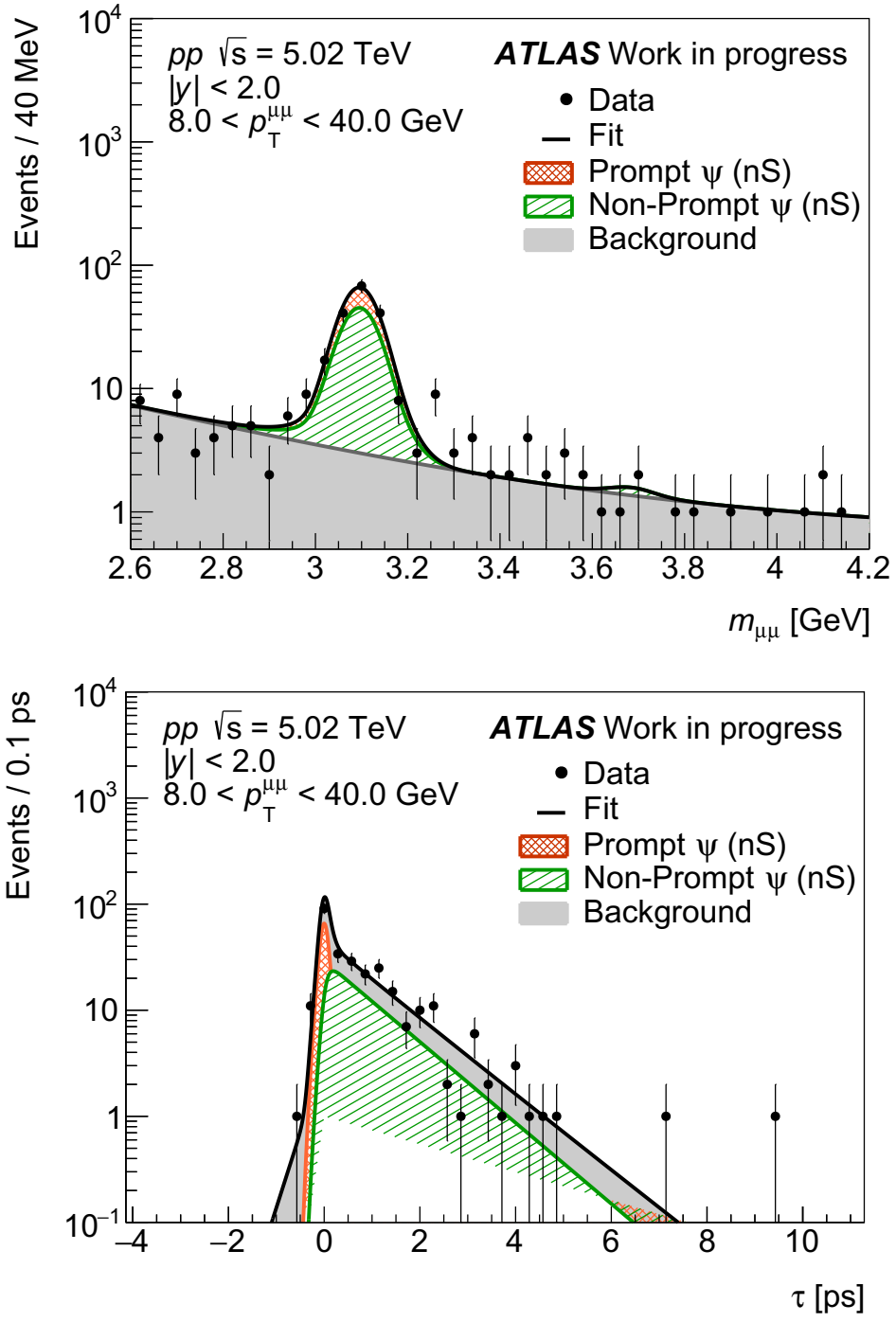

Figure 4.25: Projections of the charmonium fit onto dimuon invariant mass (top) and pseudo-proper time (bottom) for pp collisions at $\sqrt{s} = 5.02$ TeV for rapidity range $|y| < 2$. Data used in this fit were not weighted to correct for the acceptance.

4.5 J/ψ and ψ(2S) production cross-section

This section presents results calculated from the fit model described in section 4.4. These results are compared to MC simulations done in PYTHIA 8, and data published in 2017 in Refs. [2, 51].

In this thesis rapidity cut on $|y| < 2$ was used. Further, we used for estimation of prompt J/ψ cross section the same p_{T} binning as it was used in [2]. However, slightly different p_{T} binning for estimation of non-prompt J/ψ cross-section was used due to insufficient statistics. Our results are presented in figures 4.26 - 4.30 labelled as "ATLAS 2017 - Work in progress" (ATLAS 2017 - WIP), original results published in 2018 are labelled as ATLAS 2015. MC simulations are labelled as PYTHIA 8. Results of an estimated differential cross section of ψ(2S) are not shown since no yield is extracted from the dataset used in this study. Results from [2] are compared to the results obtained in MC Simulations. This comparsion is presented in Figure 4.29.

Results were normalised to the first bin of ATLAS 2015 data. Results obtained from PYTHIA 8 were normalised by the ratio of the cross-section of the selected process calculated by MC and the number of events. The value of this ratio is $1.79 \cdot 10^{-2}$ nb. Results were also multiplied by the branching ratio of charmonium decay to muon pair ($\psi(\mathrm{nS}) \to \mu^+\mu^-$) taken from Particle Data Group [11].

In Figures 4.26, and 4.27 one can see the discrepancy between our results and ATLAS 2015 results. Insufficient statistics most likely causes these differences.

There is also a discrepancy between ATLAS 2015 data and PYTHIA 8 simulation. It is known that PYTHIA 8 does not describe charmonia production properly. This discrepancy is displayed by ratio of ATLAS 2015 data, ATLAS 2017-WIP, and PYTHIA 8 simulation in Figure 4.28 for Prompt J/ψ differential cross section and it is displayed by ratio of ATLAS 2015 data and PYTHIA 8 simulation in Figure 4.30 for Prompt ψ(2S) differential cross section. The fluctuations of ATLAS 2017-WIP data caused by insufficient statistics are observed. Therefore, last bin of ratio ATLAS 2017-WIP/MC is neglected. Neither of these ratios is constant, and the discrepancy between ATLAS 2015 and PYTHIA 8 sample is about 10 times smaller in the case of ψ(2S) than in the case of J/ψ. It is seen that charmonia production is not described in PYTHIA 8 since it cannot reproduce the same shape of measured cross-section.

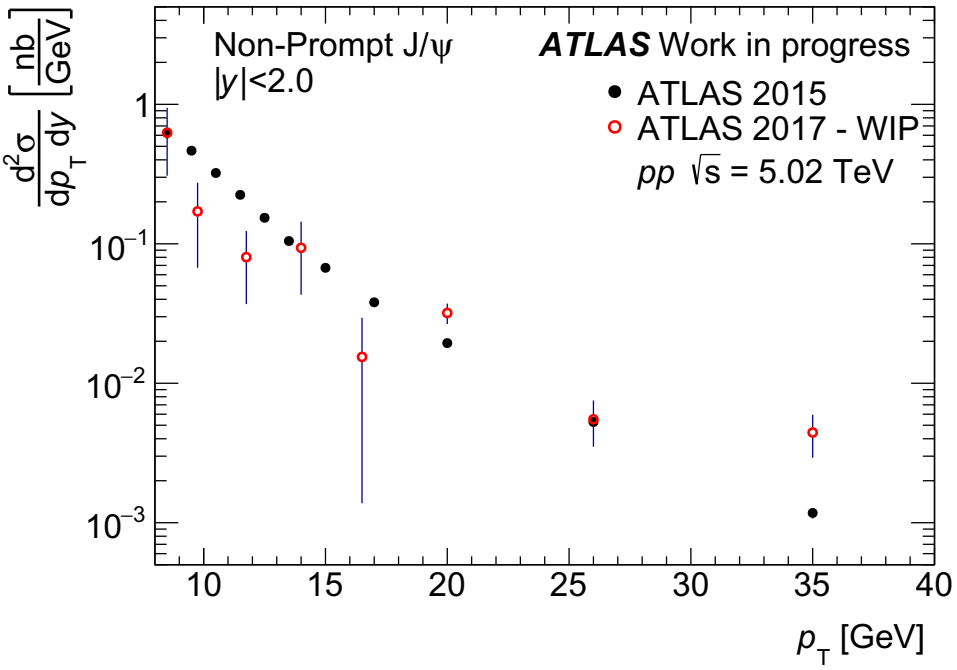

Figure 4.26: The differential Non-Prompt production cross section of J/ψ as a function of p_{T} for pp collisions at $\sqrt{s} = 5.02$ TeV for rapidity interval $|y| < 2$ compared to data from [2].

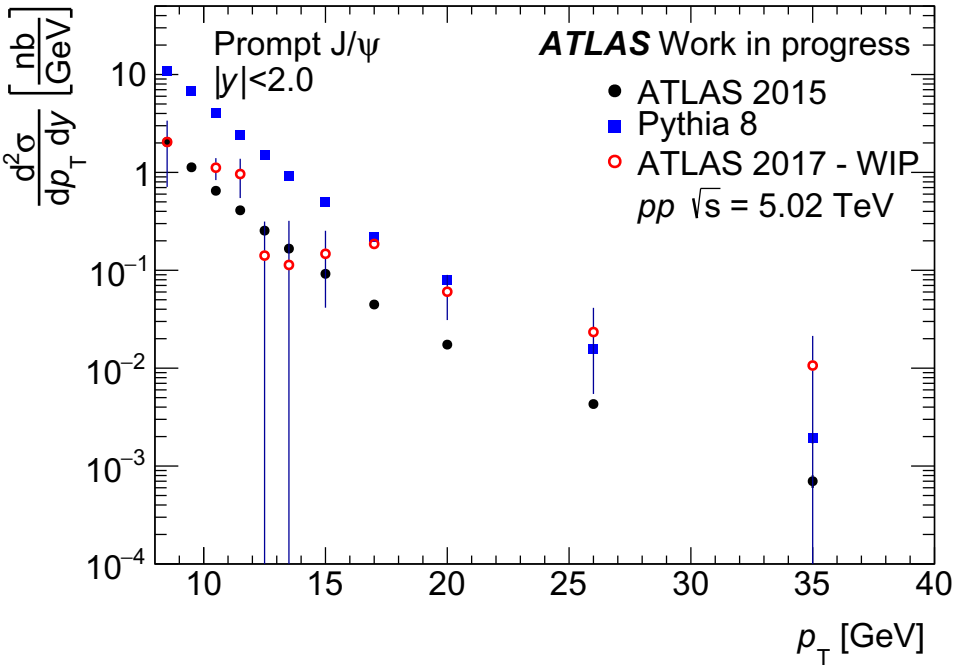

Figure 4.27: The differential Prompt production cross section of J/ψ as a function of p_{T} for pp collisions at $\sqrt{s} = 5.02$ TeV for rapidity interval $|y| < 2$ compared to data from [2] and MC simulation in Pythia 8.

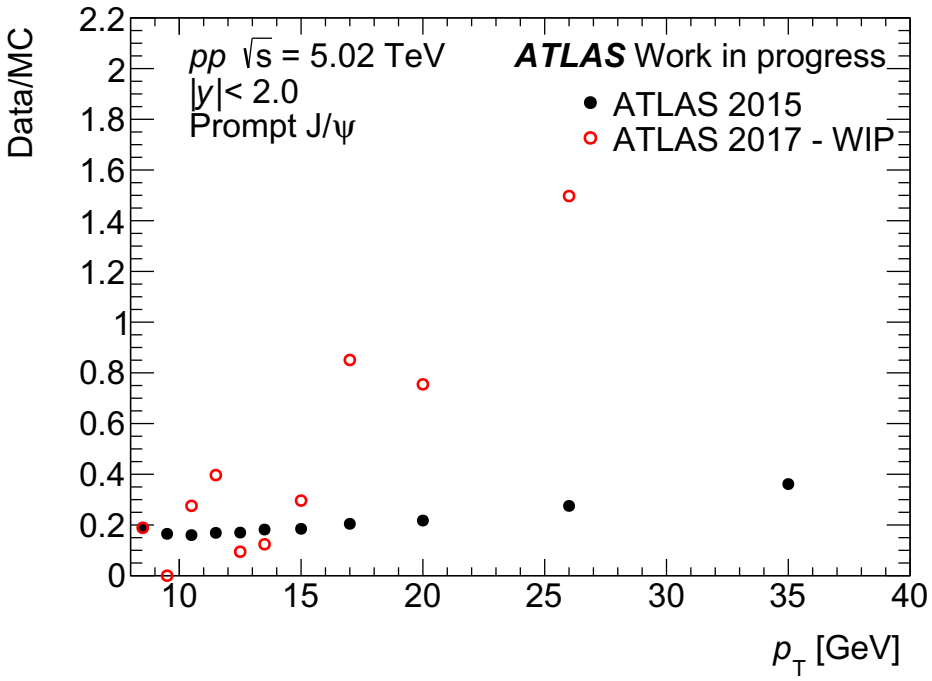

Figure 4.28: The ratio of measured and MC simulated (Pythia 8) differential Prompt production cross section of J/ψ as a function of p_{T} for pp collisions at $\sqrt{s} = 5.02$ TeV for rapidity interval $|y| < 2$.

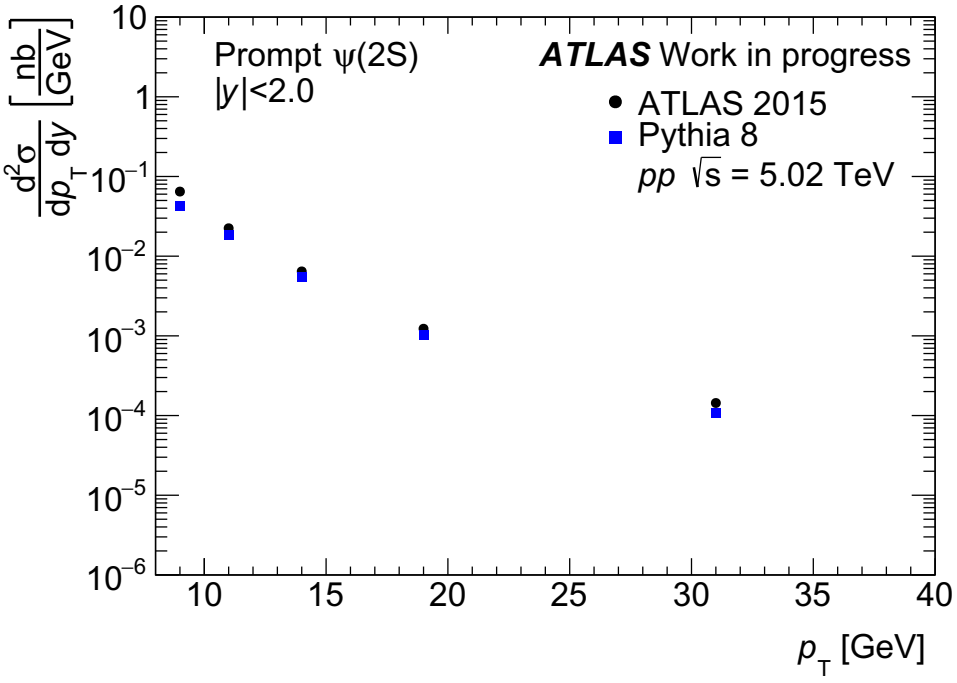

Figure 4.29: The differential Prompt production cross section of $\psi(2\mathrm{S})$ as a function of p_{T} for pp collisions at $\sqrt{s} = 5.02$ TeV for rapidity interval $|y| < 2$. Data from [2] are compared to the MC simulation from Pythia 8.

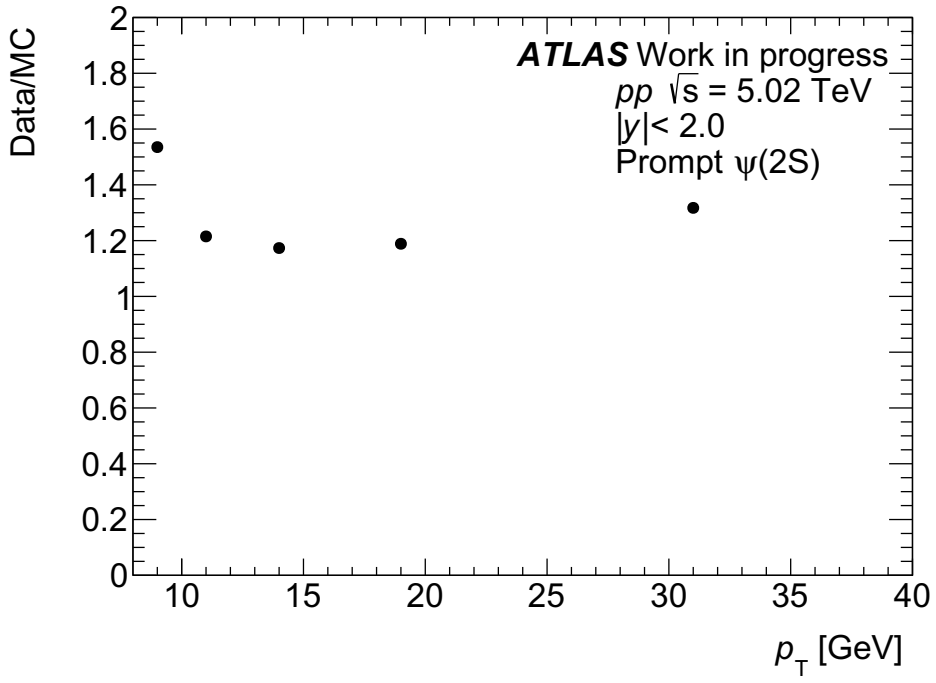

Figure 4.30: The ratio of measured and MC simulated (PYTHIA 8) differential Prompt production cross section of $\psi(2S)$ as a function of p_T for pp collisions at $\sqrt{s} = 5.02$ TeV for rapidity interval $|y| < 2$.

Summary and Conclusions

Chapter 1 briefly introduced the Standard Model of particle physics, including Quantum chromodynamics. Chapter 2 summarised the basics of heavy-ion collisions, including its description using the Glauber model. The end of this section provided the introduction to the quarkonia production. Chapter 3 described the experimental setup, including LHC and ATLAS Experiment.

Results of charmonium production and radiation produced in proton-proton collisions at center-of-mass energy $\sqrt{s} = 5.02$ TeV are presented in Chapter 4. To study production of ψ(nS), dimuon decay channel $\psi(\text{nS}) \to \mu^+\mu^-$ was used. First, Monte Carlo generator Pythia 8 was used to estimate inclusive charmonium production cross-section and study charmonia kinematics. Analysis of the charmonium gluon radiation using sample generated in Pythia 8 and quantification of the amount of charmonium gluon radiation was done. It was observed that the charmonium intermediate octet state on average radiates two gluons during its evolution to physical charmonium. The slow growth of the mean value of the number of gluons radiated by intermediate octet state with increasing p_{T} was observed. Understanding charmonium production and radiation in proton-proton collisions helps to understand charmonium production and suppression in heavy-ion collisions. Further, it may help to test different models describing charmonium production.

Further, basic information about the RooFit toolkit for data modelling and its usage for yield extraction is presented. RooFit was used to analyse data measured by ATLAS in 2017 (our main goal was to understand the fit model used in study [2] and to understand yield extraction provided using RooFit), and we compared these data with ATLAS data measured in 2015 and with our Pythia sample. In these results, there are discrepancies between data and Pythia 8 results. These discrepancies are transverse momentum dependent, and they are more significant for prompt J/ψ yields. This thesis did not reach the yield extraction of ψ(2S) due to insufficient statistics. It is seen that charmonia production is not fully described by Pythia 8 since it cannot reproduce the shape of measured cross-section.

This thesis did not provide the analysis of heavy-ion collisions data. However, it provided first steps towards evaluating basic observables such as the nuclear modification factor. The important part of future studies is to find the best way to quantify charmonium radiation. This thesis also presented first steps in that direction.

Bibliography

[1] T. Matsui and H. Satz. J/ψ Suppression by Quark-Gluon Plasma Formation. *Phys. Lett. B*, 178:416–422, 1986.

[2] Morad Aaboud et al. Measurement of quarkonium production in proton–lead and proton–proton collisions at 5.02 TeV with the ATLAS detector. *Eur. Phys. J. C*, 78(3):171, 2018.

[3] Steven Weinberg. *The Quantum Theory of Fields*, volume 2. Cambridge University Press, 1996.

[4] J. Horejsi. *Fundamentals of electroweak theory*. 2002.

[5] Wikipedia contributors. Standard model. `https://en.wikipedia.org/wiki/Standard_Model`. Online; Accessed: 05 Mar 2022.

[6] ATLAS Collaboration. Observation of a new particle in the search for the Standard Model Higgs boson with the ATLAS detector at the LHC. *Physics Letters B*, 716(1):1–29, Sep 2012.

[7] A. Das and T. Ferbel. *Introduction to Nuclear and Particle Physics*. World Scientific Publishing, 2 edition, 2005.

[8] B. R. Martin. *Nuclear and Particle Physics*. John Wiley & Sons, Ltd, 2006.

[9] Jiri Chyla. Quarks, partons and Quantum Chromodynamics. 2 2004.

[10] Walter Greiner, Stefan Schramm, Eckart Stein, and D.A. Bromley. *Quantum Chromodynamics*. Springer, 3rd rev. and enl. ed edition, 2007.

[11] P.A. Zyla et al. Review of Particle Physics. *PTEP*, 2020(8):083C01, 2020.

[12] Experiment ATLAS. An ATLAS high mass dijet event. `https://cds.cern.ch/record/1697057`, Apr 2014. General Photo.

[13] Ryan Atkin. Review of jet reconstruction algorithms. *Journal of Physics: Conference Series*, 645:012008, oct 2015.

[14] *Expected performance of the ATLAS experiment: detector, trigger and physics*. CERN, Geneva, 2009.

[15] James D Bjorken. Energy loss of energetic partons in quark-gluon plasma: possible extinction of high p_T jets in hadron-hadron collisions. Technical report, FERMILAB, Batavia, IL, Aug 1982.

[16] Miklos Gyulassy and Larry McLerran. New forms of QCD matter discovered at RHIC. *Nucl. Phys. A*, 750:30–63, 2005.

[17] ATLAS Collaboration. HI event display - November 2015. `https://cds.cern.ch/record/2105590`, Nov 2015. General Photo.

[18] Roy J. Glauber. Quantum optics and heavy ion physics. *Nuclear Physics A*, 774:3–13, Aug 2006.

[19] Michael L. Miller, Klaus Reygers, Stephen J. Sanders, and Peter Steinberg. Glauber Modeling in High-Energy Nuclear Collisions. *Annual Review of Nuclear and Particle Science*, 57(1):205–243, Nov 2007.

[20] Sebastian Tapia Araya, Qipeng Hu, Petr Gallus, Nikita Smirnov, William Brooks, and Jorge Andres Lopez. Supporting note for measurement of J/$\psi \rightarrow$ $\mu^+\mu^-$ and ψ(2S)$\rightarrow$ $\mu^+\mu^-$ with 2015 Pb+Pb data at $\sqrt{s_{\mathrm{NN}}}$ = 5.02 TeV. Technical report, CERN, Geneva, Jul 2016.

[21] Urs Achim Wiedemann. Jet Quenching in Heavy Ion Collisions. pages 521–562, 2010.

[22] G. Aad et al. Observation of a centrality-dependent dijet asymmetry in lead-lead collisions at $\sqrt{s_{\mathrm{NN}}} = 2.76$ TeV with the atlas detector at the lhc. *Phys. Rev. Lett.*, 105:252303, Dec 2010.

[23] Morad Aaboud et al. Measurement of the nuclear modification factor for inclusive jets in Pb+Pb collisions at $\sqrt{s_{\mathrm{NN}}}$ = 5.02 TeV with the ATLAS detector. *Phys. Lett. B*, 790:108–128, 2019.

[24] J. Soto. Overview of Non-Relativistic QCD. *The European Physical Journal A*, 31(4):705–710, Mar 2007.

[25] Jean-Philippe Lansberg. New observables in inclusive production of quarkonia. *Physics Reports*, 889:1–106, Dec 2020.

[26] S. Digal, P. Petreczky, and H. Satz. Quarkonium feed-down and sequential suppression. *Physical Review D*, 64(9), Oct 2001.

[27] Peter Cho and Adam K. Leibovich. Color-octet quarkonia production. *Phys. Rev. D*, 53:150–162, Jan 1996.

[28] J. P. Lansberg, A. Rakotozafindrabe, P. Artoisenet, D. Blaschke, J. Cugnon, D. d'Enterria, A. C. Kraan, F. Maltoni, D. Prorok, H. Satz, Joseph Cugnon, Lansberg Jean-Philippe, and Nicolas Matagne. Perspectives on heavy-quarkonium production at the lhc. *AIP Conference Proceedings*, 2008.

[29] Morad Aaboud et al. Prompt and non-prompt J/ψ and ψ(2S) suppression at high transverse momentum in 5.02 TeV Pb+Pb collisions with the ATLAS experiment. *Eur. Phys. J. C*, 78(9):762, 2018.

[30] Georges Aad et al. Z boson production in Pb+Pb collisions at $\sqrt{s_{\mathrm{NN}}}$= 5.02 TeV measured by the ATLAS experiment. *Phys. Lett. B*, 802:135262, 2020.

[31] Georges Aad et al. Measurement of $W^{\pm}$ boson production in Pb+Pb collisions at $\sqrt{s_{\mathrm{NN}}}$ = 5.02 TeV with the ATLAS detector. *Eur. Phys. J. C*, 79(11):935, 2019.

[32] CERN. CERN Homepage. `https://home.cern/`. Online; Accessed: 24 Oct 2021.

[33] Lyndon R Evans and Philip Bryant. LHC Machine. *JINST*, 3:S08001. 164 p, 2008. This report is an abridged version of the LHC Design Report (CERN-2004-003).

[34] ATLAS Experiment. The ATLAS Experiment. `https://atlas.cern/`. Online; Accessed: 24 Oct 2021.

[35] ATLAS Collaboration. The ATLAS Experiment at the CERN Large Hadron Collider. *JINST*, 3:S08003, 2008.

[36] CERN Bulletin. The particle suppliers. Les fournisseurs de particules. (BUL-NA-2010-077. 14/2010):03, Mar 2010.

[37] Joao Pequenao. ATLAS detector. `https://cds.cern.ch/images/CERN-GE-0803012-01`. Online; Accessed: 26 Oct 2021.

[38] Joao Pequenao. Inner Detector figure. `https://cds.cern.ch/images/CERN-GE-0803014-01`. Online; Accessed: 31 Oct 2021.

[39] Joao Pequenao. Computer generated image of the ATLAS Muons subsystem. `https://cds.cern.ch/record/1095929`, Mar 2008. Online; Accessed: 01 Nov 2021.

[40] Smita Darmora. *Search for a Supersymmetric Partner to the Top Quark using a Multivariate Analysis Technique*. PhD thesis, Texas U., Arlington, 8 2015.

[41] Torbjörn Sjöstrand, Stefan Ask, Jesper R. Christiansen, Richard Corke, Nishita Desai, Philip Ilten, Stephen Mrenna, Stefan Prestel, Christine O. Rasmussen, and Peter Z. Skands. An introduction to PYTHIA 8.2. *Computer Physics Communications*, 191:159–177, Jun 2015.

[42] Torbjörn Sjöstrand, Stephen Mrenna, and Peter Skands. PYTHIA 6.4 physics and manual. *Journal of High Energy Physics*, 2006(05):026–026, May 2006.

[43] Raghunath Sahoo. Relativistic Kinematics. `https://inspirehep.net/literature/1444984`, Apr 2016.

[44] Jing Chen, Q Hu, Y Zhu, M Donadelli, Zvi Hirsh Citron, Kunlin Han, Sebastian Tapia Araya, and Petr Gallus. Supporting note for charmonium and bottomonium analyses using 2013 p+Pb data at 5.02 TeV and 2015 p+p data at at 5.02 TeV. Technical report, CERN, Geneva, Aug 2014.

[45] G. Aad, B. Abbott, J. Abdallah, O. Abdinov, B. Abeloos, R. Aben, M. Abolins, O. S. AbouZeid, N. L. Abraham, and et al. Muon reconstruction performance of the ATLAS detector in proton–proton collision data at $\sqrt{s}$ =13 TeV. *The European Physical Journal C*, 76(5), May 2016.

[46] The ATLAS Collaboration. Measurement of the differential cross-sections of inclusive, prompt and non-prompt production in proton-proton collisions at $\sqrt{s} = 7$ TeV, 2011. `https://www.sciencedirect.com/science/article/pii/S0550321311002938`.

[47] Wouter Verkerke and David P. Kirkby. The RooFit toolkit for data modeling. *eConf*, C0303241:MOLT007, 2003. https://root.cern/manual/roofit/.

[48] R. Brun and F. Rademakers. ROOT: An object oriented data analysis framework. *Nucl. Instrum. Meth. A*, 389:81–86, 1997. https://root.cern/.

[49] M. Baak, G. J. Besjes, D. Côté, A. Koutsman, J. Lorenz, and D. Short. Histfitter software framework for statistical data analysis. *The European Physical Journal C*, 75(4), Apr 2015.

[50] M. Oreglia. A Study of the Reactions $\psi' \to \gamma\gamma\psi$. Other thesis, 12 1980.

[51] ATLAS Collaboration. Measurement of quarkonium production in proton–lead and proton–proton collisions at 5.02 TeV with the ATLAS detector. HEPData (collection), 2020. https://doi.org/10.17182/hepdata.82624.